Using impact parameter information for leptonic τ decays in the measurement of the W$\rightarrow \mu\nu$ decay

Nassim Ainouz

Masterarbeit in Physik
angefertigt im Physikalischen Institut

vorgelegt der
Mathematisch-Naturwissenschaftlichen Fakultät
der
Rheinischen Friedrich-Wilhelms-Universität
Bonn

January 2021

I hereby declare that this thesis was formulated by myself and that no sources or tools other than those cited were used.

Bonn, 05.01.2021 .....
Date

.....
Signature

1. Gutachter: PD Dr. Philip Bechtle
2. Gutachterin: Prof. Dr. Klaus Desch

Contents

CHAPTER 1

Introduction

The particle accelerator LHC at CERN has been in operation for over 10 years and was succesful in measuring the Higgs boson in 2011 which was postulated decades ago. The Higgs boson was a missing puzzle piece in the Standard Model. Furthermore, the LHC was constructed in order to search for particles that could not be described by the Standard Model like supersymmetric particle or other unresolved problems. There a various ways to probe for new physics. Either one raises the energy with which the particles are colliding in a particle accelerator in hope to find a new massive particle or one tries to measure very precisely important parameters that put constraints on beyond the Standard Model physics. One of its aspects is that of the lepton universality which says that the decay to the different lepton generations should be equal because apart from the mass there is no difference between an electron, a muon and tau. Thus, the branching ratio of a decay to these different final states should be equal and so far no violation of the lepton universality has been observed. A way to test this would be to look at the branching ratio fraction. A measurement by LEP in the year 2006 gave a $2.8\,\sigma$ uncertainty for $\mathcal{BR}(W \to \tau\nu)/\mathcal{BR}(W \to \mu\nu)$. A recent analyis of 2020 showed that the lepton universality is in accordance with the Standard Model but the search for new physics via presice meaurement remains promising.
On of the ways to test the Standard Model is to improve the measurement of the mass of the W boson. Currently, a reanalysis of the W-boson mass with Run 1 data is performed. This thesis is a part of that reanalyis and will test if the impact parameter can be used in improving the measurement. The impact parameter is distributed differently depending on whether the decay is $W \to \tau\nu$ or $W \to \mu\nu$. Furthermore, the decays $Z \to \tau\tau$ and $Z \to \mu\mu$ can be used to calibrate the impact parameter distribution.
The theoretical understanding which is needed will be explained in chapter 2. In chapter 3 the ATLAS detector and the particle and vertex reconstruction are presented. A short summary of the analysis of the boson mass and how what the main idea of this thesis can be found in chapter 4. The calibration of the impact parameter and how its uncertainties are determined are layed out in chapter 5. After that, the result of the p_T fit are presented in chapter 6. At the end, the last chapter 7 summarizes the thesis and its results and gives a quick outlook.

CHAPTER 2

Theoretical Background

2.1 The Standard Model of Particle Physics

The Standard Model of particle physics (SM) is a theoretical and mathematical framework to describe the interaction of elementary particles on a fundamental level. It quantifies all elementary particles by their mass, charge, spin and color. These particles are the building blocks of all matter in the universe. Furthermore, processes that these particles can be involved in are described by this theory which was developed over the course of the last century. The SM consists of three forces which explain all physical processes. Any elementary particles can be categorized as a member of one of two groups, either boson or fermion. Bosons are particles with an integer spin while fermions do have a half odd interger spin. Other classifications are done based on the way the particles interact. There are three ways in which a particle can interact. [2]
Each interaction is governed by its respective gauge particles. These particles are bosons and thus have an integer spin. They are exchange particles and can interact with any particle that is carrying the respective charge. These bosons differ in charge, mass and interaction range. What follows is a brief description of

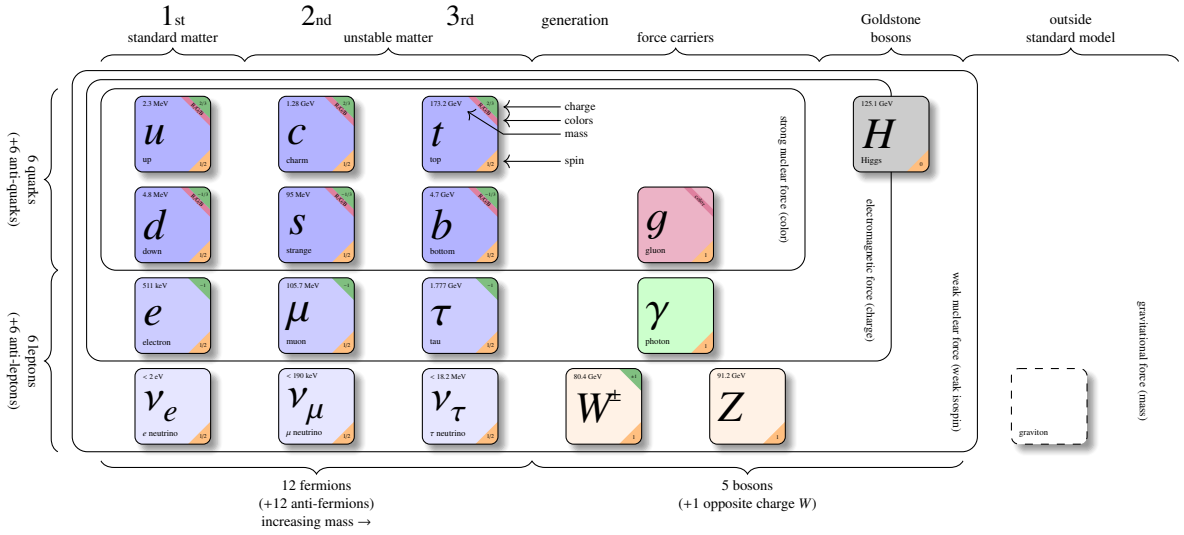

Figure 2.1: Visual representation of all fundamental particles that make up the SM including bosons and fermions. Each particle is listed with its electrical charge, mass, color and spin[1]

the three forces and its gauge particle.

The electro-magentic force is a unified force of electricity and magnetism which were thought to be seperated. Its gauge boson is the photon which has no mass and no electrical charge. The photon can couple to any particle with an electrical charge, either quark, lepton or boson. Because the photon is massless, it is stable and does not decay, hence the electromagnetic force has an infinite range.

The weak force has three gauge particles, the neutral Z boson and two charged W bosons. These bosons have a heavy mass and thus have short lifetime and a limited interaction range. All fermions carry weak charge but neutrinos are the particles that can only interact via the weak force.

The strong force is mediated by the gluon which is massless and stable but has limited interaction range because the gluon carries colour charge which is the quantum number of the strong force. Out of the fermions only the quarks can interact via the strong force. Thus, it is responsible for binding quarks and forming hadrons.

In addition to the exchange bosons, there is another boson which is different in a various ways. The Higgs, with a mass of 125 GeV, is a scalar-like boson with zero spin and is a excitation of the Higgs field which spontaneously breaks the electroweak symmetry(see Sec. 2.1.1). It was proposed in the 1960's, and discovered by the ATLAS and CMS collaboration in 2012.[3]

Besides bosons, there are fermions which carry a spin of 1/2 and are the elementary particles that make up matter and consist of two groups, the quarks and the leptons. Further, there are neutrally charged leptons that are considered massless in the SM, called the neutrinos, that only interact via the weak force and leptons with an electrical charge that interact via the weak and electromagnetic force. Each fermion belongs to one of three generations with each generation having increased mass. For the quarks there are two types, the up-type quarks with +2/3 electrical charge and the down-type quarks with -1/3 electrical charge. Thus, there are six different quarks with the last one, the top quark, being discovered in 1995 at Fermilab. Quarks form a bound state composed out of two or three quarks which are called mesons or baryons, respectively. Recently, they have been even observations of pentaquarks and heptaquarks. The most known elementary particles are the electron and the up and down quark which form the proton and the neutron. [4]

The names of the fundamental forces indicate that they have not equal strength. In fact, they are many orders of magnitude apart when comparing their coupling constants. The smallest is the weak coupling constant which is six orders lower than the coupling constant of the strong force, the electromagnetic force is two orders of magnitude below the strong force.

Since the electro-magnetic and the weak force has been unified as the electro-weak force, efforts have been made to unify all aspects of SM. For high energies electro-weak and the strong force can be described as one. For decades theoretical physicists have tried to include the gravitional force and describe it as a quantum field theory but so far without any success. Furthermore, on these small scales the gravitational force does not play a significant role.

2.1.1 Electroweak interaction

Most of the focus will put on the electroweak interaction because this is the crucial part of a W-boson analysis.

The electroweak interaction is a $SU(2) \times U(1)_Y$ symmetry group, whereas $SU(2)$ is the weak isospin and $U(1)_Y$ is the hypercharge symmetry. Initially, four massless vector bosons are required, consisting of a W triplet (W_1, W_2, W_3) originating from $SU(2)$ and B^0 singlet originating from $U(1)_Y$, responsible for the weak isospin and weak hypercharge, respectively. Forcing massterms into the Lagrangian is not helpful because it would violate gauge invariance. Introducing in the Lagrangian a term for the Higgs field:

$$\mathcal{L}_h = |\mathcal{D}_\mu h|^2 - \lambda\left(|h|^2 - \frac{v^2}{2}\right)^2 \tag{2.1}$$

$$V(\phi) = \mu^2|\phi|^2 + \lambda(|\phi|^2)^2 \tag{2.2}$$

with λ having is postive value because the potential needs to be bound from below. For μ^2, there are two possibilities, either it is positive than the potential looks the left side of Fig.2.2 and this would recreate massless bosons. But if μ^2 is negative the potential looks like on the right side of Fig.2.2.

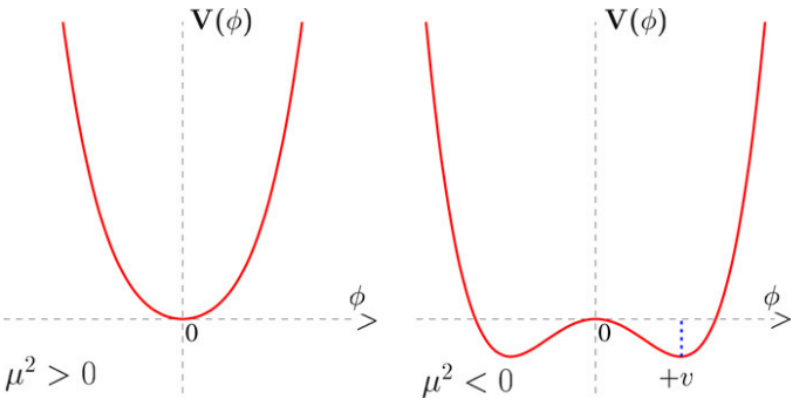

Figure 2.2: Potential of the scalar field ϕ for two different μ^2. [5]

Now the field has a non-zero vacuum expectation value $v = \left(-\frac{\mu^2}{\lambda}\right)^{1/2}$ which leads to the breaking of the symmetry.[6] The gauge symmetry is spontaneously broken by the Higgs Mechanism which leads to $SU(2) \times U(1)_Y \rightarrow U(1)_{EM}$ and boson mixing resulting in massive gauge particles for the weak force.[7]

The new interacting term of the Lagrangian looks like:

$$\frac{1}{2}(\partial H)^2 + \frac{1}{8}g_2^2(v+H)^2|W_\mu^1 + iW_\mu^2|^2 + \frac{1}{8}(v+H)^2|g_2W_\mu^3 - g_1B_\mu|^2 \tag{2.3}$$

which leads to a new definition of the fields[5]:

$$W^\pm = \frac{1}{\sqrt{2}}(W_1 + iW_2), \quad Z_\mu = \frac{g_2W_\mu^3 - g_1B_\mu}{\sqrt{g_1^2+g_2^2}}, \quad A_\mu\frac{g_2W_\mu^3 + g_1B_\mu}{\sqrt{g_1^2+g_2^2}} \tag{2.4}$$

with g_1, g_2 being the coupling constant of the $SU(2)$ and $U(1)_Y$ group.

To be exact, B^0 and W^3 mix in this way.[6]

$$\begin{pmatrix}\gamma\\ Z^0\end{pmatrix} = \begin{pmatrix}\cos(\Theta_W) & \sin(\Theta_W)\\ -\sin(\Theta_W) & \cos(\Theta_W)\end{pmatrix}\cdot\begin{pmatrix}B^0\\ W^3\end{pmatrix} \tag{2.5}$$

forming the known Z^0 boson and the photon γ. The mixing is governed by the weak mixing angle Θ_W. The masses of the bosons are defined as:

$$m_W = \frac{1}{2}vg_2, \quad m_Z = \frac{1}{2}v\sqrt{g_1^2 + g_2^2}, \quad m_A = 0 \tag{2.6}$$

2.1.2 Leptons

As already mentioned there are two types of leptons, namely charged and chargeless leptons. The electron with a mass of 510.99 keV is the most known and the only charged lepton which is stable. The muon, discovered in 1936, is approximately 200 times heavier (105.66 MeV) and has a mean lifetime of 2.2 µs. The tau, with a mass 3500 times higher than the electron, has an even shorter lifetime which is approximately $(290.3 \pm 0.5) \times 10^{-15}$ sec , which made its discovery challenging. It was in 1975 when the tau lepton was found by Martin Pearl at SLAC[8] after being predicted by Yung-su Tsai in 1971. The tau has a mass of (1 776.86 ± 0.12) MeV and is thus heavier than a proton or neutron. All of these leptons have an electrical charge of -1e. Each of these three leptons has a corresponding massless and chargeless neutrino with a corresponding name (electron neutrino...). Thus, there are six leptons, just like there are six quarks. The lack of charges for the neutrinos makes it a challenge detecting them but has been able in specifically designed experiments.

Tau decay

Because the tau plays an important role in this analysis what follows is a small discussion of its decay. As the tauon is the heaviest lepton, it has a short lifetime and thus will decay in the beam line which makes it difficult to detect. Because of this dealing with the tau is a tough situation but also a promising one because its mass does play a role in possible charged Higgs that is more likely to couple to particles with a higher mass.

As the tau decays shortly after its creation one has to know the different decay modes of the lepton and track the decay products in order to decide if a detected particle is due to a tau lepton. It can decay in two ways, either hadronically or leptonically, as can be seen in the feynman graph of Fig.2.3. The most dominant decay modes are listed in Tab.2.1 in which one can see that hadronic decays are the most probable. This is whats sets the tau apart from the muon and electron because it is the only lepton that can decay hadronically.

A hadronic decay involves the creation of at least one or more pions which are more helpful in identifying the tau than the leptonic modes because the leptons could have been produced without a tau. Another difficulty like all leptonic decays is that a neutrino is produced which will pass the detector undetected. A way to distinguish hadronic decay products from gluon jets and quark background is to look at how the showers are grouped. The ones for the tau decay are not part of a big shower and more collimated.[9]
Taus are considered to be favorable candidates in the search for physics beyond the Standard model because theories predict that a tau would be more affected due to its mass.

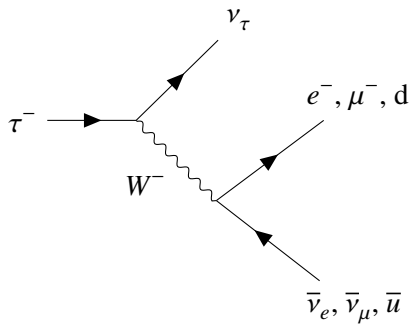

Figure 2.3: Feynman diagram of tau decay for the lowest order

decay mode	branching fraction
$e^-\bar{\nu}_e\nu_\tau$	17.82 ± 0.04
$\mu^-\bar{\nu}_\mu\nu_\tau$	17.39 ± 0.04
$\pi^-\nu_\tau$	10.82 ± 0.05
$\pi^-\pi^0\nu_\tau$	25.49 ± 0.09
$\pi^-2\pi^0\nu_\tau$	9.26 ± 0.10
$\pi^-\pi^+\pi^-\nu_\tau$	9.31 ± 0.05

Table 2.1: Most dominant decay modes of the tau lepton [10]

2.1.3 W- and Z-boson

Because of the electroweak theory predicting new types of bosons the search for the W and Z boson increased with the construction of particle accelerators. The construction of a proton-antiproton accelerator was proposed at CERN. The first $p\bar{p}$-collision was realized with $\sqrt{s} = 540\,\mathrm{GeV}$ in 1981. The following year $W \to e\nu$ could be observed and in 1983 the decays $Z \to e^+e^-$ and $Z \to \mu^+\mu^-$ were observed.[11]. The current masses are[10]

$$m_W = (80.379 \pm 0.012)\,\mathrm{GeV} \quad m_Z = (91.1876 \pm 0.0021)\,\mathrm{GeV} \tag{2.7}$$

The respective decay widths are[10]

$$\Gamma_W = (2.085 \pm 0.042)\,\mathrm{GeV} \quad \Gamma_Z = (2.4952 \pm 0.0023)\,\mathrm{GeV} \tag{2.8}$$

In Fig.2.4 the most likely decays of the W boson can be seen. The most likely decays for the Z boson can be found in Tab.2.3

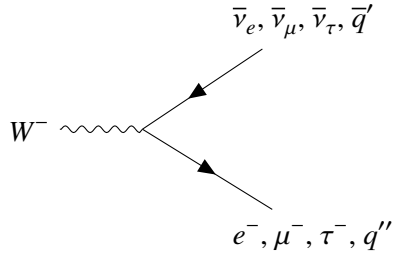

Figure 2.4: Lowest order Feynman diagram for the W-boson decay

Mode	Branching fraction (Γ_i / Γ)
$\ell^+\nu$	(10.86 ± 0.09)%
$e^+\nu$	(10.71 ± 0.16)%
$\mu^+\nu$	(10.63 ± 0.15)%
$\tau^+\nu$	(11.38 ± 0.21)%
hadrons	(67.41 ± 0.27)%

Table 2.2: Most dominant decay modes of the W boson and its fraction[10]

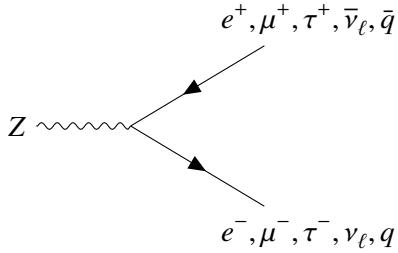

Figure 2.5: Lowest order Feynman diagram of the Z-boson decay

decay mode	fraction ± uncertainty
e^+e^-	3.3632 ± 0.0042
$\mu^+\mu^-$	3.3662 ± 0.0066
$\tau^+\tau^-$	3.3696 ± 0.0083
$\nu_\ell\bar{\nu}_\ell$	20.000 ± 0.055
hadrons	69.911 ± 0.056

Table 2.3: Most dominant decay modes of the Z boson and its fraction

2.1.4 Decay Processes

What follows is a list of processes and decays which will be discussed in this thesis. After the collision of two accelarated protons a myriad of decays are detected. Out of these only a few will be taken into account, namely the ones that are originate from a W or Z decay. W and Z cannot be detected directly because of their great mass. Instead their decay products can be measured.

Leptonic Decays

The W boson has several decay channels. One of them is the leptonic one in which the W boson can decay to an electron, muon or tau, with its corresponding anti-neutrino. The neutrino evidently will go through the detector unnoticed. Each of the leptonic decay modes make up roughly 11 percent as can be seen in Tab.2.2. Because the tau's lifetime is short, it is possible that a detected muon or electron stems from a tau lepton.

The Z boson has three leptonic decays mode. Because the Z is neutrally charged each decay channel conists of $l\bar{l}$ which leave tracks in opposite directions due to momentum conservation in the rest frame. Each of these decay modes has a likelihood of roughly three percent.[10] But because the Z boson has no electric charge, it has another possibility of decaying leptonically which makes up one fifth of all Z decays. This decay mode is considered invisible because it consists of two neutrinos which go through the calorimeters undetected.

Hadronic Decays

For both bosons, the W and Z, the hadronic decay channel is the most dominat one.
Because there are no free quarks due to confinement every W boson which decays into two quarks will form either a bound state of one or several quark. The hadronic decay channel which makes up roughly two thirds of all decays consists most of the time of multiple of pions with corresponding neutrinos. These pions will be detected as particle showers in the hadronic calorimeter. Because hadronic showers do not soley originate from boson decays it cannot be used to identify them.Just like for the W decay, around two thirds of all Z decays are hadronic as seen in Tab.2.3.

2.1.5 Lepton Universality

Branching Ratio

The branching ratio of a certain decay shows how likely it is for the mother particle to decay to a particular final state. If a particle X can decay to either Y_1 or Y_2 the branching ratio for $X \to Y_1$ is defined as:

$$BR(x \to Y_1) = \frac{\Gamma(X \to Y_1)}{\Gamma(X)} = \frac{\Gamma(X \to Y_1)}{\Gamma(X \to Y_1) + \Gamma(X \to Y_2)}, \tag{2.9}$$

with $\Gamma(X \to Y_1)$ being the partial decay width and $\Gamma(X)$ the total decay width. Every decay mode depends on the particular matrix element $\Gamma(X \to Y_1) \propto |\mathcal{M}(X \to Y_1)|^2$.
The advantage of comparing the branching ratios is the cancellation of systematic uncertainties. A possibility for which the ratio could divert from one would be the introduction of supersymmetry or a charged Higgs that would play a role in favoring one decay over the other.

The partial decay width for the W boson does only depend on constants expcept for small kinematic mass corrections due to phase space.[12]

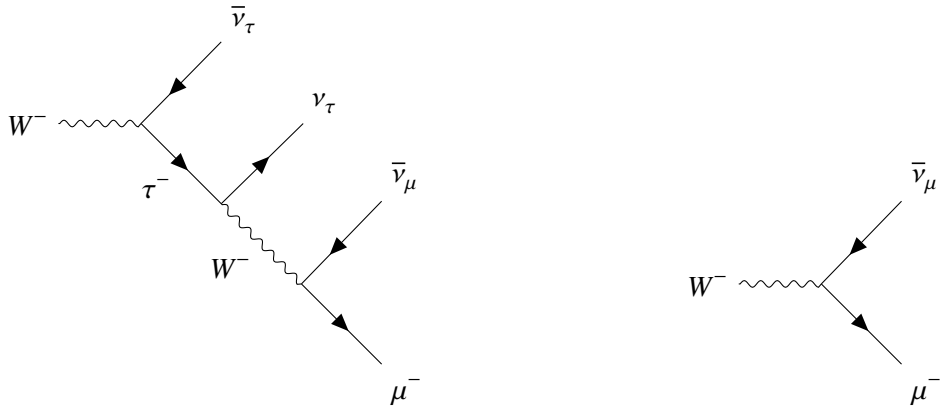

(a) W decay to muon via tau

(b) W decay to muon

Figure 2.6: Feynman diagrams for two different W-decay channels

$$\Gamma(W^- \to \ell^- \bar{\nu}_\ell) = \frac{G_F M_W^3}{6\pi\sqrt{2}}, \tag{2.10}$$

with $G_F = \frac{\sqrt{2}g^2}{8M_W^2}$[13] being the Fermi constant which depends on the weak coupling constant g.

Thus neglecting the mass of the leptons, there is no difference between the electron, muon and tau regarding the quantum numbers.[14] Thus, a gauge particle like the W boson, should connect in equal amounts to the leptons resulting in equal branching ratios for the W decay. It can be tested in neutral and charged weak interactions by looking at leptonically decaying W and Z bosons. A way to probe lepton universality, would be to measure the branching ratios of the individual lepton channels and then compare these ratios as seen in Eq.2.9.
So far, lepton universality was verified by several experisments and no violation has been observed. For the W boson the decay mode to the electron and the muon are close to each other and within the uncertainty with $(10.71 \pm 0.16)\%$ and $(10.63 \pm 0.15)\%$, respectively. The fraction for the tau lepton is a bit off with $(11.38 \pm 0.21)\%$. The decay mode to tau was measured at LEP and yields a $2.8\,\sigma$ difference with respect to the other leptonic decay modes.[15]

This leads to a possible explanation of a charged Higgs boson that couples to massive particles and thus influences the decay to the tau more than other leptons. But the difference is still not enough to say that lepton universality is broken. Furthermore, the tau's short lifetime makes reconstruction not easy and explains its uncertainty.

At LHCb semileptonic B meson decays were analysed and the ratio of branching fraction $\mathcal{R}(D^*) = BR(\bar{B}^0 \to D^{*+}\tau^-\bar{\nu}_\tau)/BR(\bar{B}^0 \to D^{*+}\mu^-\bar{\nu}_\mu)$ showed a two sigma discrepancy for the lepton universality.[16] It was the first measurement of tau final states of b hadron decays at a hadronic collider.

A recent paper using the $\sqrt{s} = 13\,\text{TeV}$ ATLAS run analysing W-boson decays that stem from $t\bar{t}$ events, has made the most precise measurement of the ratio $R(\tau/\mu) = BR(W \to \tau\nu_\tau)/BR(W \to \mu\nu_\mu) = 0.992 \pm 0.013$ which is in good agreement with the Standard Model and did not show any deviation. [17]

2.2 Shortcomings of the SM

So far, the Standard Model has been succesful in explaining a majority of physical processes. But other phenomena have yet to be explained. The most prominent example is dark matter which is elaborated on in Sec.2.2.1. Other instances are in which the SM predicts a process but the experimental results differ in way that it may not be a statistical fluctuation. What follows are a few unanswered question of the SM.

One major flaw of the SM is the absence of the gravitational force and why its coupling constant is much smaller compared to the other fundamental forces.

Another problem is the huge range in masses for the elemantary particles from the up quark to the top quark which are around four orders of magnitude apart. Recent discovers like the neutrino oscillation show that the neutrinos do have a mass, in contrast to the SM which says neutrinos are massless. Another prominent example is the unbalance of matter and anti-matter in the universe. The big bang should create matter and anti-matter in equal manner but all detected matter is so far no anti-matter.

2.2.1 Dark Matter

One of the most glaring issues is the fact the SM only describes visible matter despite dark matter being much more dominant in the universe than the visible one. The name dark matter was chosen because so far its effect can only be detected via its gravitational pull and not via radiation. Thus, it consists of an undiscovered particle. Possible candidates are so-called WIMPS, weakly interacting massive particles.

A prime reason why something like dark matter is needed can be seen in Fig.2.7. This plot shows the rotation curve of a galaxy depending on its radius. The y-axis displays the rotational velocity around the center of the galaxy. Usually, the velocity should decrease but stays flat as function of the radius. The plots shows different contribution that necessary to fit the data. The disc and gas aspects do not explain why the velocity does not drop off but uncounted mass outside of the galaxy disc can.

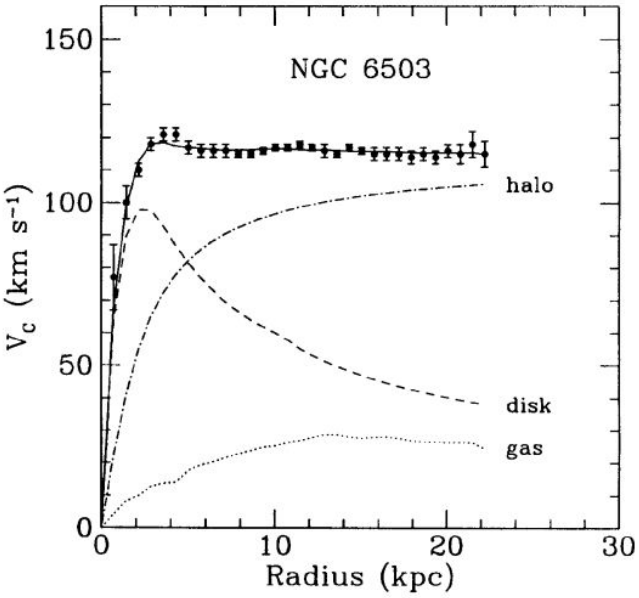

Figure 2.7: Rotation velocity plotted against the radius for the galaxy NGC 6503. The dashed lines describe the different contribution of the fit. The solid line includes all constribution and fits the data.[18]

2.2.2 The Case for New Physics

As mentioned, the SM is a theoretical framework that can predict and efficiently describe a majority of physical interactions. Other processes cannot be described by SM, hence the search for physics beyond the Standard Model or New Physics. There various theoretical ideas to expand the SM. From supersymmetry, which gives each particle a partner that differs by a half-integer spin, to string theory. Other ways to probe the SM is to look at theoretical predictions which differ from the experimental results. Precision measurements of the SM could give an insight into where new physics could arise. This is why precise testing of the lepton universality, which differs two standard deviations from the theoretical predictions, could improve the understanding the shortcoming of the SM. Precise measurements can put constraints on other observations.

The mass measurement of the W boson is very much a precision measurement that tries to reduces the uncertainties on the mass further and further. Other possibilities than supersymmetry that could have an effect on high energy physics, as the measurement of W mass is, are an additional vector boson which coupling constant differs depending on the quark and lepton. Another theory states that leptoquarks are coupling to leptons and quarks. These extensions of the SM would violate the lepton universality.

For quite some time physicists are looking for New Physics because of the shortcomings of the SM. One way is, as already mentioned, precision measurements, and another way is, in the field of particle physics, high-energy experiments in order to find theoretical particles that should be able to be produced at a high-energy scale.

2.3 Production of W/Z bosons at LHC

This section briefly describes how the weak gauge bosons are produced at the Large Hadron Collider(more on that in Sec.3.1). Production is only possible if the centre-of-mass energy is high enough so that heavy particles like the Z and the W bosons can be created. A proton is composed out of three quarks but they carry fifty percent of the energy and the rest is part of the gluons. That means the centre-of-mass energy would have to be at least six times higher than the mass of the boson.

2.3.1 W boson

In Fig.2.8 one can see the Feynman diagrams for W^+ production. On the left side, the u quark stems from the proton accelerated by the LHC. It interacts with a gluon that is part of the other accelerated proton. On the right side two gluons interact with each other result in the production of a W boson via the weak force. At the same time, one or in the case of Fig.2.8(b) two quarks are created that will hadornize. Similiar Feynman diagrams can be drawn to produce a W^- boson

(a) Production of W boson with a gluon and a quark

(b) Production of W boson with two gluons

Figure 2.8: Feynman diagram for single-W production

2.3.2 Z boson

Because the Z decay will be used as a tool to put constraints on the impact parameter of the lepton originating from the boson decay one should have a quick look at the Z-boson production.

During the collision one quark of the proton from each bunch forms a Z boson. These quarks have to carry opposite charge as seen in Fig.2.9 on the left side in the leading-order diagram. On the right side the next to leading order is shown. Here, a quark interacts with a gluon from the other proton which leads to a quark that gives off a Z boson.

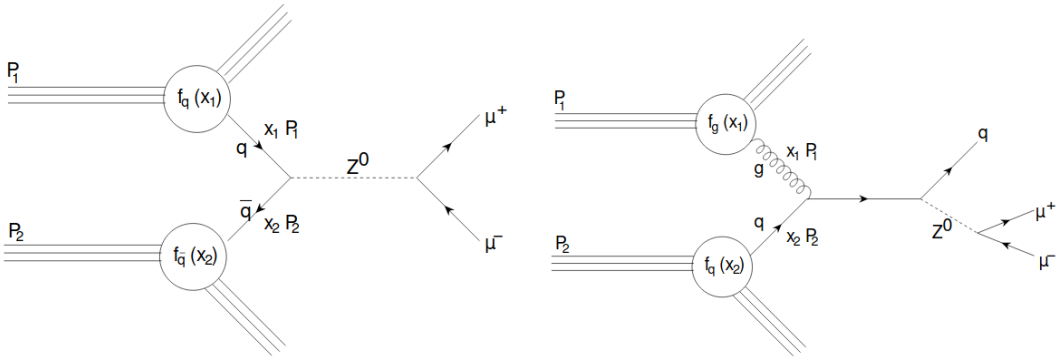

Figure 2.9: Leading order and next to leading order diagram for Z boson production at LHC[19]

CHAPTER 3

Experimental Setup

The following chapter presents the particle accelerator and detector which played the role in producing and recording the data used for this analysis.

3.1 Large Hadron Collider

The Large Hadron Collider(LHC), the world's largest particle accelerator with a circumference of 27 km, is located near Geneva, Switzerland, 100 m beneath the surface, and was built from 1998 to 2008 by the European Organization for Nuclear Research (CERN). It is located in a 3.8 m wide tunnel which was used for LHC's predecessor LEP, which was a lepton accelerator with 209 GeV center-of-mass energy. LHC has four main detectors: ATLAS, CMS, LHCb and ALICE, all located at different points of the accelerator. ATLAS and CMS are general-purpose detectors, used in the search for the Higgs particle and new physics. ALICE is exhibiting the quark-gluon plasma that existed shortly after the big bang. The LHCb experiment is used to investigate the difference betweeen matter and anti-matter. Furthermore, there a four smaller experiments perfomred at LHC. Next to the main collider ring are a linear accelerator and proton boosters to bring the particles up to speed. The collider beam is no continous beam held in place by the dipole magnets but grouped in bunches. They reason why protons are used is because they can accelerated easier due to the smaller energy loss because of synchrotron radiation.

Luminosity

The luminosity is defined as:

$$L = \frac{1}{\sigma}\frac{dN}{dt} \quad L_{int} = \int L dt \tag{3.1}$$

The luminosity and the integrated luminosity are a way to describe how good the performance of a particle accelerator is. σ stands for the cross section and $\frac{dN}{dt}$ for the particle flow rate. By raising the flow rate, increasing the cross section and taking data for a longer period of time. This would lead to a higher amount of data the higher the chance of finding something of interest.

3.2 ATLAS detector

The ATLAS detector is part of the Large Hadron Collider which received over the years several upgrades which took the beam energy from 3.5 TeV to currently 13 TeV. It is 45 meters in length and 25 m

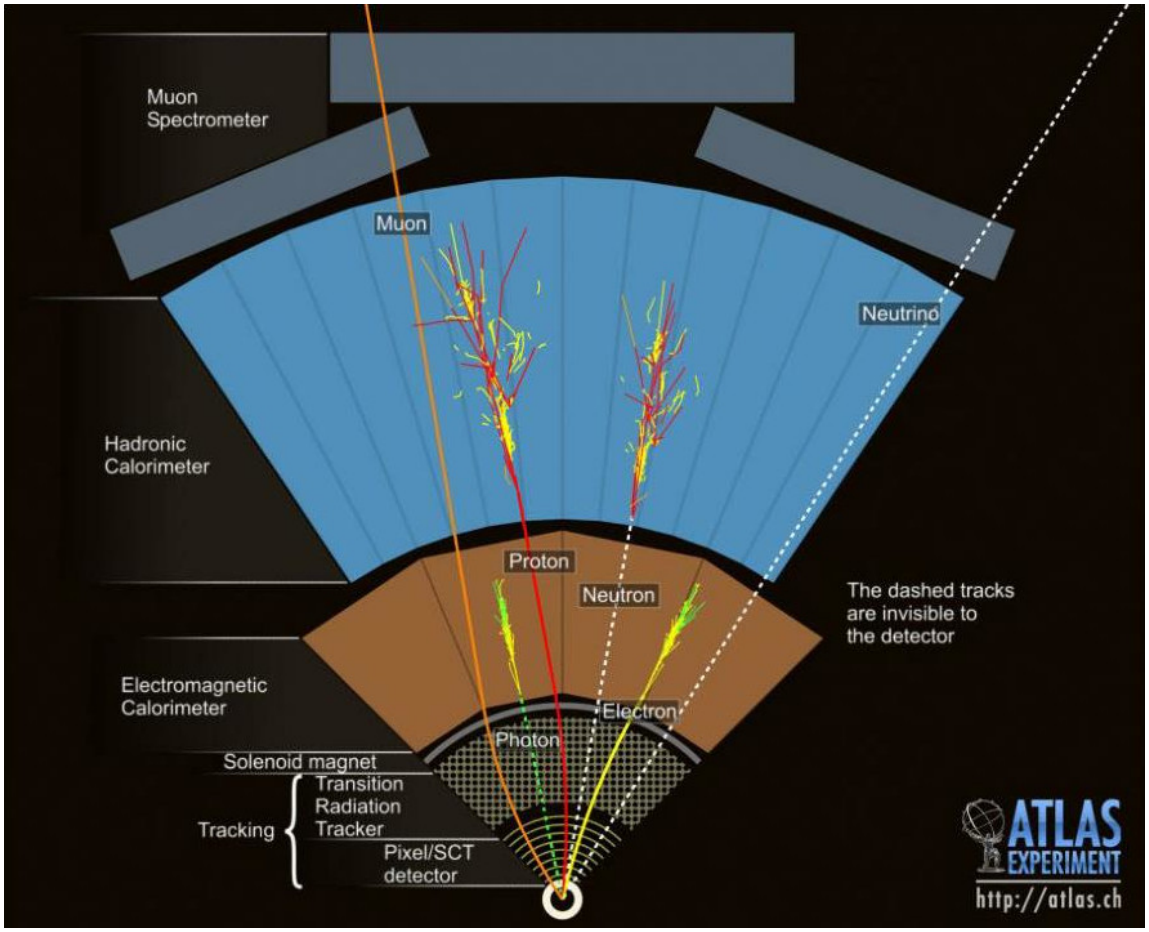

Figure 3.1: Cross section display of the different components of the ATLAS detector and a representation of particle tracks and their showers in the respective calorimeter. The compoment at the very bottom is the inner detector, the electromagnetic calorimeter is shown in brown while the hadronic calorimeter is shown in blue. At the very top the muon spectrometer is visible[21]

in diameter and weighs 7000 tonnes. Unlike other detector such as ALICE or LHCb, ATLAS is a multi-purpose detector with a 4π range such as the search for new physics, CP violation and the discovery of the Higgs particle. Around the interaction point one needs various layers in order to track and measure different variables of the daughter particles which were created by the collision. For this work the data of RUN 1 with $\sqrt{s} = 7\,\text{TeV}$ and $\sigma = 4.57\,\text{fb}^{-1}$ was used[20].
The four main components of the ATLAS detector are listed below and explained in detail in Sec.3.2.2:

- Inner Detector
- Electromagnetic Calorimeter
- Hadronic Calorimeter
- Muon Spectrometer

As seen in Fig.3.1, particles differ in their trajectory depending on their type and their charge.
Before the different components of the detector are examined its coordinate system will be presented.

3.2.1 ATLAS Coordinate System

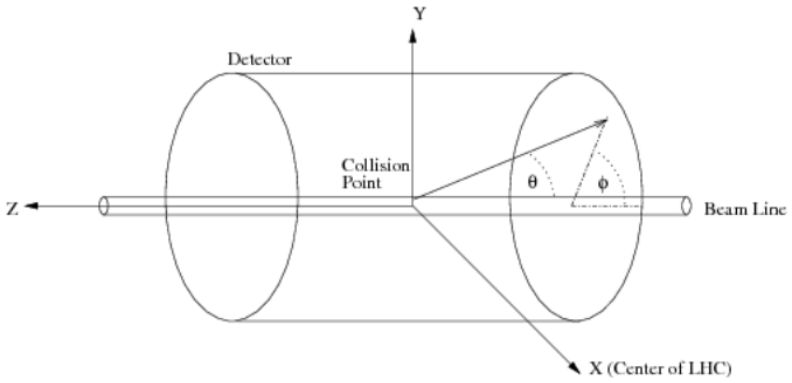

Figure 3.2: Coordinate system of the ATLAS detector. The z-axis aligns with the beam line while the y-axis points upwards and the x-axis points towards the center of the LHC. ϕ is the azimuthal angle around the z-axis. θ describes the angle between the positive z-axis and the particle trajectory. [22]

The beam axis serves as the z axis of the coordinate system, the x axis points towards the center of the accelerator ring, while the y axis points upward and the interaction point severs as the origin as visualized in Fig.3.2. The polar angle θ stands for the angle between the z-axis and the particle track and ϕ is the azimuthal angle around the beam pipe[23].

Pseudorapidity

The pseudorapidity η is defined as

$$\eta = -\ln\left(\tan\left(\frac{\theta}{2}\right)\right), \tag{3.2}$$

wheares θ is the angle between the beam axis and the particle's trajectory. The closer the particle track gets to the beam axis the higher η gets. The pseudorapidity is a way to characterize in which region of the detector the particle decayed. The reason why η is rather looked at than rather the polar angle θ is because the differences in rapidity are lorentz invariant.[24] A visualization for different values of η is shown in Fig.3.3, in which one can see how the pseudorapidity changes for different polar angles. The smaller the angle the greater the value of η gets.
An observable that can be expressed with η is called the p-quant. Its definition and dependencies are shown below:

$$p_{quant} = \frac{1}{\sqrt{p^2 \sin^3(\theta)}}, \quad \sin(\theta) = \frac{1}{\cosh(\eta)}, \quad p = p_T \cdot \cosh(\eta) \tag{3.3}$$

3.2.2 Subsystems

In this section the different parts that make up the ATLAS detector are presented as seen in Fig.3.1. They will be exlpained from the most inner layer to the outside.

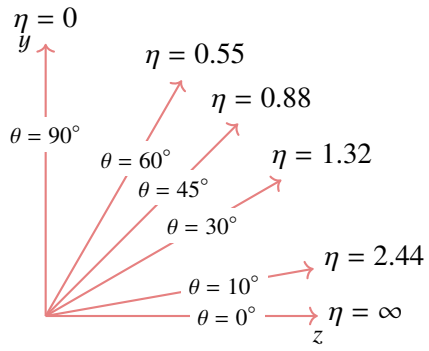

Figure 3.3: Representation of pseudorapidity for different values of the polar angle θ. The smaller θ the higher η.Y-axis points upwards and the z-axis is aligned with the beam line.[25]

3.2.3 Inner detector

The following paragraphs describe the different components of the most inner part of the detector. Its main purpose is to track and provide vertex information for the particles passing through it by measuring their momenta and charge.

All of the inner detector is encapsulated by a superconducting solnenoid magnet creating a 2-T magnetic field which is parallel to the beam axis all particles with an electrical charge are exhitbiting a curved trajectory due to the Lorentz force as seen in Fig.3.1[26].

Pixel detector

The pixel detector is composed of its basic unit, a rectangular module that measures 6 cm by 2 cm. In total there are 1744 modules assembled in three concentric circles around the beam line. Each of these three layers has a distance to the interaction point of 50.5 mm, 88.5 mm and 122.5 mm, respectively. The very first layer is called the B-layer. Furthermore, three discs of for both end-caps each help in giving a three-hit system for coverage of $|\eta| < 2.5$. Each module consists of a controller chip, 250 µm thick n^+ -on-n silicon sensors and 16 front-end chips. There are 47232 pixels each with a size of 50 µm × 400 µm typically[27].

The front-end chips can determine if charge was deposited by the time-over-threshold method. The module controller chip gathers the data from the 16 readout chips and converts and sends it to electronics outside of the detector[28].

In total, the most inner layer of ATLAS consist of 80 million pixels surrounding the beam pipe.

Semi Conductor Tracker

The next layer in the inner detector is the semi conductor tracker. Its radius covers the distance from 299 mm to 560 mm. For the semi conductor tracker(SCT) there are in total 4088 modules of silicon-strip detectors, 2212 of these are part of four concentric barrels, the remaing are installed in the two endcaps. Every sensor consists of p-on-n strips. Four rectangular silicon-strip sensors make up each module. The nominal resolution for SCT is 580 µm in the z direction and 17 µm in the R-Φ plane[29].

The SCT is able to provide four space-points to better determine the vertex and momenta of the particles. Other requirements of SCT is reconstruct leptons with $p_T > 5$ GeV and meaure the momentum of high-energy leptons at $p_T = 500$ GeV with at least 30% precision with a coverage of $|\eta| < 2.5$[30].

Transition Radiation Tracker

The transition radiation tracker(TRT) is the last layer of the inner detector. Its basic unit is a proportional straw drift tube that is 4 mm in diameter. Each straw is filled with a gas mixture of 70% Xe, 27% CO_2 and 3% O_2[31]. They form a barrel that surrounds the previous layers, and two endcaps. In total there are 52544 straws each with a length of 144 cm arranged in 73 layers make up the barrel and 122880 straws pointing towards the beam line. The radius from 0.5 m to 1.1 m is covered by the TRT.

The TRT is effective in making a distinction between electrons and charged pions. Particle identification is possible due to the difference in transition radiation depending on the particle.

For charged particles with $p_T > 0.5\,\text{GeV}$ and $|\eta| < 2.0$ the TRT is able to achieve a resolution of 120 µm[32].

Electromagnetic Calorimeter

The electromagnetic calorimeter's role is to measure electrons, positrons, photons and neutrally charged pions. Leptons will loose energy by the means of bremsstrahlung, photons by pair production, with both producing a shower in the calorimeter as seen in Fig. 3.1. For high energetic electrons Bremsstrahlung will be the dominating process in which the particles will lose energy[33]. Additionally, the calorimeter is used for tracking purposes.

There are three main components: the electromagnetic barrel, the electromagnetic end-caps and the forward liquid argon calorimeter(FCal) as shown in Fig.3.4.

The first two components are constructed by layering lead and liquid argon in an accordion structure. Pseudorapidity range of up to $|\eta| < 3.2$ is covered by the barrel and the end-caps. The FCal has a electromagnetic part which is responsible for detecting high boosted particles with $|\eta| < 4.9$.

The energy resolution for the electromagnetic calorimeter can be parametrized by:

$$\frac{\sigma(E)}{E} = \frac{a}{\sqrt{E}} \oplus \frac{b}{E} \oplus c \tag{3.4}$$

$$= \frac{10\%}{\sqrt{E}} \oplus \frac{200\,\text{MeV}}{E} \oplus 0.7\%, \tag{3.5}$$

with a being a stochastic term, b a noise term and c a constant term for the barrel[34].

Hadronic Calorimeter

Looking at the Feynmann diagram for the W decay, one of its decay channels includes quarks which cannot be detected as such because of confinement. Quarks forms various bound states as hadrons that need to be detected in order to decide which decay to place.

This calorimeter measures the energy from hadronic particles like charged pions, protons and neutrons that interact with it and thus creating a hadronic shower.

There are two parts that make up the hadronic calorimeter: the tile calorimeter, the hadronic end-caps as shown in Fig.3.4. The tile caloriemter consists of layers of steel and scintillators and cover the region $|\eta| < 1.7$. The end-caps are responsible for a boosted range of $1.5 < |\eta| < 3.2$ and are made out of alternating layers of copper and liquid argon. Additionally, a FCal is located next to the end-caps and close to the beam pipe with a pseudorapidity range of $3.1 < |\eta| < 4.9$. The hadronic FCal has layers of tungsten and liquid argon[35].

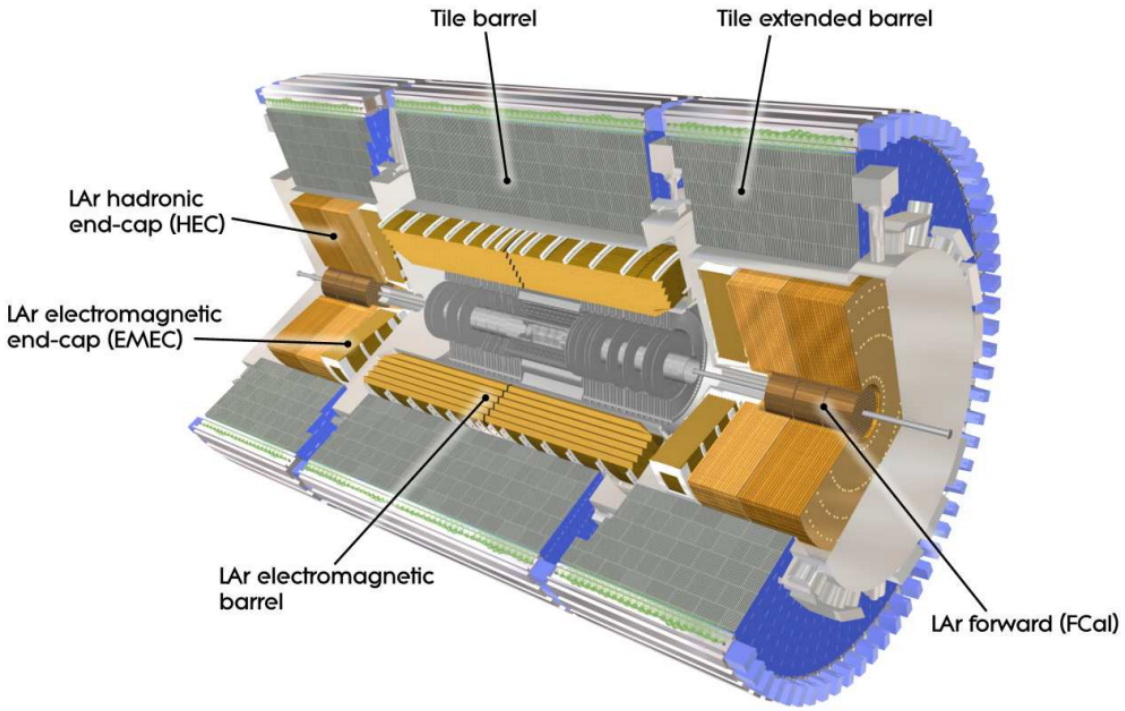

Figure 3.4: Depiction of the calorimeter system of the ATLAS detector. The inner detector in the middle is surounded by the golden coulored electromagnetic calorimeter. Its barrel is parallel to the inner detector while the end-caps are found and the the end[36]

An incoming particle hits the copper/tungsten layer which serves as absorber. Secondary particles ionize the argon. This current can be used as indicator of how many daughter particles were created in the calorimeter and thus the mass of the original particle. In the case of the tile calorimeter, a iron plates serve as the absorber and the scintillator material produces scintillation light which is transmitted to the photomultiplier by fibers on both sides of the module[36].

Because the hadronic calorimeter is where hadronisation is taking place, this calorimeter's resolution is limited due to complex structure of the particle showers. For this reason the shower's width and length is wider and longer which translates to a larger calorimeter.

Muon Spectrometer

Because muons interact weakly and have a higher mass than electron they rarely interact with the calorimeters. Thus, the most outer part of the detector is a muon spectrometer which measures the trajectory and energy of the muons passing through (see Fig.3.1). The muon spectrometer consists of three components: the monitored drift tubes, the cathode strip chambers and the resistive plate chamber[37]. This is done by the way of muon drift tube chambers which are filled a gas mixture of argon and carbon dioxide. Several layers of muon drift chambers are stacked on top of each other to avoid muons passing through without detection. Because of this the muon spectrometer makes up a large part of the ATLAS detector. The spectrometer has a momentum resolution for muons between 10 and 100 GeV of 2-3% and of 10% for very energetic muons at 1 TeV

3.2.4 Trigger System

Since protons are colliding at such a high rate it is not possible to store all data generated by the proton-proton interactions and one needs triggers to filter out a huge amount of data[38].
For RUN 1 a hardware built trigger, called Level-1 trigger (L1), reduces the amount of collisions from 1 GHz to 75 kHz. L1 defines a promising region, the region of interest (RoI), which is used by the second trigger. Because L1 acts on every bunch it can only use a limited amount of detector information and has only 2.5 μ sec to make a decision. This Level-2 trigger (L2) reduces the data rate to 3.5 kHz with a decision time of 40 m sec. The final trigger is an event filter(EF) by using offline analysis tools. After this last trigger the rate is cut down to 200 Hz which is the limit of data taking capabilities. L2 and EF are called High Level Trigger (HLT) and are software based that operate on computing farms outside the detector[35].

3.2.5 ATLAS Data taking

The LHC is not able to deliver the maximum amount of luminosity in an instant. As every accelerator LHC needs time to start up to reach a stable beam. Additionally, the number of events can vary from day to day and from experiment to experiment. It has to be noted that the data taking period was part of Run 1 at $\sqrt{s} = 7$ TeV, created by proton-proton collisions, as seen in Fig.3.5(a) where the total integrated luminosity over time is plotted. The green area displays the luminosity delivered by LHC, the yellow area shows the one recorded by ATLAS and the blue one shows the luminosity which is of good quality. These areas differ because firstly the detector is not perfect and cannot record everything and secondly what is considered 'good' quality depends on the well maintained detector component and well reconstructed physics object to be considered suitable for further analysis. On average nine interactions per crossings were recorded as given by poisson distribution on the number of interactions per crossing for each bunch as seen in Fig.3.5(b). In the end 4.57 fb^{-1} were used.

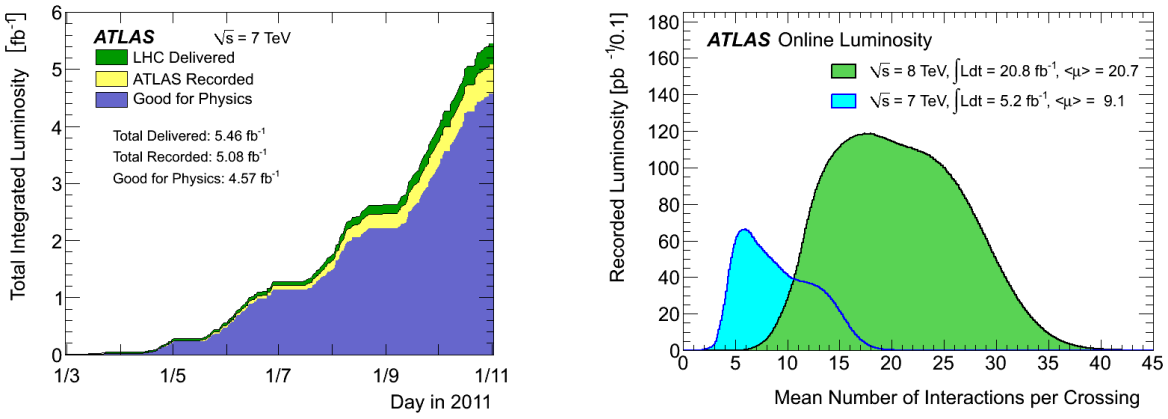

(a) (b)

Figure 3.5: (a): Culumatated luminosity in 2011 at $\sqrt{s} = 7$ TeV. Green stands for luminosity delivered by LHC, yellow for luminosity recorded by ATLAS and blue for luminosity that can be used for physics analysis. (b): Mean Number of Interactions per Crossing for $\sqrt{s} = 7$ TeV in blue and $\sqrt{s} = 8$ TeV in green[39]

3.3 Particle Reconstruction

This section describes the way different physical objects are recreated after the data has been registered in the detector. For this analysis the reconstuction of the muon and tau lepton, the jets and the missing transverse energy will be focused on.

3.3.1 Multijet reconstruction

Jets are objects that conists of strongly interacting particles that form a collimated cone. Most of the proton-proton colossions end up being gluons and quarks that will hadronize due to color confinement when detected as energy deposits in the calorimeters. Jets events are reconstucted by a three-step method which is detailed below.

Topological clustering

In this step the four-vector is defined. Calorimeter cells that have a large ratio of singal to noise($|E_{cell}| > 4\,\sigma_{\text{noise}}$) with σ being the sum of the expected electronic and pile-up noise are used as seeds for the algorithm. Adjacent cell to the seed cell are grouped together if they fullfil $|E_{miss}| > 2\,\sigma_{\text{noise}}$. After that, all remaining adjacent cells are added regardless of their energy. This grouping is called topocluster. The formed cluster is treated as massless with an energy that equals the energy of all cell that are part of the cluster[40].

Jet algorithms

Here, an anti-k_t algorithm[41] is applied to decide what object are grouped together to form a jet.

A distance parameter is defined as:

$$d_{ij} = \min\left(k_{t,i}^{2p}, k_{t,j}^{2p}\right)\frac{\Delta ij^2}{R^2}, \tag{3.6}$$

$$d_{iB} = k_{t,i}^{2p}, \tag{3.7}$$

where $\Delta_{ij}^2 = (y_i - y_j)^2 + (\phi_i^2 - \phi_j^2)^2$. $k_{t,i}$ is the transverse momentum of a partice i. y_i is its rapidity and Φ its azimuthal angle. R is a parameter of the radius of the cone and takes values of either 0.4 or 0.6. The relative power of the energy compared to the geometrical scale is governed by the parameter p. The value of p is chosen as $p = -1$ to prevent soft radiation.

The clustering algorithms tries to find the shortest distances between two objects d_{ij} or between an object and beam particle d_{iB}. If the smallest distance is d_{ij} the objects i and j are combined and it is d_{iB} the object i is a jet and removed from the list. Afterwords the distance is computed again and the process is repeated until no object is left.

Jet energy calibration

The last step of reconstruction is to account for effects that have an influence on the energy measurement and need to be corrected like calorimeter leakage and dead detector cells.

The measurements were done at the electromagnetic scale because the energy deposits were tuned with electromagnetic showers. The idea is to correct the jet energy measurement for the hadronic scale. There are detector effects that will be corrected because they influence the jet energy measurement. A few of these detector effects are listed below:

- Dead detector cells
- Partial energy measurement
- Energy leakage

The calibration scheme called (EM +JES) is divided into three steps. The first one is to remove the average additional energy that is caused by pile-up. The direction of jets points towards the centre of the ATLAS detector but in the second step the position of the jet is corrected in such a way that the direction points towards the primary vertex. In the third step the jet position and energy are corrected using data-driven corretions by looking at the difference between truth-level jets and reconstructed jet kinematics[42].

3.3.2 Tau lepton reconstruction

Only hadronically decaying tau leptons play a role in the reconstruction because taus that decay leptonically cannot reconstructed by their decay products. Tau leptons are seeded by jets that fullfil the following conditions:$p_T \geq 10\,\text{GeV}$, $R = 0.4$ and $|\eta| \leq 2.5$. For every tau seed the best vertex is found via a vertex association method.

Track association

The next step is to associate tracks to every tau candidate. Tracks that lie within a core cone of $\Delta R \leq 0.2$ are assigned to tau candidate if they pass the following criteria:

- $p_T \geq 1\,\text{GeV}$
- At least two pixel hits
- At least seven pixel and SCT hits combined
- $|d_0| \leq 1.0\,\text{mm}$
- $|z_0 \cdot \sin(\Theta)| \leq 1.5\,\text{mm}$

with d_0 being the impact parameter and z_0 the longitudinal one(see Sec.3.5.2) The number of tracks within the core cone dictates whether the tau candidate is classified as a single or multi-prong. Tracks that satisfy the criteria above but are isolated meaning $0.2 < \Delta R \leq 0.4$ are considered for variable calculation.

Identification of tau lepton

The tau reconstruction is not very helpful in distinguishing hadronically decaying tau leptons and jet background because they are the main background source. There are two methods used for identification, boosted-decision trees can be used and a likelihood method.
An algorithm called $\tau_{had-vis}$-identification (tau ID) is one of the methods used in discriminating between jets and $\tau_{had-vis}$. Training candidates have to pass a few criteria to ensure a good reconstruction. Furthermore, to raise the number of high p_T tau candidates, simualtion samples with a greater boson mass were chosen. For the tau ID three different candidates are considered:

- 1-prong: candidates have only one reconstructed track that matches a true τ_{had} with one charged hadron

- 3-prong: candidates have three reconstruncted tracks that match as true τ_{had} with three charged hadrons

- Multi-prong: candidates have two or three reconstruncted tracks that match as true τ_{had} with three charged hadron

When dividing the number of truth $\tau_{had-vis}$ candidates that are identified by the algorithm with all true hadronic tau decays, one can set a identification efficiency. The background efficiency is described if one divides the number of background $\tau_{had-vis}$ by the amount of the total background $\tau_{had-vis}$ candidates.
The boosted-descision tree is trained at three working points called tight, medium, loose that are defined as target efficiency for 1-pring of 40 %,60 %, 70 % and for multi-prong of 35%,55%,65%, respectively. Many variables are useful in discriminating tau leptons from jet background by characterizing the shower shape becaue in general jets are wider than hadronic tau decays. Not all variables can be explained but a few are highlighted[43].

Discrimination against muon and electron

Another aspect that has to be mentioned is that taus have to be discriminated against other leptons like the muon and electron. The reason why an electron might be misidentified as a tau is that 1-prong $\tau_{had-vis}$ have a similar signature. A way to seperate them is by looking at properties that are decisive like the longer and wider shower by hadronic tau decays or transition radiation by the electron.
For different η regions and different variable the e-veto BDT was trained and then tested for different variables at three working points
The reason why muons might be misidentified as taus is not the same as for the electrons because as minimum ionizing particles they rarely leave enough energy in the calorimeters to be misreconstructed as $\tau_{had-vis}$ candidate. But a energy cluster and muon track can be asigned $\tau_{had-vis}$ candidate. In order to dismiss fake taus the default muon reconstruction algorithm can be applied for which a $\tau_{had-vis}$ cannot overlay geometrically with a reconstructed muon

3.3.3 Muon lepton reconstruction

To identify a muon tracks are reconstructed in the inner detector and the muon spectrometer in which the track reconstruction is split into three stages. The first step is to look for hit patterns in the spectrometer. If a chamber has multiple close hits a line called segment is formed. Segments are combined to creating a track fit with respect to the inhomogeneous magnetic field. The track is extrapolated to the interacting point in the inner detector[44].

There are three different classes of muons.

- Stand-alone muons(SA): The track reconstruction was only made in the muon spectrometer. By interpolating the track to the point of closest approach of the beam line, the impact parameter and the direction of flight near the interaction point is estimated

- Combined muons(CB): The track is reconstructed independently in the muon spectrometer and in the inner detector and then combined

- Segment-tagged muons(ST): A track that is reconstructed in the inner detector and when extrapolated is aligned with at least one segment in the muon spectrometer, the track is assigned as a muon

3.3.4 Missing transverse energy reconstruction

Missing transverse momentum

Another important variable is the missing transverse momentum p_T^{miss} or its magnitude the missing transverse energy E_T^{miss}. After the proton-proton collision momentum is expected to be conserved in the plane perpendicular to the beam axis. When adding up the measured momentum in the calorimeters missing energy points to undetectable particles like neutrinos and BSM particles. Summing up the missing four-momenta of all measured particles in every calorimeter and the muon spectrometer[45].

$$\begin{aligned} E_{x(y)}^{miss} = E_{x(y)}^{miss,e} + E_{x(y)}^{miss,\gamma} + E_{x(y)}^{miss,\tau} + E_{x(y)}^{miss,jets} + E_{x(y)}^{miss,softjets} \\ + E_{x(y)}^{miss,calo,\mu} + E_{x(y)}^{miss,CellOut} + E_{x(y)}^{miss,\mu} \end{aligned} \tag{3.8}$$

$E_{x(y)}^{miss,calo,\mu}$ describes the energy that the muon lost in the calorimeter and $E_{x(y)}^{miss,CellOut}$ describes cells that are not counted towards any electrons or photons. By adding every cell associated with different particles for both coordinates, the value of E_T^{miss} is calculated as such:

$$E_T^{miss} = \sqrt{\left(E_x^{miss}\right)^2 + \left(E_y^{miss}\right)^2} \tag{3.9}$$

3.4 Monte Carlo Simulations

Monte Carlo simulations are very important part of research because the measurements need to be compared to a frame of reference. To give a full picture of reality the physics itself has to be calculated and simulated and the response to said physics when measuring it has to be simulated. Thus, the Monte Carlo method is divided into two parts, the simulation of the events and the simulation of the detector. For this method the simulation is generated by PYTHIA, herwig++ and SHERPA. In the Z-boson sample, background estimations were made up to next-to-next-to-leading order(NNLO) in the perturbation expansion. The Monte Carlo of the W samples is evaluated at NLO level and additional higher-order QCD and electroweak corrections were included.

3.4.1 Event Generation

After many measurements one can calculate the probability for certain decays. Central to the Monte Carlo Method is the use of random numbers. In the case of particle physics one does not know all the particles that are produced after the beam collision but by picking random numbers and simulating the different decay channels probabilities for the physical process can be generated. In order to properly compare measurement with Monte Carlo it has to be updated and maintained. Current theoretical predictions have to be included to produce reliable physical simulation in order to cover each step from the hadron colission to the hadronisation[46].

The first step is a hard scattering process, namely the proton-proton collision which is described by the matrix elements of perturbation theory. What follows is a parton shower algorithm that considers the internal structure of the jets. Further, radiative corrections due to electrodynamics are taken into account. The hard scattering process does not acknowledge the possibility of multiple partons colliding at the same time. This is not a dominant process but has to be included. The last step, the hadronisation in which partonic final states move to the actual hadronic bound state, is not described fully but modeled due to its non-perturbative nature[46].

3.4.2 Detector Simulation

Another important part is to simulate the response the detector because one has to take into account the precision and shortcomings of the detector. No detector is perfect and has a limited resolution. Every single interaction of a particle with detector components such as the calorimeters and the tracking strips are simulated when particle are interacting with them. Basically, a virtual detector is modeled, from its geometrics, to the material used, to the magnetic fields and their response[47]. The program which handles all of these tasks is called GEANT4.

By comparing the data with the Monte Carlo simulation one can find areas in which the simulation might differ and can be improved, treating it like a detector and performance study. Another aspect of using Monte Carlo is that it can give an idea of what to focus on or what challenges might arise. Taking data is scarce so one has to use Monte Carlo.

3.5 Vertexing and impact parameter reconstruction

This section discusses the methods with which particle vertices at ATLAS are selected and reconstructed. The precise localization of the primary vertex which describes the point of a proton-proton interaction is crucial for every following measurement. Then the reconstruction of the impact parameter is examined.

3.5.1 Primary Vertex Reconstruction

The method consists of two parts, first an algorithm is responsible for finding the primary vertex and second, an algorithm which takes care of fitting the vertex position. A challenge will be the effect of pile-up which describes multiple inelastic proton-proton collision[48].

The vertexing process is an iterative method that sorts out step by step tracks that do not fit the criteria or are not compatible with the vertex. The finding algorithm follows the track from the inside of the detector to the outside while the fitting algorithm works the other way around. To identify particle tracks space points from the pixel and the SCT detector are used to determine possible tracks that will be reconstructed by using a χ^2 fit that sorts out candidates with a poor fit.

The χ^2 method checks how much an observed distribtution diviates from the expected one. The value of χ^2 is calculated like:

$$\chi^2 = \sum_i^N \frac{(x_i - y_i)^2}{y_i}, \tag{3.10}$$

with x_i being the measured value and y_i the expected one. Depending on how many degrees of freedom there are and what kind of statistical significance is looked for, the value of χ^2 decides if a fit was acceptable.

Next, a seed position for the first vertex is chosen. It has to be situated in the beam spot which is the point of beam interaction Now an iterative χ^2 fitting method is looking for the tracks that best fit the vertex position. For this a weight is assigned to each track that will be changed after each step of the algorithm depending on the track's compatibility and the vertex is recomputed. A pool of incompatible candidates is formed that will be used for the iteration of another vertex position. Incompatible candidates are tracks that are more than 7σ away from the vertex. The process is repeated with the unused tracks until all tracks are used and the vertices have at least two associated tracks[49].

The criteria for tracks that will be used for the reconstruction algorithm is shown below[50]:

- $p_T > 150\,\text{MeV}$

- $|d_0| < 4\,\text{mm}$
- $\sigma(d_0) < 5\,\text{mm}, \sigma(z_0) < 10\,\text{mm}$
- Four or more hits in the semiconductor tracker
- Six or more hits in the pixel and SCT detector

A limitation for the impact parameter was chosen to eliminate tracks that originate from secondary interaction.

In Fig.3.6(a) a distribution of the reconstructed vertex is displayed in which it can be seen that the vertices have a wide distribution but are heavily peaked which indicates that the reconstruction algorithm is working as intended.

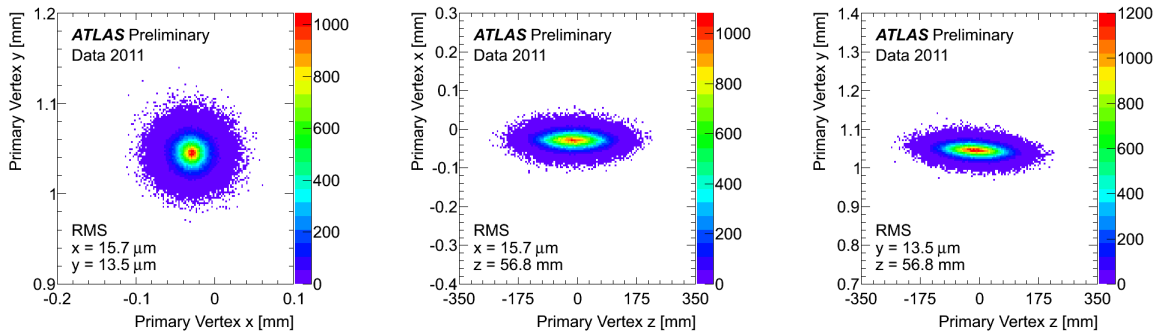

(a) XY plane (b) XZ plane (c) YZ plane

Figure 3.6: Reconstructed vertices distribution for different projections at $\sqrt{s} = 7\,\text{TeV}$. Every point has at least three reconstructed vertices. Most reconstructed track are found in the center of the distribution[51]

3.5.2 Impact Parameter

The impact parameter(IP) is considered an important observable in reconstructing vertices near the beam line and interacting point. The Fig.3.7 shows a particle track in relation to the coordinate system of the detector. The transverse impact parameter d_0 is defined as the closest point of approach of the curved particle track in the x-y plane to the beam line. The longitudinal impact parameter z_0 is defined as the z component of d_0 as can be seen in the figure.

Due to the high mass of certain particles a short lifetime and thus a short propagation distance is inevitable. A more visual representation of the impact parameter is shown in Fig.3.8 where the blue primary vertex is the spot of beam collision. Particles that are created at the primary vertex would propagate in all directions and would be absorbed in one of the calorimeters or form jets. A heavy particle, like the tau for example, would travel a short distance in the detector before decaying and thus creating a secondary vertex to which seemingly misplaced tracks would point to, indicated by the red dashed lines. If you trace back the secondary vertex one can define a vertical displacement d_0, the impactparameter, as shown by the blue dashed line and a longitudinal displacement z_0.

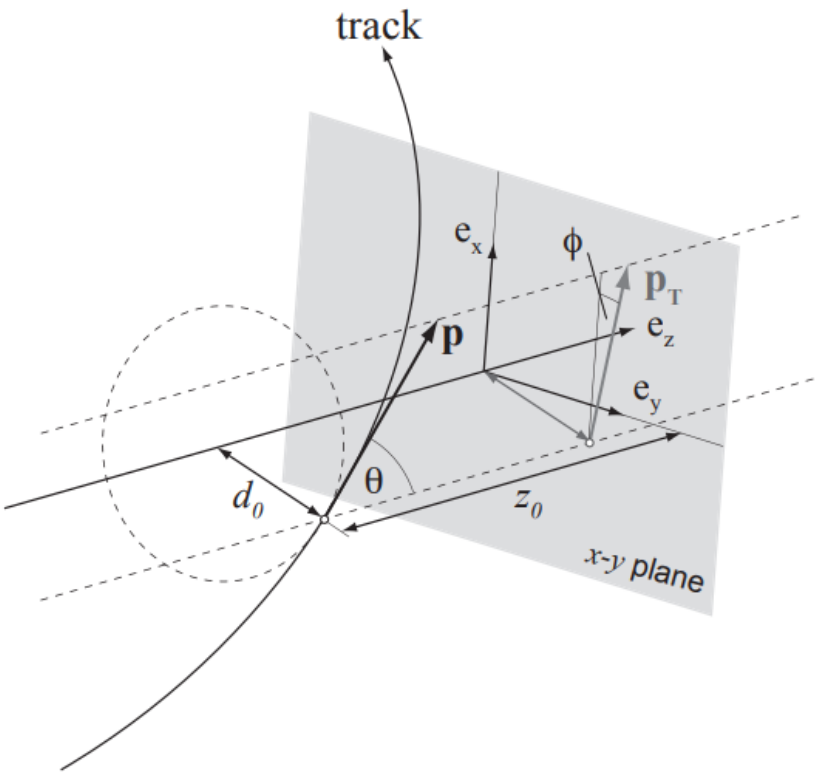

Figure 3.7: Threedimensional visulation of the transverse and lognitudinal impact parameter in the coordinate system of the ATLAS detector[52]

Resolution of the impact parameter

The impact parameter resolution can be approximated by [54]:

$$\sigma = \frac{r_1\sigma_2 \oplus r_2\sigma_1}{r_2 - r_1} \oplus \frac{k_1 r_1}{p_T} = A \oplus \frac{B}{p_T} \tag{3.11}$$

r_1, r_2 and σ_1 and σ_2 stand for the first and second layer of the inner detector, respectively. The root-mean square of the multi scattering angle at the first layer is explained by $\frac{k_1}{p_T}$. A and B do depend on $|\eta|$ but not p_T.

As can be seen in the equation above the resolution does decrease for higher momentum for fixed pseudorapidity. This can be explained by the multiple scattering which dominates at low momentum. When the momentum is fixed the resolution of the transverse impact parameter does increase for higher $|\eta|$, as seen in Fig.3.9(a) where the reseolution for $p_T = 1\,\text{GeV}$ and $p_T = 200\,\text{GeV}$. For the longitudinal impact parameter the resolution first decreases and then increases as shown in Fig.3.9(b) for two different momenta.

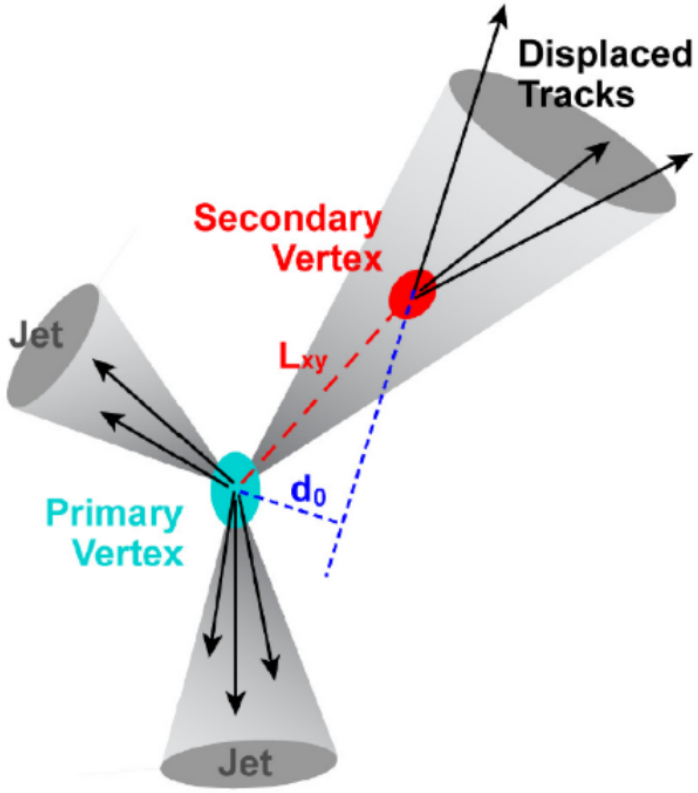

Figure 3.8: Representation of the primary vertex in blue and the displaced secondary vertex in red. The impact parameter d_0 is shown as the vertical displacement of the vertex compared to the center of the coordinate system[53]

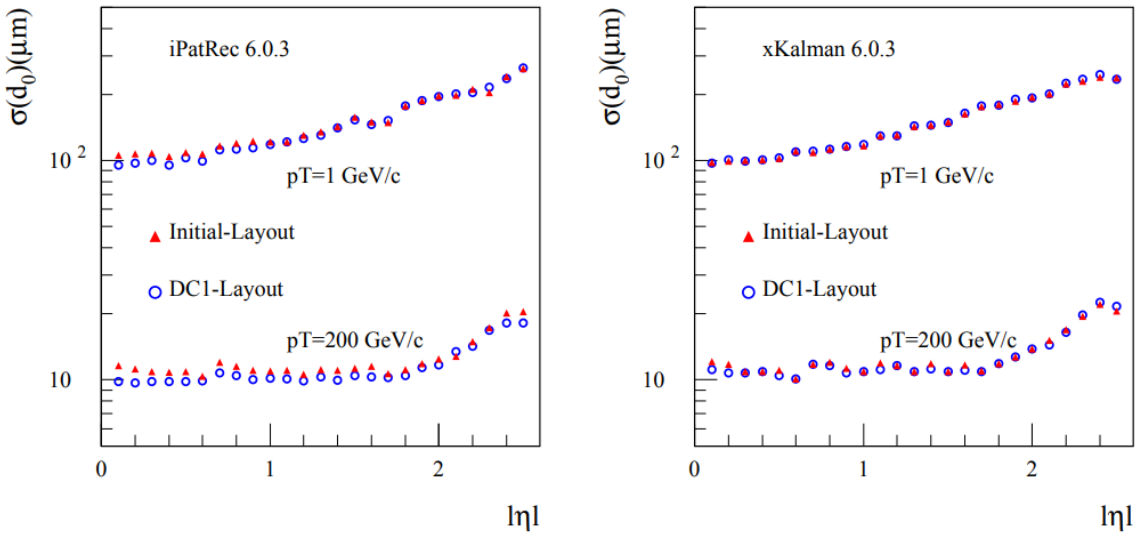

(a) Resolution of the transverse impact parameter d_0

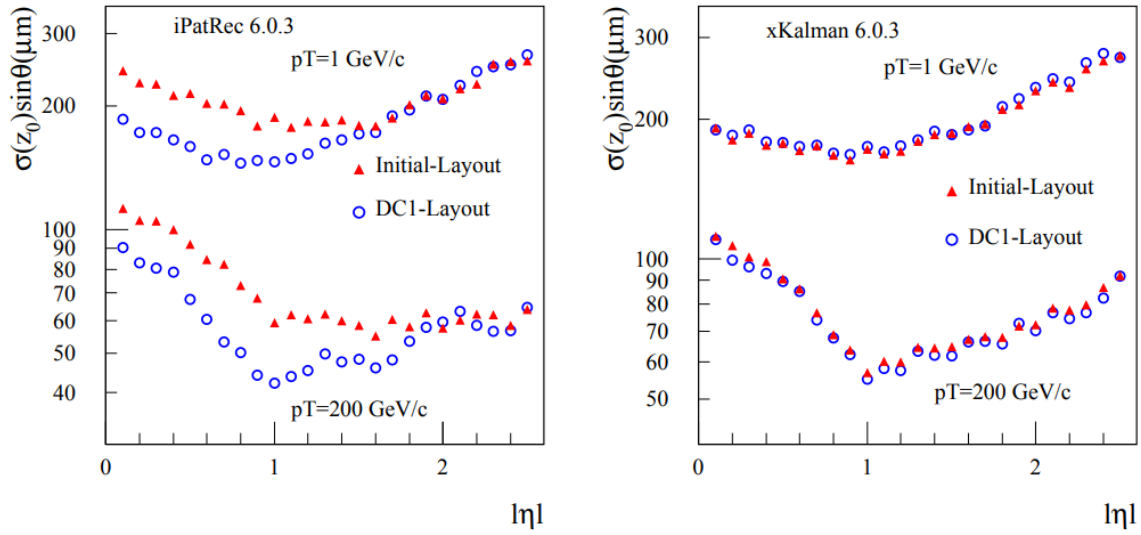

(b) Resolution of z_0 projected transversely to the track direction

Figure 3.9: Resolution of the impact parameter as a function of $|\eta|$ for two reconstruction programs. The blue and red points represent two different detector layouts. The upper points correspond to low momentum at $p_T = 1\,\text{GeV}$ while the lower points correspond to high momentum at $p_T = 200\,\text{GeV}$[54]

CHAPTER 4

Overview of the Analysis Strategy

In the following chapter the basic idea of this thesis' analysis will be presented to give the reader an understanding of how the lepton universality will be measured.
Because this thesis is based on the analysis of the W-boson mass measurement in proton-proton collissions at $\sqrt{s} = 7\,\text{TeV}$ and $\sigma = 4.6\,\text{fb}^{-1}$ of integrated luminosity in 2011 with the ATLAS detector at LHC and published in 2018[55], a short summary of its strategy and results are given in Sec.4.2[56].

4.1 Motivation

In Fig.4.1 the changing world average of the W-boson mass over the years starting in 1998 is shown. The upper panel displays the value for the m_W with a yellow line and its uncertainty in blue while the lower panel shows the decrease of the relative uncertainty in yellow.

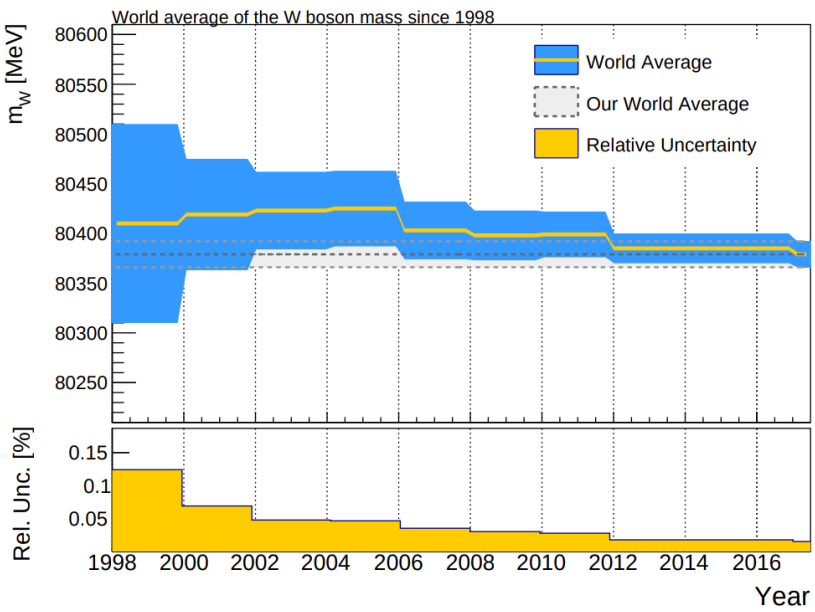

Figure 4.1: Evolution of the world average of the W mass over years since 1998. The upper plot shows the world average as a yellow line and its uncertainty in blue. The lower plot shows the relative uncertainty in yellow[19]

An improvement of the W-boson mass and its uncertainty is highly beneficial because at the lowest

order of electroweak theory m_W can be expressed in the following way:

$$m_W^2 \left(1 - \frac{m_W^2}{m_Z^2}\right) = \frac{\pi\alpha}{\sqrt{2}G_\mu}(1 + \Delta r), \tag{4.1}$$

such that the mass depends on the fine-structure constant α, the Fermi constant G_μ and the Z-boson mass. Δr is an additional influence that includes higher-order corrections. By putting limits on the W-boson mass theories for physics beyond the Standard Model are constrained.

4.2 Analysis of the W-boson mass

This section summarizes the most important aspects of the analysis of the W-boson mass as described in [56]. In it the ATLAS detector, the particle reconstruction and the generators are detailed. They do not need to be described because the ATLAS detector, the particle reconstruction of the W and Z boson candidate events was already explained and can be found in Sec.3.2 and Sec.3.3, respectively, while the samples and generators are discussed in Sec.3.4.

4.2.1 Important observables

Before the event selection will be discussed, a short explanation of important variables is made.

Transverse lepton momentum

The momentum of a particle can be split into its different components depending on the coordinate system. For particle in a detector the transverse momentum is the component perpendicular to beam axis and should be equally distributed. Bunches in the beam that do not interact with each other as they pass along the beam pipe with unchanged momentum. Transverse momentum of a particle originates from an interaction at the vertex that changes the direction. Under a boost along the beam axis p_T is lorentz invariant.

$$p_T = \sqrt{p_x^2 + p_y^2} \quad or \quad p_T = p \cdot \sin(\theta) \tag{4.2}$$

Transverse boson mass

Measuring an invariant mass for the boson is met with difficulty since the neutrino passes the detector undetected. Instead, an analogous mass that is calculated by looking at the transverse components of the lepton momenta.

$$m_T = \sqrt{2p_T^\ell p_T^{miss}(1 - \cos(\Delta\Phi))}, \tag{4.3}$$

with $\Delta\phi$ being the azimuthal opening angle between p_T^{miss} and the charged lepton. A look at the $\frac{1}{\sigma}\frac{d\sigma}{dm_T}$ would give a clear Jacobian peak at $m_T = m_W$ in the case the W boson decays at rest, otherwise the peak is smeared[57].

4.2.2 Event Selection

Hsigh luminosities ensure a high number of recorded data but there were few requirements applied to assure a promising data set. There are two types of selection made, the first one is the selection of the lepton and the second one is requiring the right kinematics. Before the signal cuts are applied several intermediate cuts reduced the number of events like a trigger matching or jet cleaning cut. Depending on what decay is the focus these cuts might differ. Muon candidates are required to have at least 18 GeV for the transverse momentum and electron candidates are required to have at least 20 GeV and 22 GeV for later data-taking periods. A reconstructed primary vertex with at least three associated tracks is a requirement for lepton events.
Leptons that pass the listed cuts below are considered signal events for the $W \to \ell\nu_\ell$ decay.citeAaboud:2017svj:

- Exactly one well reconstructed electron/muon
- $p_T^l > 30\,\text{GeV}$
- $p_T^W < 30\,\text{GeV}$
- $m_T^W > 60\,\text{GeV}$
- $p_T^{miss} > 30\,\text{GeV}$

A visualization of all cuts is displayed below in Fig.4.2(a) for the $W \to \mu\nu_\mu$ decay and is called Event Cut Flow. Before any cuts that guarantee a clean classification were applied $154 \cdot 10^6$ events were recorded. In the end $7.84 \cdot 10^6$ events were kept[55]. For the electron channel $5.89 \cdot 10^6$ events are selected.
Because the Z-boson decay is used as a calibration the event selection for leptons is listed below that selects $0.58 \cdot 10^6$ for the $Z \to ee$ decay and $1.23 \cdot 10^6$ for the $Z \to \mu\mu$ decay.

- Required to have exactly two leptons with $p_T^\ell > 25\,\text{GeV}$
- These two leptons have to carry opposite charge
- Invariant mass of the dilepton system in the range of $80 < m_{ll} < 100\,\text{GeV}$

4.2.3 Multijet background estimation

Because the multijet background cannot be sufficiently described by simulations, a data-driven method will estimate its contribution.

The way the multijet background was estimated is by template fitting the kinematic variables. These variables are m_T, p_T^{miss} and p_T^ℓ/m_T and will be looked at in two kinematic region in which signal requirements are loosened. For the first kinematic region cuts on the event selection for m_T and p_T^{miss} are reduced. For the second kinematic region the same definition holds true but also taking out the requirement on the transverse plane recoil. As estimation of the impact of multijet background in lepton channels is made because the mulitjet events have semileptonic decays which may end up in the signal channel.

Requirements that were used to isolate the lepton energy are inverted in order to obtain the templates of the multijet background distribution. To normalise the background estimation a fraction fit is applied that fixes the normalization of all decay channels except for the multijet one.

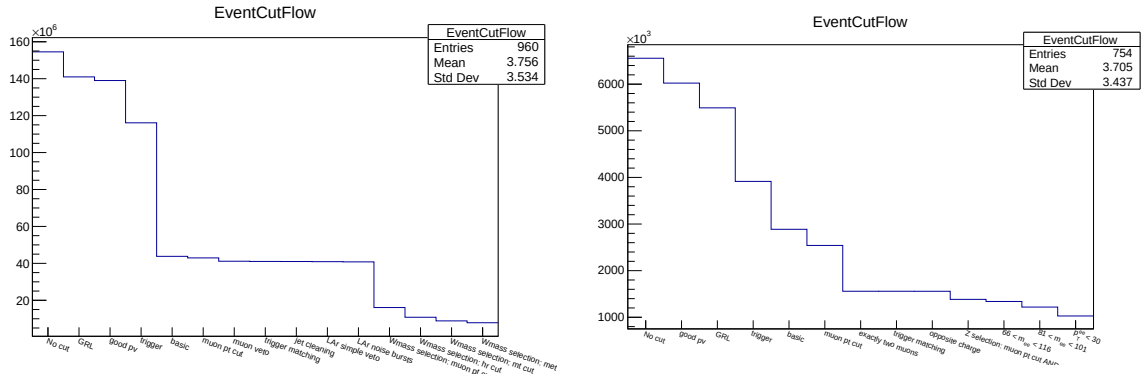

(a) $W \to \mu\nu$ (b) $Z \to \mu\mu$

Figure 4.2: Diagram represents the cut flow for the signal channel in W and Z decays. Y-axis shows the number of signal events for every cut on the x-axis.

4.2.4 Applied correction

Of high importance to the analysis are the correction to the electron, muon and recoil response.
The observables of interest like p_T^{ℓ} are influenced by the calibration of the lepton energy and the recoil. Because the Z-boson mass can be measured accutarely, it is helpful in calibrating the correction of the lepton momentum while the $p_T^{\ell\ell}$ is used to calibrate the recoil.

To correct the recoil three steps are taken. The first reweights the average interaction per bunch-crossing. Afterwards, the discrepancy in the ΣE_T is corrected. The difference of the observed azimuthal angle of the recoil distribution is corrected in the third step. These corrections are verfied by applying the same methods that are used to determine the W-boson mass on the Z-boson mass.

4.2.5 Fitting Procedure

The adopted strategy to atain the mass of the W-boson is by fitting the W boson transverse mass and the charged lepton transverse momentum of the leptonic channels $W \to \mu\nu$ and $W \to e\nu$. Different values of m_W are used to simulate the final-state distibution. A χ^2 function that depends on m_W is minimised to get the measured value.

The mass fitting is done in different categories like the charge and η region which are in the end combined for the final value of the mass measurement. Consistentcy of the result is helpful to test the experimental calibration in case of the lepton channels and W-boson production model in case of the η and charge categories. The systematic uncertainies result from the corrections to detector and recoil calibration, physics modelling and background substraction. Half of the width of the χ^2 functions determines the statistical uncertainties.

The final result is a consequence of combining the measurement of the different categories and is yielding:

$$\begin{aligned} m_W &= 80369.5 \pm 6.8\,\text{MeV}(stat.) \pm 10.6\,\text{MeV}(exp.yst.) \pm 13.6\,\text{MeV}(mod.syst.) \\ &= 80369.5 \pm 18.5\,\text{MeV} \end{aligned} \tag{4.4}$$

Currently, a reanalysis of the discussed measurement is in the works for which this analysis will be apart of. The reanalysis will be includ the electron and the 8 TeV data will be used to reduce uncertainty.

4.3 The Premise

When dealing with a highly complex experiment, especially in precise measurement, hindrances that complicate the analysis are to be expected.

In high energery physics such complications are surely the missing neutrino and heavy multijet background. For the leptonic W boson decay a neutrino is inevitable and only a single defined track in the detector is visible. This leaves room for plenty of uncertainties when it comes to locating the point of decay for a tau lepton even though a precise tracking would be of high interest and necessity. One way to clearly identify the particle track would be to install tracking detectors with a higher resolution. This is very costly and does require years of planing. For the Run 2 at ATLAS, a new most inner layer of the pixel detector was introduced. This analysis is based on Run 1 und therefore is not in possession of this new layer. Instead, one has to use other possibilities.

As already mentioned, the Z-boson decay will be used to calibrate the W-boson decay. This is possible because Z boson produces no neutrinos if it decays directly to muons or electrons. In the rest frame the lepton tracks are back to back giving two tracks that help in determinating the vertex position which results in an impact parameter distribution which should be closer to the expected one because uncertainties concerning the vertex position are reduced.

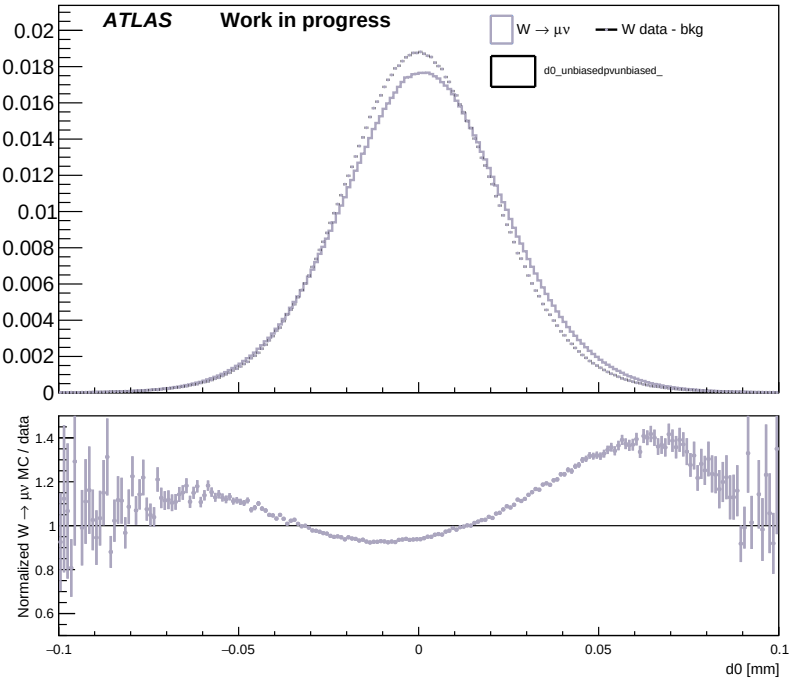

Figure 4.3: Disitribution of the d_0 parameter for the data signal minus expected background and the Monte Carlo for the $W \to \mu\nu$ decay. The lower panel shows the ratio of the data and MC

Further, one could compare the individual branching ratios of the leptonic but in many cases the measurement of the ratio of branching fraction is evaluated. The benefit of looking at the ratio is that experimental and theoretical uncertainties are expected to cancel out.

As stated above the Z decay should be better described thus the main premise of this analysis is using

the Z decay to calibrate the W decay which has more uncertainty concerning its vertex due to undetected neutrino. By utilizing the information of the Z decay one can put constrainsts on the W decay.

Over the course of this chapter and the next one this analysis will describe how the impact parameter was examined. This will be done by taking a look at the distribution of the impact parameter and how it changes if one applies specific cuts.

An example of the d_0 distribution is displayed in Fig.4.3 which includes the Monte Carlo and data signal distribution. Both follow a Gaussian distribution. The lower panel shows how well these two compare to each other. A good agreement would set the ratio to one but in this case the impact parameter is either underestimated by the Monte Carlo in the peak region or overestimated in the tail regions. The goal would be to find out in which case the measured impact parameter is well described by the Monte Carlo and to understand their differences. Another approach would be looking not only at the transverse impact parameter d_0 but the longitudinal one z_0 and the significance for both which are defined as the impact parameter divided by its uncertainty. They might be better modeled by the Monte Carlo such that a calibration would be more efficient.

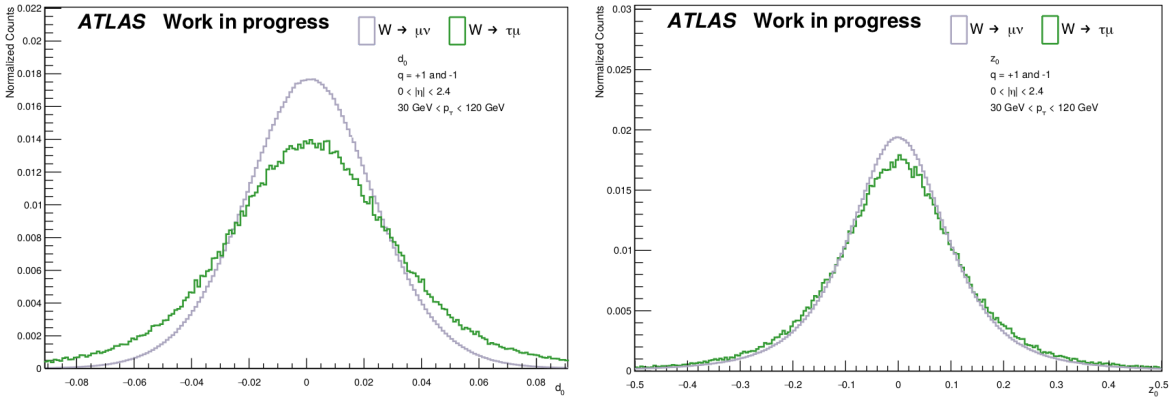

(a) Transverse impact parameter d_0

(b) Longitudinal impact parameter z_0

Figure 4.4: Normalized distribution $W \to \mu\nu$ in grey and $W \to \tau\nu$ in green

The Fig.4.4 shows the MC distribution of $W \to \mu\nu$ in grey and $W \to \tau\nu$ in green for d_0 in Fig.4.4(a) and for z_0 in Fig.4.4(b). These two demonstrate that the distribution of the two decays differ. In the case of the longitudinal impact parameter z_0 one sees little differences in the shape but the distribution is slightly wider for the tails. This difference is much more visible in the case of d_0 where tails are clearly wider. This means that d_0 is expected to be much better for separating these two decays. The next chapter is going to determine which observable is better suited for this analysis.

4.3.1 Calibration

This section presents the basic idea of the calibration applied in this thesis. As already mentioned the Z-boson decay will be used in order to calibrate the W-boson decay. In the previous section the Fig.4.3 was briefly described. It was mentioned that a good agreement between the Monte Carlo and data results in a flat ratio. The same can be done for the Z-boson decay. In this case the lower panel shows the ratio of the Monte Carlo and the data of the Z decay. A flat ratio indicates that the Monte Carlo is modeling the distribution, from the tails to the peak, in the same way the data was recorded. It may be possible that much more data was taken that simulated but as long the Monte Carlo follows the same shape as the data the ratio is flat. Unfortunately, many distribution are not well modeled by the Monte Carlo for W and Z

decays. Because the individual ratios do not stay constant the idea is to look at the ratio of the ratios, called double ratio. If the ratios of both decays are not flat or mismodeled in the same way, the Z decay can be used for calibration.

The next section is going to present the binning of the impact parameter histograms. In the next chapter the calibration of the impact parameter and the determination of its uncertainties are explained.

4.4 Optimized Binning

4.4.1 Binning of the impact parameter

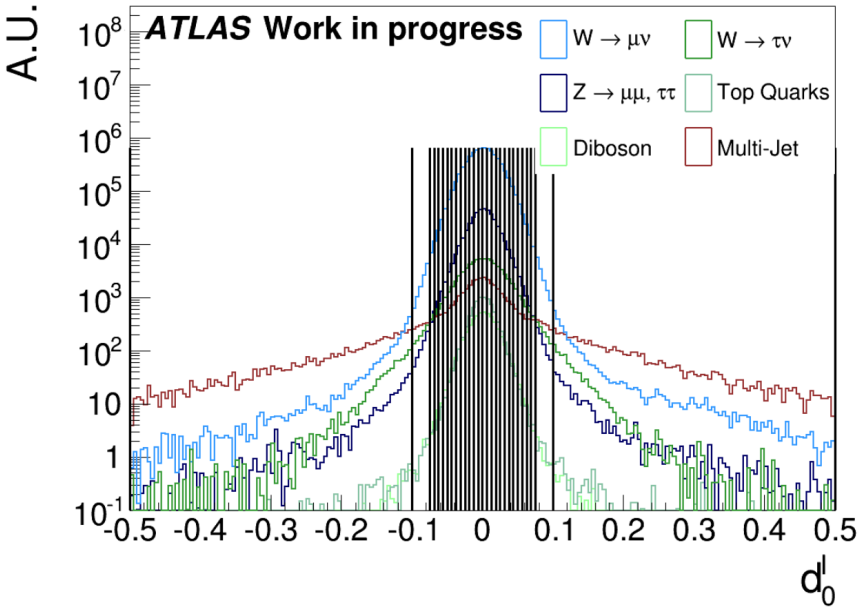

Figure 4.5: Binning study by a bachelor student. Vertical lines mark the borders of a new bin. X-axis is in mm. Different colored lines represent different decay channels in log scale.[58]

One reason for a new binning is decreasing the statistical uncertainty for the final fit. Another reason is good statistics per bin which is necessary for the fitting procedure. A previous study by a bachelor student was done concerning the number of bins for the histogram of the transverse impact parameter. For this the distribution of the impact parameter for the different channels were analyzed in how much the statistical uncertainty of the ratio of the branching fraction changes for different types of binning.

The bachelor thesis did analyze the effect of the binning on the stastical uncertertainty of the ratio of the branching fraction. The change of uncertainty was documented for the configuration: p_T binned in different variables like the $|\eta|$, d_0 and the electrical charge. The smallest uncertainty could be obtained by combining all variables. Taking both decay channels into account, electronic and muonic one, the statistical uncertainty was 2.095% for p_T binned in $|\eta|$, d_0 and both electrical charges with 28 bins. Without any additional configuration the statistical uncertainty is 3.58% for electrons and muons combined.

The conclusion was to take very thin bins in the middle of the distribution and very few for the tails as shown in Fig.4.5. Taking a close look one can see that bin starting at |0.1| sits roughly at a point where the blue crosses the red line. At this point the signal(blue) is more dominant than the multijet

background(red). The next bin starts where the red line crosses the dark green one. From this point on the decay to tau(dark green) is more dominant than the multijet background. Beware that the y-axis is in log scale which means that differences are much bigger than they seem.

The binning for d_0 was adopted from the bachelor thesis. But there is a slight difference. The range for d_0 distribution as seen in Fig.4.5 spans from -0.5 mm to 0.5 mm. In this analysis the range of d_0 covers -0.1 mm to 0.1 mm which can be seen in Fig.4.3. Thus, a binning was chosen for which the outer bin ends where the red line crossed the green one in Fig.4.5. This leads to a binning for which the center of the distribution has equidistant binning until $d_0 = |0.075\text{ mm}|$ and than one wide bin from |0.075 mm| to |0.1 mm|. This binning can be looked up in Tab.4.1.

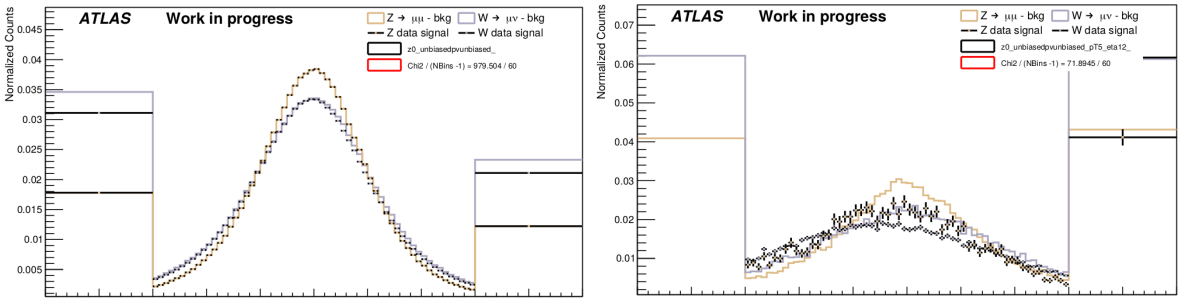

Figure 4.6: Two z_0 distributions that show a new binning trial. That underestimated the outer bins. X-axis in mm

A new binning is applied to the other observables such as z_0 and the significance of d_0 and z_0. Because they have a different range the binning is going to differ. The distribution of z_0 is much broader. In fact, the idea of starting a new bin at the point where two channels cross line as described above is not the same for z_0. In the chosen range the red line never crosses the blue line and the red and dark green one intersect close to the center as seen on left side Fig.4.6. For z_0 a similiar approach was taken as in Fig.4.5, a wide bin at both sides from $|0.3\,\eta|$ to $|0.5\,\eta|$. In the middle are sixty equally distanced bins.

A problem that arose for this binnin is that many events fall into the outer bins increasing the event count. An example for this can be seen in Fig.4.6. For variables with lower statistics the outer bins can get higher than the peak. To solve this problem the wide bin was divided into two regions with with different bin width. This can be seen in Fig.4.7(b) on the right side. The left side shows the old binning for which every bin has the same width. The exact width of the bins are listed in Tab.4.1.

$\|d_0\|$ range [mm]	Bin width [mm]	$\|z_0\|$ range [mm]	Bin width [mm]
0 - 0.075	30 bins with 0.0025	0 - 0.25	25 bins with 0.01
0.075 - 0.1	1 bin with 0.025	0.25 - 0.45	8 bins with0.025
		0.45 - 0.5	1 bin with 0.05

Table 4.1: New binning for the d_0 and z_0 distribution

Because the significance of d_0 and z_0 depend on these observables their binnings are chosen accordingly, such that they cover the same ratio of range. That means that for the $d_0/\sigma(d_0)$ distribution the binning consists of equidistant bins that cover the same percentage as for d_0 and one wide bin. For the significance of z_0 the same measures to prevent overfilled bins were taken. The new binning for these observables are listed in Tab.4.2.

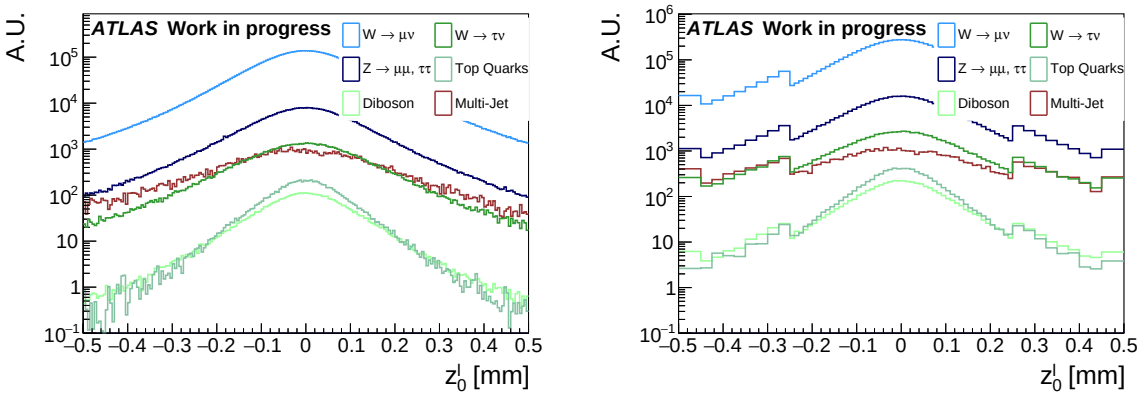

(a) z_0^ℓ for equidistal bins

(b) z_0^ℓ with new binning

Figure 4.7: Logarithmic plot of impact parameter variable and the different decay modes of the W boson.

$\lvert d_0/\sigma(d_0)\rvert$ range [mm]	Bin width [mm]	$\lvert z_0/\sigma(z_0)\rvert$ range [mm]	Bin width [mm]
0 - 3.0	30 bins with 0.1	0 - 2.0	25 bins with 0.08
3.0 - 4.0	1 bin with 1.0	2.0 - 3.6	8 bins with 0.2
		3.6 - 4.0	1 bin with 0.4

Table 4.2: New binning for the significance of the d_0 and z_0 distribution

4.4.2 Binning of the pseudorapidity and transverse momentum

The impact parameter is not the only variable that needs a new binning. In order to analyze the distribution of the impact parameter under different aspects it would be helpful to introduce other observables for which the distribution can change.

Pseudorapidity

The pseudorapidity was defined in Sec.3.2.1. The distribution is binned in four η slices from $0 < |\eta| < 2.4$ in steps of 0.8, 0.6, 0.6 and 0.4. This matches the η binning applied in the W-boson mass analysis described in Sec.4.2 otherwise the fit would not work. The η distribution for the W-boson decay and its different decay modes is shown in Fig.4.8. Furthermore, the mentioned binning is included by adding vertical lines. The old binning is still visible and clearly shows how the events per bin differ. Depending on the η bin and decay mode different number of events are registered.

Transverse Momentum

On the left-hand side the distribtution of the transverse momentum is shown with vertical lines for the binning. The first three bins contain the bulk of the peak, the fourth bin is chosen to be wider because the distribution drops off, the last bin is open to include any event that is part of the tail but will not be included in the mass fit.

In Fig.4.9 the distribution of the transverse momentum for the W-boson decay and its different decay channels is plotted. It is divided into five bins. The first three bins cover the bulk of all events. The next one is chosen to be wider because fewer events are detected in that range. The last bin is open to

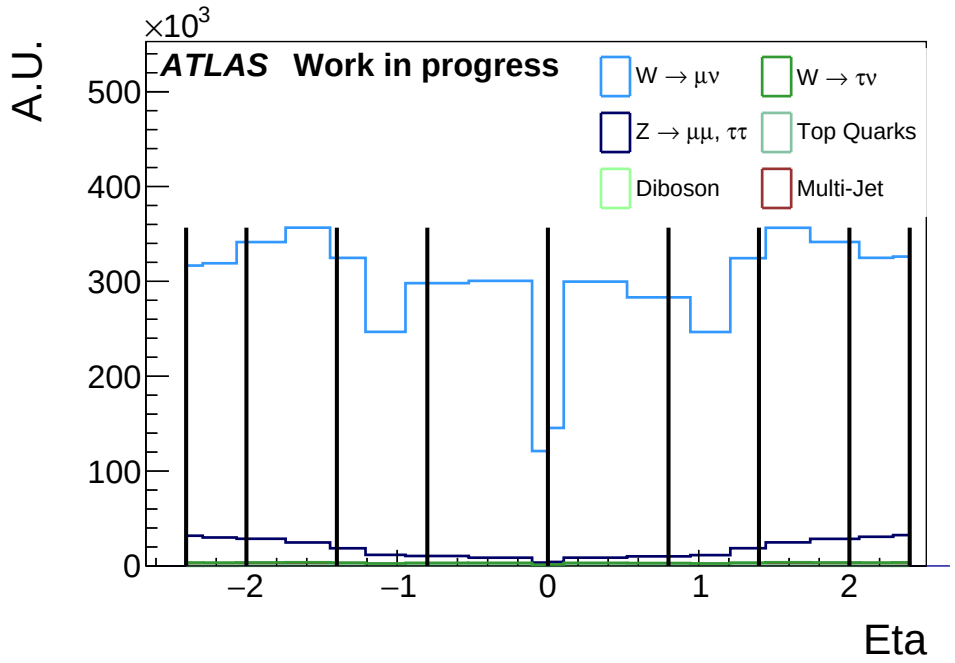

Figure 4.8: Distribution and binning of η for the W-boson decay shown as colored histograms. Vertical lines mark bin

include any event that is part of the tail but will not be included in the mass fit. The shown plot starts at $p_T = 30\,\text{GeV}$ because that is lower threshold for a signal event as stated in Sec.4.2.2. The binning of p_T is listed in Tab.4.3.

$\lvert\eta\rvert$ binning	p_T binning [GeV]
0 - 0.8	30 - 34
0.8 - 1.4	34 - 38
1.4 - 2.0	38 - 42
2.0 - 2.4	42 - 50
	50 -

Table 4.3: Binning for the $|\eta|$ and p_T

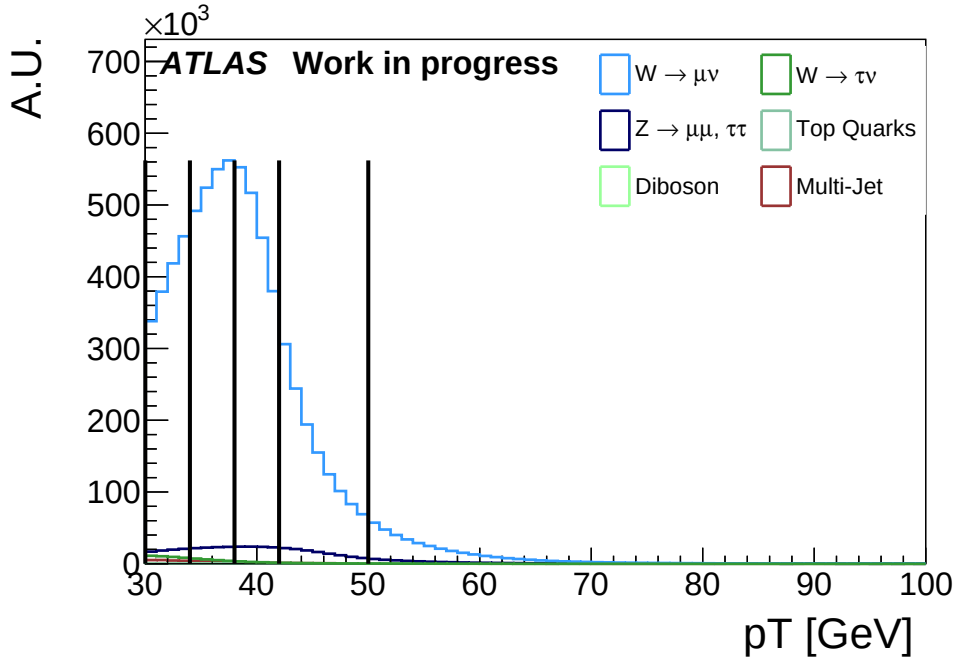

Figure 4.9: Distribution and binning of p_T for the W-boson decay and its decay different decay modes shown as colored histograms. Vertical lines mark bins

CHAPTER 5

Calibration and uncertainties of the impact parameter reconstruction

This chapter details a step by step explanation of the calibration of the impact parameter that was applied for this analysis. Additionally, a way to determine the uncertainty of the calibration will be discussed at the end of this chapter. Due to the determination of systematic uncertainties, every observable used was split up into the two electrical charges, four distinct η bins and different bins of the transverse momentum

5.1 Outline of the calibration method

5.1.1 Calibration weights

The basis for the calibration is the distribution of the impact parameter as already seen in the previous chapter in Fig.4.3 which is split in two parts. The upper part for the distribution of the Monte Carlo and data for W-boson decay, and the lower part which shows the ratio of these two distribution. The next step is adding for the same observable the impact parameter distribution of the Z decay. An example of this is shown in Fig.5.1(a).

Here, the distributions of the W decay are plotted in grey while the data and Monte Carlo of the Z-boson decay is shown in brown. The lower panel displays the ratio of data to Monte Carlo for both decay in their respective colors. For the shown observable, d_0, both ratios are not flat. In the case of the W-boson decay the data is underestimated by the Monte Carlo in the center of the distribution while it is overestimated for the tails. For the distribution of the Z-boson decay, it is the other way around. The data is higher than expected in the middle and lower for the tails.

The next step is to form the aforementioned double ratio which is just dividing the ratio for Z-boson decay by the ratio for the W-boson decay. This double ratio will be plotted on the lower panel in black and can be seen in Fig.5.1(b). In this case the double ratio exhibits a Gaussian like shape that is far from being flat. This is due to the distributions of the W and Z decay being mismodeled in different ways.
With the double ratio introduced the next step would be to find a way to quantify the flatness of said ratio. This will be done by fitting a straight line to the double ratio and checking how well it matches. This can be seen in Fig.5.2 in which the fit is a red line on the lower panel. How much the line fits the double ratio is quantified by a χ^2 test. Its result is displayed as part of the legend in the upper panel. For the shown case then the line does fit the double ratio very badly which is already clear by looking at it alone.

As there is no good agreement between the Monte Carlo and the data, each muon is mulitplied a weight which is calculated such that the Monte Carlo matches the data for the $Z \rightarrow \mu\mu$ decay. If these weights

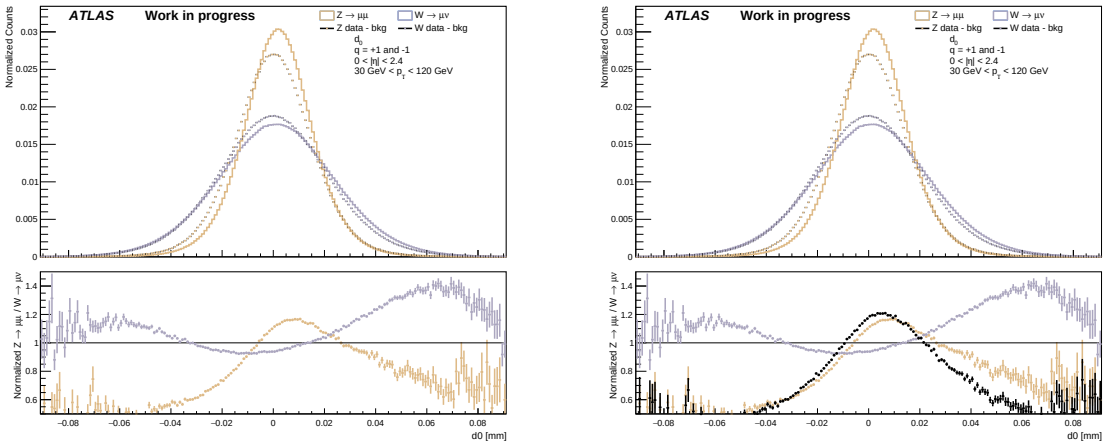

(a) Ratio of MC and data

(b) Double Ratio in black

Figure 5.1: Distribution of d_0 for Z and W decay plotted in brown and grey, respectively. Lower panel shows the ratio of data to MC for both decays in their respective colors.

are applied correctly the ratio on the lower panel should show no deviation from one. This is confirmed in the plot below. Fig.5.3(a) shows the calibrated Monte Carlo distribution of the Z-boson decay which is perfectely aligned with the data and thus the calibration procedure has been correctly implemented.

For every bin i in the d_0 histogram a weight w_i is calculated as follows:

$$w_i = \frac{d_i}{MC_i}, \tag{5.1}$$

with d_i and MC_i being the value for the data bin i and MC bin i, respectively. These are the weights that were multiplied to the distribution of the Z-boson decay in Fig.5.3(a).

The same weights are applied to every muon from the $W \rightarrow \mu\nu$ in Fig.5.3(b). A reweighting does not change the double ratio because the same weights are applied to both distributions. That means the flatter the double ratio the more the Z and W decay distributions are similiar and the more the calibration aligns the data and the Monte Carlo of the W-boson decay. It has to be noted that there is a possibility for a Monte Carlo bin being empty or even negative entries. This is because of detector ineffencies. In the case of empty bins this would create infinite weights and for negative bin entries it would result in negative weights. Both cases are not practical. For those edge cases the weight is set to one.

As can be seen by this example, after the calibration the distribution of the $W \rightarrow \mu\nu$ decay is very badly described by the Monte Carlo. This is due to the unflat double ratio. For this reason it is of uttermost importance that the double ratio is flat in order for the calibration to work.

5.1.2 Uncertainty of the calibration weights

After the calculation of the weights are established one has to look at how accurate the weights are.

To calculate the uncertainty σ for a certain bin i one considers the distance of the calibrated ratio of the W-boson decay to the fit of the double ratio. The exact way to determine the relative uncertainty is seen in Eq.5.2. The value of the uncertainty corresponds to the difference of the double ratio fit to the double ratio and how much they do not align. Great uncertainties indicate that either the fit did not perform well,

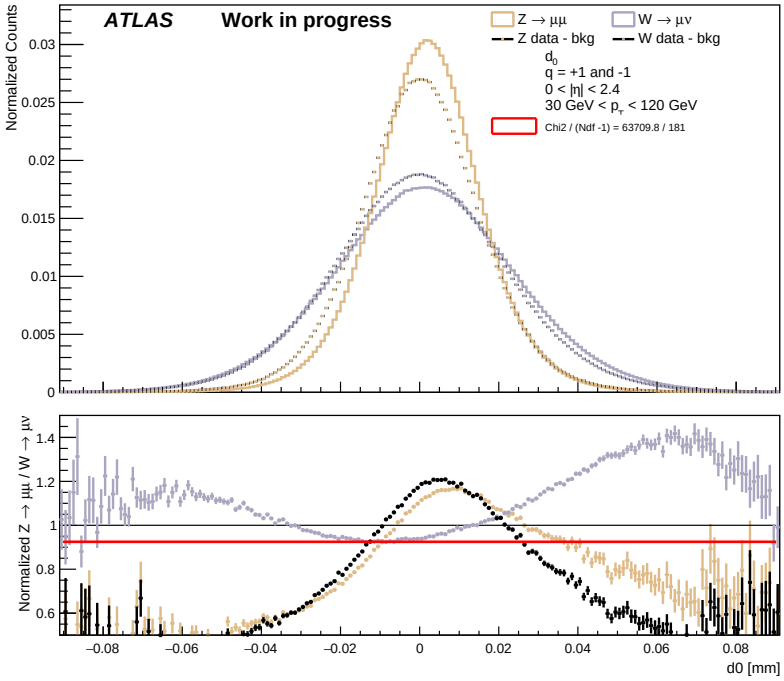

Figure 5.2: Distribution of d_0 for Z and W decay plotted in brown and grey, respectively. Lower panel shows the ratio of data to MC for both decays in their respective colors and a fit in red to the double ratio.

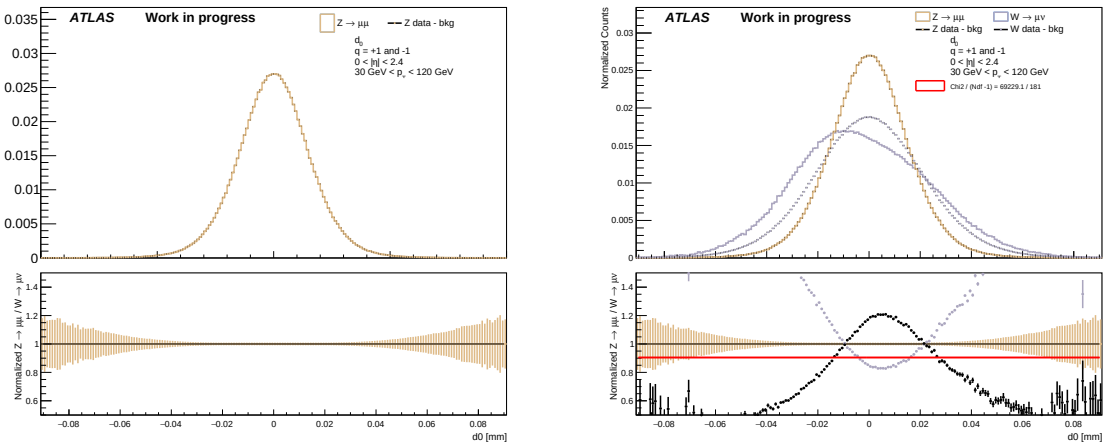

(a) Calibrated distribution of the Z-boson decay (b) Both distributions are calibrated with the weight

Figure 5.3: Inclusive d_0 distribution for MC and data is displayed on the upper plot. Lower plot shows the respective ratios. These plots demonstrate the effect of the calibration on the distributions

which is a possibility, or a certain bin deviates from a straight line .

$$\sigma_i = \frac{RrW_i - n}{n} \tag{5.2}$$

n is the value of the y-intercept of the double ratio fit and RrW is the reweighted ratio of the W-boson decay. This equation allows for uncertainty values with different signs. A change in signs means that the ratio switched from being smaller than the double ratio fit to being greater or vice versa.
In the case of the shown example the applied weights have a great uncertainty for most of the bins. Only in the center of the distribution are the reweighted bins of $W \rightarrow \mu\nu$ close to the double ratio fit.

To give a better understanding of how the calculation of the uncertainty of the calibration weight works a quick example is giving below. The plot in Fig.5.4 shows the distribution of the inclusive z_0. Due to the great amount of statistics the double ratio is flat and and the uncertainties small. The calibration weights that align the simulation of the Z-boson decay with its data is applied multiplied to distribtuion of the W-boson decay. The new ratio is seen on the lower panel in grey. To illustrate the uncertainty of the very first bin is going to be calculated. The calibration weight for said bin is $w_1 = 1.81$. Looking at the formula for the uncertainty Eq.5.2, the very first z_0 bin of the calibrated ratio is at 1.15 while the double ratio fits intercepts the y-axis at 0.95. With these two values the uncertainty can be calculated:

$$\sigma_1 = \frac{RrW_1 - n}{n} = \frac{1.15 - 0.95}{0.95} = 0.21 \tag{5.3}$$

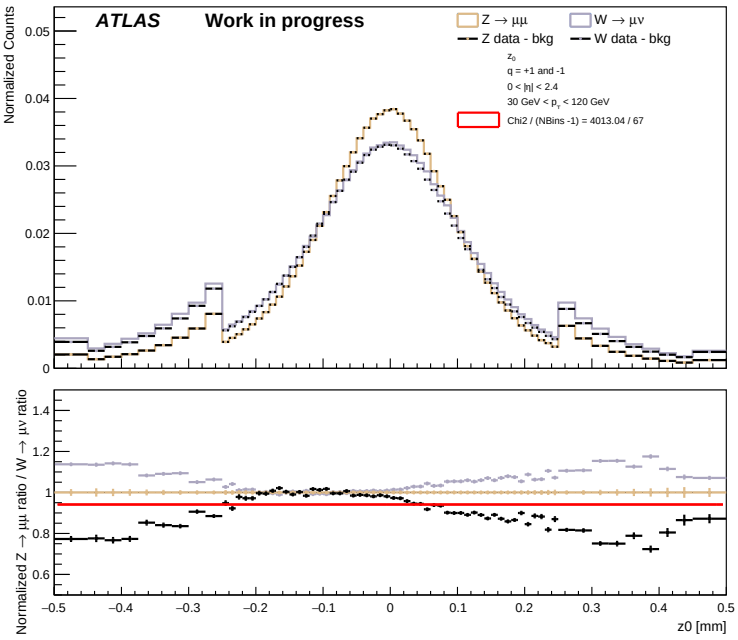

Figure 5.4: Calibrated distribution of the inclusive longitudinal impact parameter. Upper panel shows the data and MC of both boson decays. Lower panel shows the ratio of of MC and data for the W-boson decay in grey and Z-boson decay in brown. A red line is fitted to the black double ratio.

5.2 Choice of variable

The tranversal, longitudinal impact parameter and their significances were introduced in the previous chapter in Sec.4.3. This section explains the decision which observable will be used for the calibration of this thesis.

5.2.1 Flatness of double ratio

It is of uttermost importance to achieve a flat double ratio because this would ensure a succesful fit. This can be either be done by finding a binning that deal with the tails of the distribution where double ratio is most of the time not flat or looking for observables that are more flat that others. Furthermore, one can apply cuts and analyze how the level of flatness changes for these cuts.

Due to the determination of systematic uncertainties, every observable used was split up into the two electrical charges, four distinct η bins and different bins of the transverse momentum as described in Sec.4.4.2. The double ratio fit was done for every observable mentioned in Sec.4.3 and every cut.

To get an overview of the value of χ^2/ndf for different observables and cuts was plotted in Fig.5.5(a). For this plot not every cut was considered but the pseudorapidity and the charge cut. They can be seen on the x-axis and the different observables are highlighted in the legend. It is clear to see that the value of χ^2/ndf for d_0 and the significance of d_0 plotted in red and blue, respectively, are very high with one to two orders of magnitude difference to the other lines. This is a clear sign that the fit did perform very badly. But a trend can be seen. The worst performance was made for the plain observables with no cuts applied. For both observables the performance of the χ^2 fit improves the higher the η region is but it still far away from the performance of the green and violet line. These lines represent z_0 and the significance of z_0 and cannot be distinguished in Fig.5.5(a). A closer look at these two observables is made in Fig.5.5(b) for which the y-axis was limited. Again, a similiar trend is visible. The performance improves for z_0 and $z_0/\sigma(z_0)$ for both charges if one looks at high η cuts.

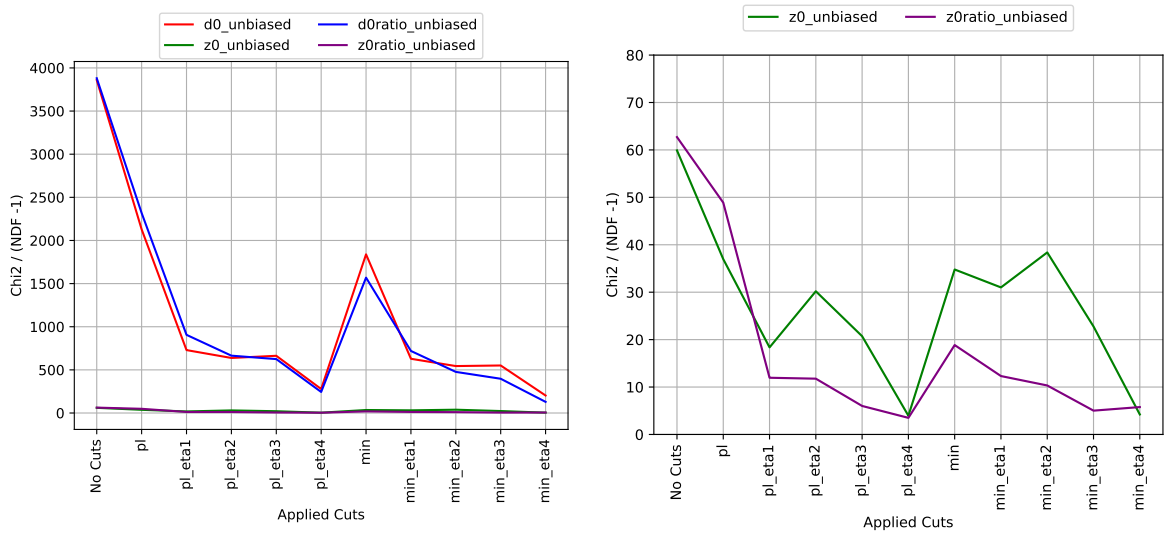

(a) χ^2/ndf for d_0,z_0, $d_0/\sigma(d_0)$ and $z_0/\sigma(z_0)$ in red, green, blue and purple, respectively.

(b) χ^2/ndf for z_0 in green and the significance of z_0 in purple.

Figure 5.5: χ^2 fit to the double ratio for the introduced observables and charge and η cuts. p_T cuts were omitted for clarity

Taking these plots into account z_0 and its significance are a much better choice in terms of the flatness of the double ratio because it can be used as a measure for how well the data was modelled by the MC. These plots demonstrate that the distribution for d_0 and its significance are not well described by the MC. Even though the d_0 has more seperating power concerning τ and μ the analysis will be carried out with z_0 because its calibration worked much better than for d_0 and the calibration of the impact parameter is at the center of this thesis. The results of this analysis will be discussed in the Sec.6.3 and whether the choice was reasonable.

To further illustrate the flat double ratio a few examples are shown for good and bad χ^2 fit performance in Fig.5.6. The first two example are chosen to demonstrate a fit to a double ratio that is very much not flat. Visible in Fig.5.6(a) and Fig.5.6(b) are the distribution of d_0 and $d_0/\sigma(d_0)$, respectively, for which the double ratio follows an inverted Gaussian distribution which has no flat region to be fitted hence a very bad performance was made. As discussed earlier the χ^2 fit performs much better for z_0 and its significance for which two examples are shown in Fig.5.6(c) and Fig.5.6(d), respectively. In both cases the lower panel shows a double ratio that is close to one and stable for the center region which is the most important region because it containts the majority of events.

5.3 Calibrated z_0 distribution

5.3.1 Calibration weights

Now that the observable which will be used in the fit is chosen one can take a closer look at its weights and their uncertainties. As seen in Fig.5.5(a) the observables z_0 and $z_0/\sigma(z_0)$ perform much better in the χ^2 fit. Thus, the double ratio is flatter and the weights applied should be smaller. But because the shape of the distribution greatly changes depending on the cuts applied the distribution of the weights might change as well.

In Fig.5.7 the calibration weights discussed in Sec.5.1 are displayed for the transverse impact parameter. On the x-axis of the plot the different cuts discussed in Sec.4.4.2 are listed and depending on the electrical charge the weight is plotted in blue or red. These weights result from averaging every weight of every bin for every distribution observable. Both lines follow the same pattern. The averaged calibration weights are small for the first η cut and reach their highest value for third η before dropping of for the last η slice. Looking at this plot the cut on the transverse momentum of the lepton has little influence on the averaged weights. The only exception seems to be the first p_T cut for which the red line exhibits the smallest peak and for the blue line the highest peak.

5.3.2 Uncertainty

In Fig.5.8 the uncertainty of the calibration is plotted for z_0 and different cuts. The red and blue represent the positive and negatice electical charge, respectively. For this plot the absolute value of the uncertainty was taken and averaged over all bins of the distribution. Just like in Fig.5.7 both lines display a similiar pattern. The averaged uncertainty reaches its highest value for the second and third η slice for every p_T cut. The lowest values are obtained for the first and the last η slice. The cut on the transverse momentum does show a certain influence. The higher the p_T cut the more the uncertainty decreases. An exception is the last p_T for which the uncertainty increases again. A reason could be that the last p_T has very few statistics. This also explains why the inclusive η cuts have little uncertainties.

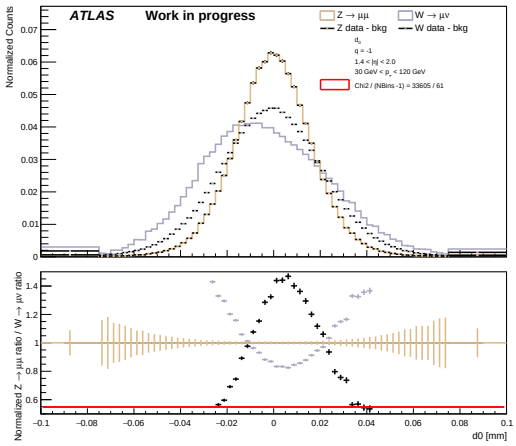

(a) Calibrated d_0 distribution for $q = -1$ and $1.4 < |\eta| < 2.0$

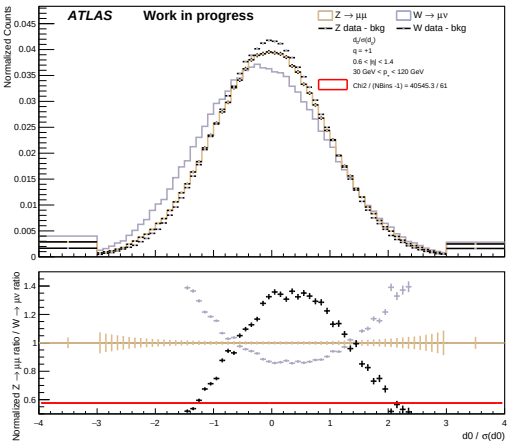

(b) Calibrated $d_0/\sigma(d_0)$ distribution for $q = +1$ and $0.6 < |\eta| < 1.4$

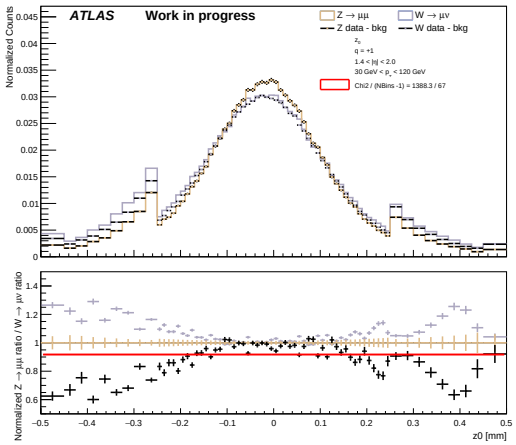

(c) Calibrated z_0 distribution for $q = +1$ and $1.4 < |\eta| < 2.0$

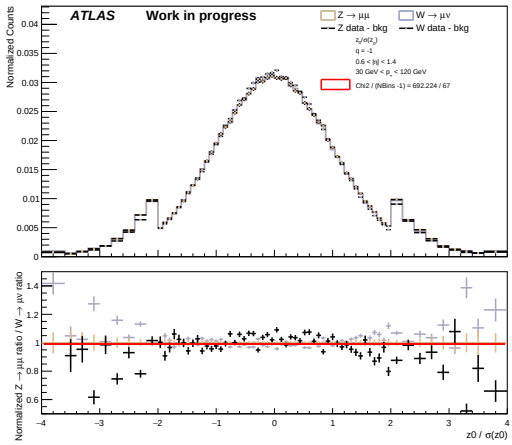

(d) Calibrated $z_0/\sigma(z_0)$ for $q = -1$ and $0.6 < |\eta| < 1.4$

Figure 5.6: Chosen examples for bad and good performance of the χ^2 fit.

5.3.3 Examples

Because the longitudinal impact parameter is chosen as the observable for the calibration this section will present two examples of the calibrated and fitted distribution of z_0 for which the fit and the double ratio does not match well and for which it does. Even though z_0 is an observable much more suitable for the fit there are a few distributions for which the double ratio is not particularly flat. Fig.5.9(a) and Fig.5.9(b) present examples for double ratios that are not flat. The double ratio in both plots is only close to one for a small region of the peak. For the tails the double ratio drops off and the ratios of the W and Z decay do not align anymore. This is due to the mismodelling of the tails for both boson decays and lack of statistics because for most distribution the double ratio is very close to one at the point of the peak. Furthermore, the central region is the most important region because most events lie in said region.

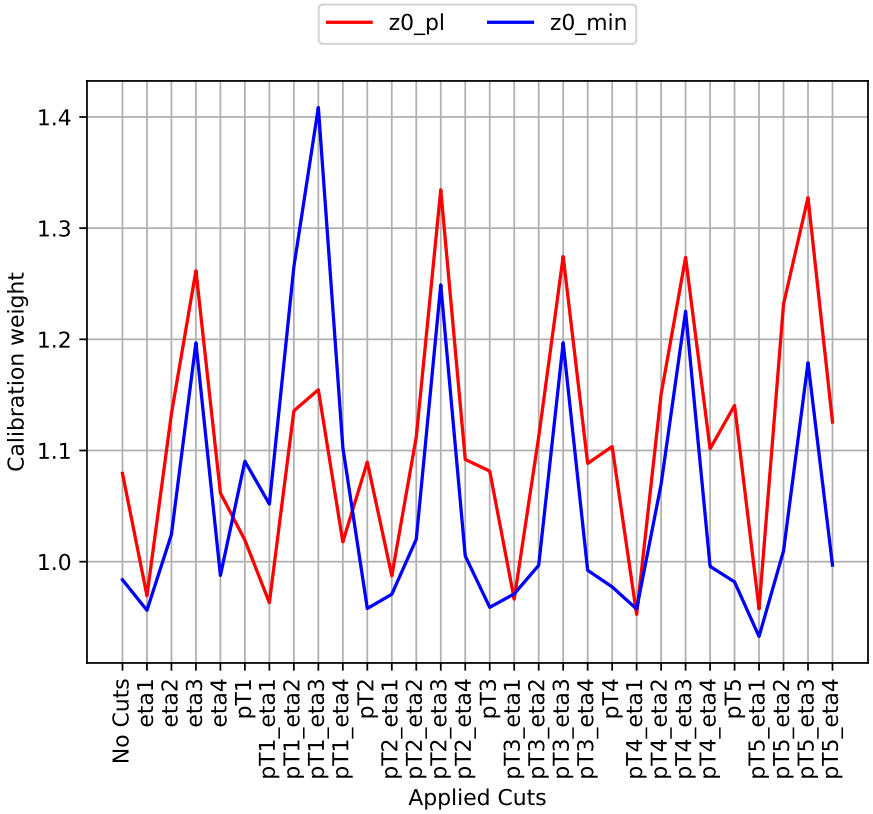

Figure 5.7: Plotted values of the calibration weight of z_0 for negative charge in blue and and positive charge in red. On the x-axis the different cuts are visible

Two examples that show a better double ratio fit are seen in Fig.5.9(c) and Fig.5.9(d). For Fig.5.9(c) the black double ratio stays close to one for the majority of the distribution and only diviates considerably on the right tail. The double ratio in Fig.5.9(d) flactuates around one for the range of the entire distribution. The binning for z_0 results in this case in tails with bins that are filled with more events than the peak. This effect is visible for distributions in the fourth η bin that covers $2.0 < |\eta| < 2.4$. The higher the η cut the higher the tail bins get because the distribution broadens for higher η. The double ratio fit for the shown example in Fig.5.6(d) is better than for the fit in Fig.5.6(c) but the points flacutate more in the center. Events in that η region are highly boosted and close to the beam line.

Because it is not possible to show in this section all the z_0 distributions that were used in the calibration of the impact parameter, they can be found in Appendix A.

5.4 Calibrated p_T distribution

As mentioned in Sec.4.2 the W-boson mass fit does depend on transverse momentum of the lepton. The weights are used to calibrate the distribution of the transverse momentum of the lepton. For the fit to work the distribution was split into different slices depending on the electrical charge, the pseudorapidity and the z_0 bin. To estimate the uncertainty of the new p_T distribution the uncertainty of the calibration weights was used.

In Fig.5.10 an example of the calibrated p_T distribution is shown is grey called nominal. The x-axis is

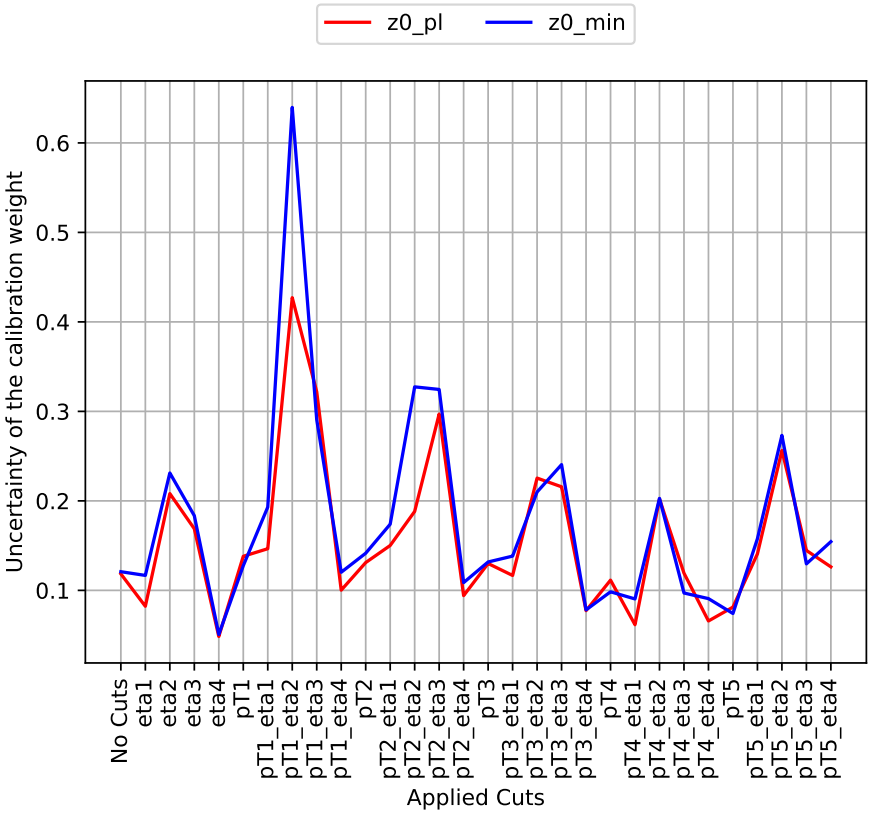

Figure 5.8: Plotted values of the calibration uncertainty of z_0 for negative charge in blue and and positive charge in red. On the x-axis the different cuts are visible

limited to 30 GeV $< p_T <$ 50 GeV because the mass fit only covers this range. The shown histogram is sliced for $q = -1$, $0 < |\eta| < 0.6$ and $-0.5\,\text{mm} < z_0 - 0.45\,\text{mm}$. The nominal distribution is a result of multiplying the calibration weight to the p_T distribution. The uncertainty of the calibration weight is used as an uncertainty envelope plotted in green and brown. As noted in the legend the green line is the upper bound of the systematic uncertainties and the brown line is the lower bound. A closer look reveals that the green line does not stay below the nominal one and the brown line does not stay above the nominal one. In fact they switch position. The reason for this is that the uncertainty in Eq.5.2 is allowed to have a positive and negative values. Thus, a change in sign flips the position of the envelopes.

The lower panel shows the ratio of the three distributions and the nominal one in their respective colours. This panel is used to give a more quantitive look at the systematic uncertainty and how it changes in the region of the distribution. The ratio of the nominal distribution and itself is of course at one. In this chapter it was explained that there is weight for every observable. Every observable can be sliced into five(four for the calibration) p_T bins. For each of these bins there is a specific weight. Thus, the distance of the envelope to the nominal distribution should change depending on the p_T region. This is clearly visible in the plot. For the first p_T bin the envelopes have a greater width than the other p_T bins.

A point that has to be mentioned is that the envelopes should be symmetrical to the nominal distribution because the value of the uncertainty is either substracted or added but this is not the case. The example in Fig.5.11 is chosen to demonstrate this. For the first p_T bin that covers 30 GeV $< p_T <$ 34 GeV on the lower panel the ratio of the envelopes is not symmetric around one. In the case of this first bin the

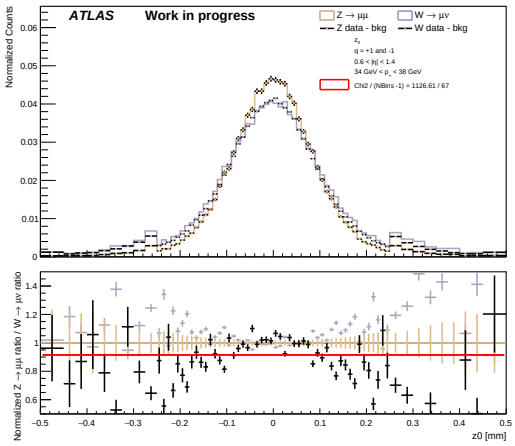

(a) $0.8 < |\eta| < 1.4$, $34\,\text{GeV} < p_T < 38\,\text{GeV}$, $q = \pm 1$

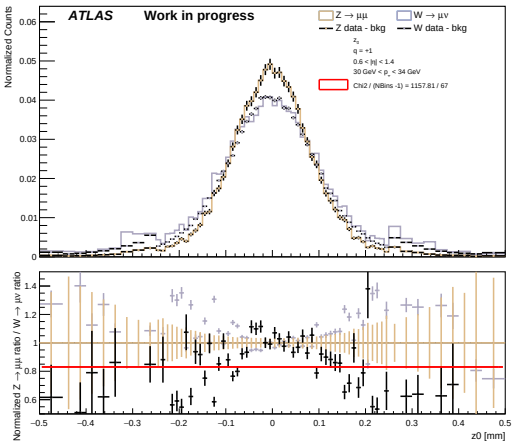

(b) $0.8 < |\eta| < 1.4$, $30\,\text{GeV} < p_T < 34\,\text{GeV}$, $q = +1$

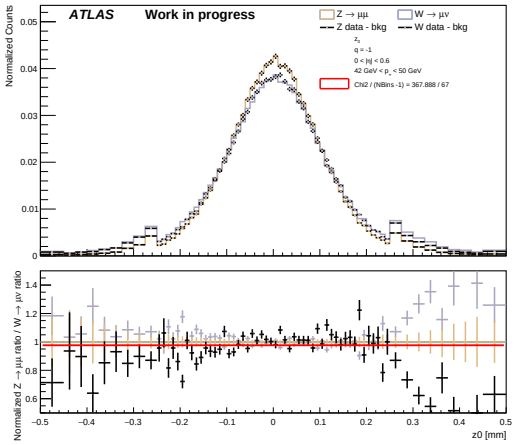

(c) $0 < |\eta| < 0.8$, $42\,\text{GeV} < p_T < 50\,\text{GeV}$, $q = -1$

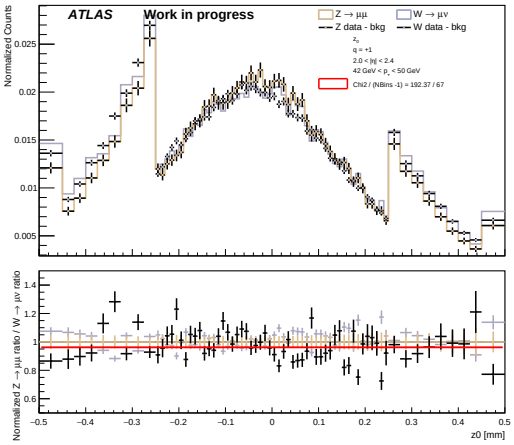

(d) $2.0 < |\eta| < 2.4$, $42\,\text{GeV} < p_T < 50\,\text{GeV}$, $q = +1$

Figure 5.9: Calibrated z_0 distributions of the W and Z decay in grey and brown, respectively, on the upper panel and the ratio of MC and data in the respective colors on the lower panel. The double ratio is plotted in black and a fit to it is shown in red.

difference is clearly visible but it looks different for every bin. For the other p_T bins the envelopes are not symmetrical either but the difference is not as big as for the first p_T bin. Another aspect is that the bins/points inside a p_T are calibrated with the same weight. This leads to the points being on the same level. The p_T bin structure is recognizable because for every p_T bin the ratio of the envelopes chages visibly. In the shown example there are small differences that are caused by different statistics in the bin.

Not all calibrated p_T distribution but a selection can be found in Appendix B because all distribution would not fit in this section or thesis.

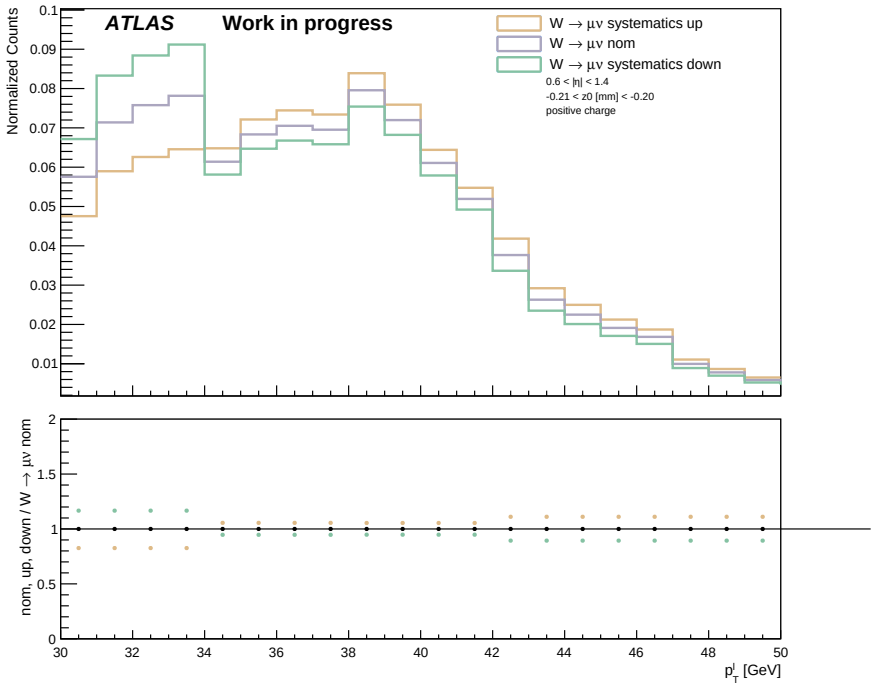

Figure 5.10: Calibrated p_T distribution for $-0.21\,\text{mm} < z_0 - 0.20\,\text{mm}$, $0.6 < |\eta| < 1.4$ and $q = +1$ on the upper panel in grey. The systematic uncertainties are plotted as an envelope in brown and green. The lower panel displays the ratio of the different distribution and the nominal one

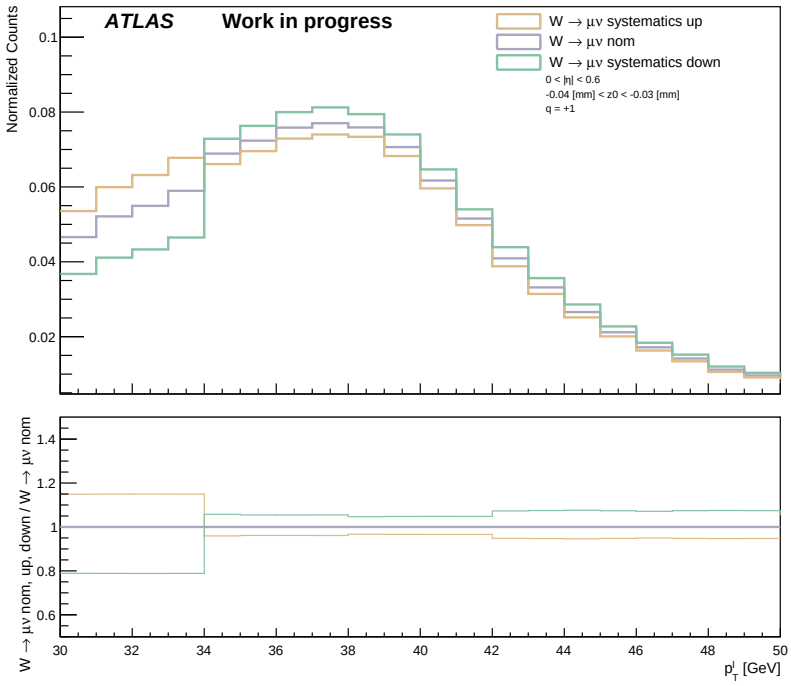

Figure 5.11: Calibrated p_T distribution for $-0.04\,\text{mm} < z_0 - 0.03\,\text{mm}$, $0 < |\eta| < 0.6$ and $q = +1$ on the upper panel in grey. The systematic uncertainties are plotted as an envelope in brown and green. The lower panel displays the ratio of the different distribution and the nominal one

CHAPTER 6

Results of the p_T fit

After the calibration of the impact parameter was established this chapter is going to present the results of the p_T fit that shows how well the calibration worked and how helpful it is.

In Sec.5.4 the p_T distribution was sliced for every z_0 bin and calibrated with the respective weight. The fit could not be done in all slices due to two reasons. The first one is that fitting many p_T slices is time consuming. Thus, time constraints limit the number of p_T distribution that will be fitted. The second reason is that the number of bins needs to be reduced in order to avoid negative and empty bin entries. Thus the 68 z_0 bins were merged into 16 bins. For the tails five bins were grouped together and for the center four. The new binning is listed in the table below.

# z_0 bins	New number of bins	Range in [mm]
1 - 10	Two Bins	- 0.5 to - 0.24
10 - 58	12 Bins	- 0.24 to 0.24
58 - 68	Two Bins	0.24 to 0.5

Table 6.1: Merged bins for the p_T fit

There will be two different fits that will be performed. The first one is the 1D fit which will be used as a comparison. The 1D fit does not include any information on the impact parameter and is only performed in the charge and η slices. The second fit is a 2D fit for which the p_T distribution is fitted in the z_0 bins according to the binnin in Tab.6.1.

6.1 Fit model

The method used to fit the pT distribution is a binned maximum likekihood fit for which each systematic is treated as a nuissance parameter. The model can be parameterized by a three factor model. The plot in Fig.6.1(a) will be used an an example. In it there are three histograms, the histogram for $W \rightarrow \tau\nu$, the histrogram for $W \rightarrow \mu\nu$ and the one for background. The sum of these histogram should match the data. In this case the distribution will be fitted to Asimov data. For the model each histogram has a normalization factor that is optimized such that the distribution fits the data. This is shown below. The likelihood fit finds the optimal value for the normalization factors

$$\mu_\mu \cdot H_\mu + \mu_\tau \cdot H_\tau + \mu_{bkg} \cdot H_{bkg} = H_{asimov} \tag{6.1}$$

$$\mu_\mu \cdot \left(H_\mu + \frac{\mu_\tau}{\mu_\mu} \cdot H_\tau + \frac{\mu_{bkg}}{\mu_\mu} \cdot H_{bkg} \right) = H_{asimov} \tag{6.2}$$

$$\mu_\mu \cdot \left(H_\mu + R_{\tau\ell} \cdot H_\tau + \frac{\mu_{bkg}}{\mu_\mu} \cdot H_{bkg} \right) = H_{asimov} \tag{6.3}$$

This formula can be rewritten by factoring out the normalization factor μ_μ thus creating a new factor $\frac{\mu_\mu}{\mu_\tau} = R_{\tau\ell}$. This is the parameter of interest because it represents how the decay of $W \to \tau\nu$ and $W \to \mu\nu$ compare to each other. To be more specific, $R_{\tau\ell}$ is proportional to the branching ratio fraction. The uncertainties on this factor will show how well the IP calibration worked.

6.2 1D fit

In the one dimensional case, the p_T distributions was fitted in four different η and two charge regions without any binning in the z_0 regions. An example of the p_T distribution for $0.0 < |\eta| < 0.8$ and $q = -1$ is shown in Fig.6.1(a). Here, the three different histogram that make up the total distribution are seen. The blue area stands for the $W \to \mu\nu$ decay, the green area for the $W \to \tau\nu$ decay and the yellow area represents the background. The shaded area represents the uncertainty. The lower panel displays the ratio of the Asimov data to the MC.

As explained above each of the three histograms has a normalization factor which is optimzed. The result of $R_{\tau\ell}$ for every fit in every region is shown in Fig.6.1(b). The red points represent the fit value. The green and black error bars stand for the statistical and total uncertainty, respectively. Their values are listed on the right side. On the bottom the combined value and uncertainties are shown and can be found in Tab.6.2. The fitted value is one because the distribution is fitted to Asimov data. The full uncertainty is dominated by the statistical uncertainty.

	Central Value	Full Uncertainty	Statistical Uncertainty
1D	1.0	5.7503 %	4.7302 %

Table 6.2: Results of the 1D fit for $R_{\tau\ell}$

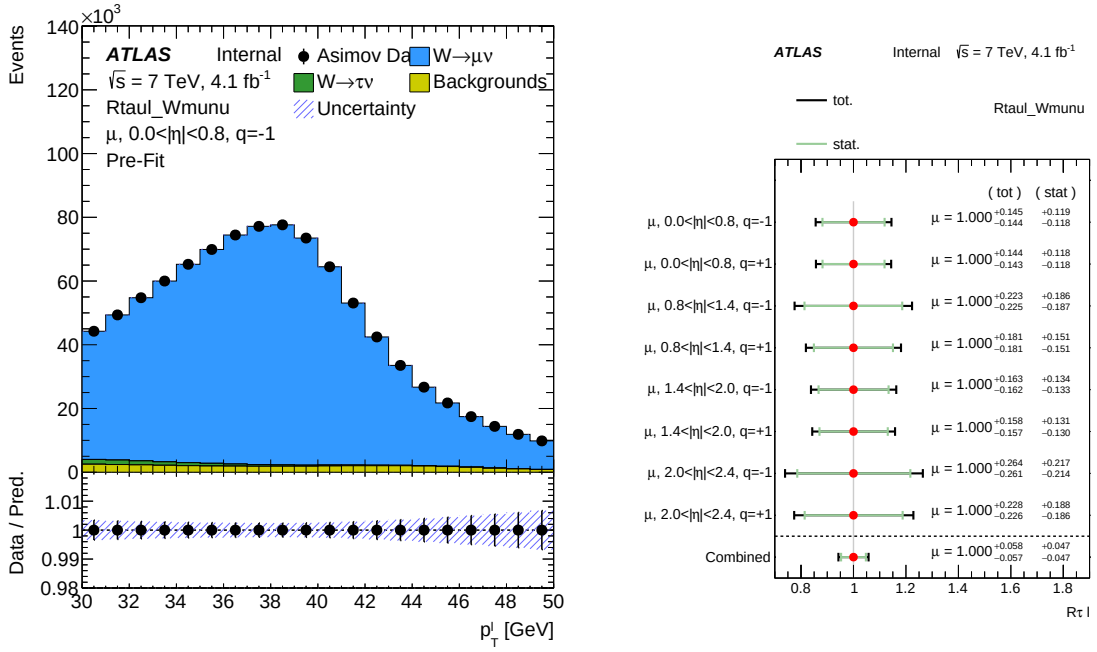

(a) $0 < |\eta| < 0.8$, $q = -1$. Blue, green and yellow area represent $W \to \mu\nu$, $W \to \tau\nu$ and the background, respectively. The shaded area shows the uncertainty. The lower panel shows ratio data and MC.

(b) 1D-fit result for different η and charge regions including statistical and total uncertainty. The combined result

Figure 6.1: The left plot shows the fit of the p_T distribution. The right plot shows the result of the 1D fit for different η and charge regions.

6.3 2D fit

This section presents the result of the 2D fit meaning the p_T distribution are sliced additional to the electrical charge, and pseudorapidity in bins of the impact parameter z_0. First, two fitted p_T distributions are going to be shown and then the result of the fit including and excluding IP systematics is going to be discussed.

6.3.1 p_T-distribution fit

The Fig.6.2 shows two examples of the p_T distribution for the 2D fit. The difference between these two and the one example for the 1D fit is that the p_T distributions were sliced in z_0 as well. Both plots show different regions of z_0. Fig.6.2(a) is sliced for the central region: $0.04\,\text{mm} < z_0 < 0.08\,\text{mm}$ while the Fig.6.2(b) is sliced for the tail: $-0.35\,\text{mm} < z_0 < 0.24\,\text{mm}$. In both cases the distribution has a different shape compared to the 1D fit. What is noticeable is that the p_T binning explained in Sec.4.4.2 is visible. The first p_T bin coveres $30\,\text{GeV} < p_T < 50\,\text{GeV}$. This bin structure is visible in both plots because the shape has a kink at the exact same position. In Fig.6.2(b) even the second p_T which covers 34 GeV to 38 GeV is visible.

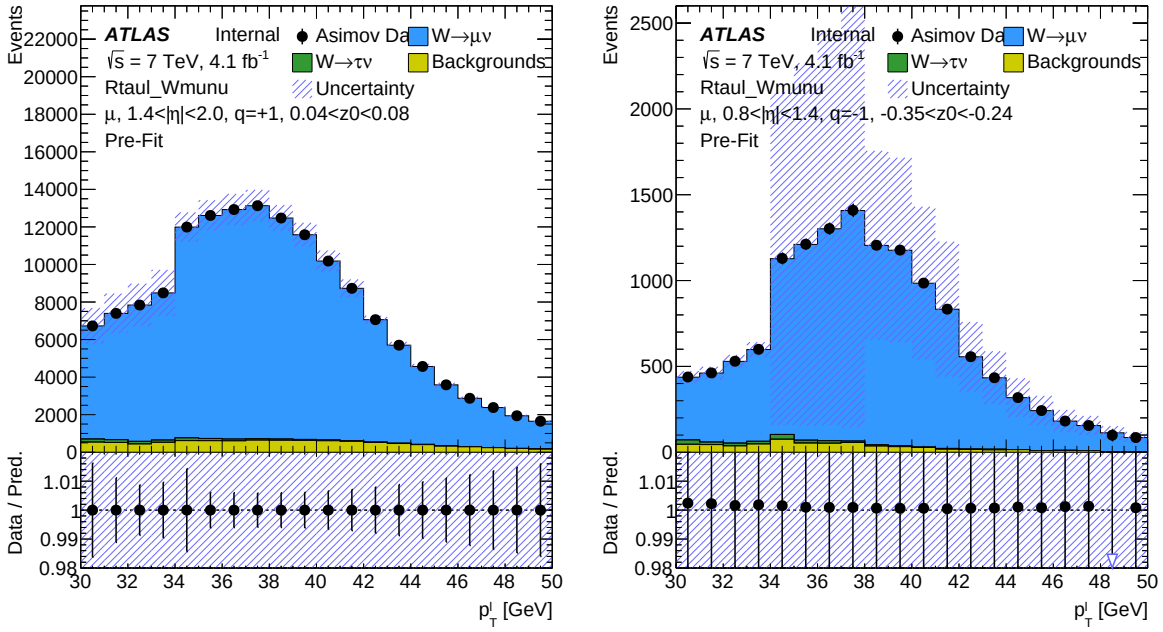

(a) 0.04 mm $< z_0 <$ 0.08 mm, $1.4 < |\eta| < 2.0$, $q = +1$ (b) -0.35 mm $< z_0 <$ 0.24 mm, $0.8 < |\eta| < 1.4$,$q = -1$

Figure 6.2: Two examples that show kinks in the shape of the p_T fit. Upper panel shows the different distributions. Lower panel shows the ratio of data and MC

6.3.2 Fit uncertainties

The Fig.6.3 presents the results of the p_T fit for $R_{\tau\ell}$. The left side includes IP uncertainties and the right side does not. It can be seen that the fitted value for $\mu_\tau/\mu_\tau\mu$ is 1 for most slices. An exception is the value for the fourth η and $q = +1$ slice for which a pull is visible. This is the case for both plots. This can be explained by the few multijet background events that are the bins. This leads to the combined fit not being at 1.0.

The Tab.6.3 summarizes the central value of the fit and the different uncertainties for the 1D and 2D case. In the case of the 2D fit the statistical uncertainty slightly reduces. This was noticed in the bachelor analysis done by Hannah Schmitz as well. The opposite is seen for the full uncertainty which increases when including the systematic uncertainties of the 2D fit. By adding the uncertainty for the impact parameter the full uncertainty increases slightly. This means that the influence of the established uncertainty for the longitudinal impact parameter z_0 is very small.

	Central Value	Full Uncertainty	Statistical Uncertainty
1D	1.0	5.7503 %	4.7302 %
2D w/o Sys	0.9937	5.9946 %	4.4857 %
2D w/ Sys	0.9937	5.9954 %	4.4857 %

Table 6.3: Results of the 1D fit in comparison to 2D fit for $R_{\tau\ell}$ with IP systematics and without. For both cases the central value, the full uncertainty and the statistical one are given

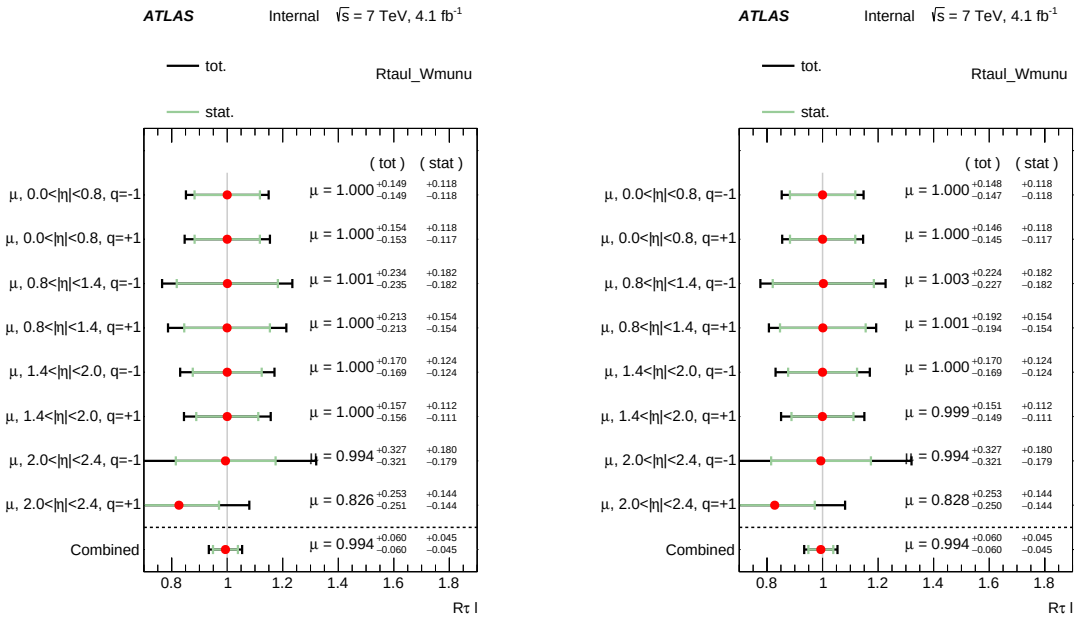

(a) With IP systematics: 0.9937 ± 5.9954(4.4857) (b) Without IP systematics: 0.9937 ± 5.9946(4.4857)

Figure 6.3: 2D-fit result of $R_{\tau\ell}$ for different η and charge slices. On the right side of each plot the total and statistical uncertainty for each slice. The combined result is shown at the bottom.

6.4 New Calibration

Because the results of the 2D fit did not show a considerable improvement the idea was to redo the calibration for different cuts. Because binning the p_T led to unwanted kinks in the shape of the p_T distribution. For this reason the new observables for the new calibration will *p-quant* and the number of hits in the B-layer(see Sec.3.2.3). Additionally, the calibration will be done for d_0, z_0 and the significance of z_0. Due to time constraints a thorough analysis of the double ratio and the calibration weights could not be made but the plots of the double ratio fit for the new calibration can be found in Appendix.D. The new calibration follows the same steps as described in Sec.5.1.
Another difference is that a new binning was applied for z_0 and $z_0/\sigma(z_0)$ which is shown below:

$\lvert z_0\rvert$ range [mm]	Bin width [mm]	$\lvert z_0/\sigma(z_0)\rvert$ range [mm]	Bin width [mm]
0 - 0.25	25 bins with 0.01	0 - 2.0	25 bins with 0.08
0.25 - 0.5	5 bins with 0.5	2.0 - 4.0	5 bins with 0.4

Table 6.4: Binning for the new calibration of the z_0 and $z_0/\sigma(z_0)$ distribution

The two new cuts are binned as well. For the number of B-layer hits(nBL) there are three bins. The observable p_{quant} has four bins. The binning for both is listed in Tab.6.5.

Number of B-layer hits(nBL)	p-quant [1/GeV]
0	0 - 0.03
1	0.03 - 0.04
≥2	0.04 - 0.05
	0.05 - 0.1

Table 6.5: Binning for nBL and p-quant that was used for the new calibration

6.4.1 p_T-distribution fit

Again, the weights were used to calibrate the events in the p_T distribution. This time there are no kinks in the shape as seen in the example pictured below in Fig.6.4. This fit of the p_T distribution is based on 14 merged bins. Like in the previous calibration the number of impact parameter bins needed to be reduced such that the fit could converge. Only one example of the fitted p_T distribution but a greater selecton can be found in Appendix.E. Not all distributions can be shown because this would be beyond the scope of the appendix.

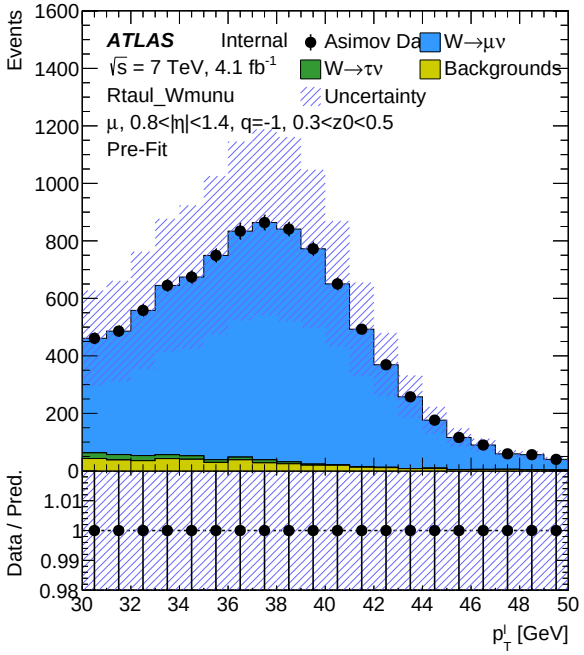

Figure 6.4: p_T distribution for $0.8 < |\eta| < 1.4$, $q = -1$ and $0.3\,\text{mm} < z_0 < 0.5\,\text{mm}$ for a fit with 14 z_0 bins. This distribution does not show any kinks in the shape

Fig.6.5 shows two examples of the systematic envelope of the p_T distribution. The red and blue line represent in both cases $1\,\sigma$ uncertainty. On the lower panel the procentual difference compared to the nominal distribution is seen. In the case of z_0 both lines are symmetrical. In the case of d_0 the $1\,\sigma$ uncertainty is extremely high at almost 500 % and thus the $-1\,\sigma$ envelope can not be seen because the blue line is at zero.

The great uncertainties for the calibration with d_0 can be explained by the way the calibration uncertainty was defined in Sec.5.1. It was shown that the double ratio for d_0 was not flat. In fact, it has a Gaussian shape.(compare Fig.5.3(b)). Thus, the uncertainty on the calibration weights have large values,

especially for the tails. The double ratio of the z_0 distribution is flatter which means the uncertainty concerning the IP calibration leads to an uncertainty envelope which is narrower.

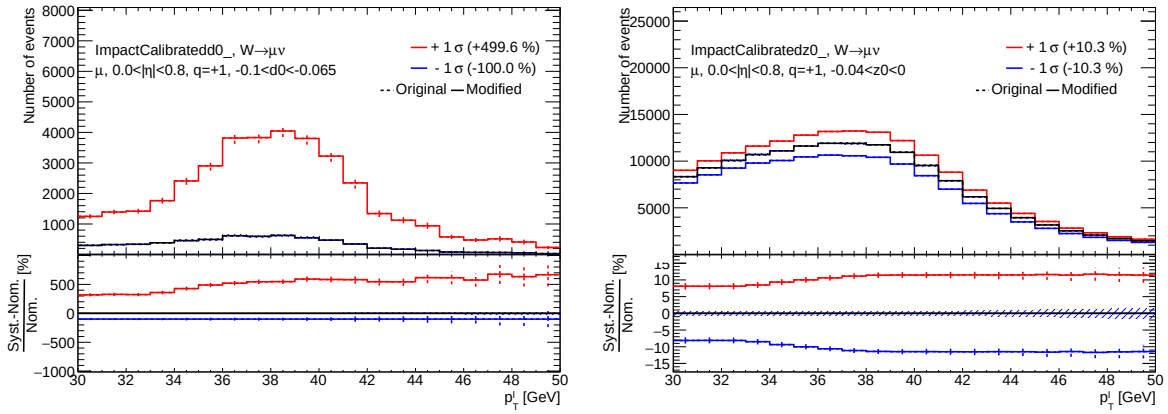

(a) $0 < |\eta| < 0.8$, $-0.1\,\text{mm} < d_0 < -0.065\,\text{mm}$, $q = +1$ (b) $0 < |\eta| < 0.8$, $-0.04\,\text{mm} < z_0 < 0\,\text{mm}$, $q = +1$

Figure 6.5: Envelopes of the systematic uncertainties of the p_T distribution. The red and blue lines represent $\pm 1\,\sigma$ uncertainty. On the lower panel the procentual difference of the envelope compared to the nominal distribution in black

For the new calibration the fit was performed for three different binnings. The fit was performed in 14, 8 and 4 bins for each impact parameter observable. The range of these fits are listed in the Tab.6.6. Because the binning is symmetric only half of the bin range is shown.

Observable	Bin Number						
	1				2		
	1		2		3		4
	1	2	3	4	5	6	7
d0 [mm]	0- 0.01	0.01 - 0.02	0.02 - 0.03	0.03 - 0.04	0.04 - 0.05	0.05 - 0.065	0.065 - 0.1
z0 [mm]	0 - 0.04	0.04 - 0.08	0.08 - 0.12	0.12 - 0.16	0.16 - 0.2	0.2 - 0.3	0.3 - 0.5
z0ratio [mm]	0 - 0.32	0.32 - 0.64	0.64 - 0.96	0.96 - 1.28	1.28 - 1.6	1.6 - 2.4	2.4 - 4

Table 6.6: Bin range of d_0, z_0 and $z_0/\sigma(z_0)$ for different binning. Because it is symmetrical only the positive half is shown

6.4.2 Fit uncertainties

The result of the fit for the different observables and binnings are listed in Tab.6.7. The fitted value of $R_{\tau\ell}$ is 1.0 for all cases. It the table three different uncertainties are shown. *Statistics only* includes only the statistical uncertainty, *w/o Sys* includes the statistical and systematic uncertainty except for the IP uncertainty, and *w/ Sys* is the full uncertainty. Two trends are noticable. The first one is about the statistical uncertainty. The smallest statistical uncertainty is the one fit done with d_0 and the biggest for z_0. Independent of the observable, the statistical uncertainty increases the fewer bins are used for the fit. But the increase is only very small for each step except for the uncertainty of d_0 when going from 8 to 4 bins. The second trend concerns the systematic uncertainty. Again, the uncertainty increases if the fit is performed with fewer bins in both cases of including the IP systematics and excluding them. Similiar to the statistical case the uncertainty only slightly increases. An exception is again the fit of d_0 in 4 bins for

which the uncertainty rises by more than one percent. Additionally, the inclusion of IP systematics only slightly increases the uncertainty

Bins	z0		d0		z0ratio	
	w/ Sys	w/o Sys	w/ Sys	w/o Sys	w/ Sys	w/o Sys
	Statistics only		Statistics only		Statistics only	
14	6.1147 %	6.0805 %	4.3480 %	4.3081 %	6.0443 %	5.8929 %
	4.5096 %		3.0277 %		4.2089 %	
8	6.2968 %	6.2566 %	4.4803 %	4.4646 %	6.2751 %	6.1037 %
	4.5341 %		3.0752 %		4.2388 %	
4	6.5236 %	6.4929 %	5.6111 %	5.6040 %	6.7601 %	6.5227 %
	4.5747 %		3.5322 %		4.3620 %	

Table 6.7: Uncertainty of fitted $R_{\tau\ell} = 1$ for new calibration with d_0,z_0 and $z_0/\sigma(z_0)$, and 14, 8 and 4 bins. *w/Sys* shows full uncertainty, *w/o Sys* shows full uncertainty except for IP systematics, *Statistics only* includes only the statistical uncertainty. The fit values and its uncertainties for every observable, binning and slice are taking from Appendix.C.

These results have to compared to the 1D fit and how they differ. Taken from Tab.6.2 the full uncertainty is 5.7503 % and the statistical uncertainty is 4.7302 %. Compared to the 2D fit one can see that the full uncertainty for z_0 and $z_0/\sigma(z_0)$ is greater than for the 1D fit for every binning. The statistical uncertainty decreased slightly which was also seen for the old calibration. Taking a look at the uncertainty of the d_0 fit the full and statistical uncertainty are smaller than for the 1D fit, no matter the binning.
An explanation for why the d_0 performed better even though the calibration worked better for z_0 and $z_0/\sigma(z_0)$ is that the the transverse impact parameter is more useful in seperating $W \to \tau\mu$ and $W \to \mu\nu$ as seen in Fig.4.4 and that the parameter of interest is a ratio which leads to the cancellation of the great uncertainties that were shown in Fig.6.5.

CHAPTER 7

Summary and Outlook

This thesis investigated the influence of the impact parameter in the measurement of the $W \to \mu\nu$ decay of Run 1 at $\sqrt{s} = 7\,\text{TeV}, \sigma = 4.1\,\text{fb}^{-1}$ recorded at the ATLAS detector located at CERN in Geneve. Furthermore, this thesis is part of a reanalysis of the W-boson mass and its precise measurement can put constraints on theories that involve physics beyond the SM. According to lepton universality the branching ratio fraction of $W \to \tau\nu / W \to \mu\nu$ should not deviate from one because apart from the mass there is no difference between the different lepton generations.

The final state $\mu\nu$ can be achieved by both processes. Either the W-boson decays directly to a muon or it originates from the $\tau \to \mu\nu$ decay. In order to differentiate these two decays this thesis looked at the distribution of the impact parameter.

The idea of this analysis was to use the similiar decay $Z \to \mu\mu$ as a calibration because it is has one more track pointing towards the vertex thus giving a better description.

The first step of calibrating the impact parameter is calculating a weight that equalizes the data and MC of the $Z \to \mu\mu$ decay for every bin of the distribution. These weights are used to calibrate the same bins of the distribution of the $W \to \mu\nu$ decay. This is done for d_0,z_0, $d_0/\sigma(d_0)$ and $z_0/\sigma(z_0)$. A flat double ratio determines what observable is more suitable because it means that the data is modeled the same way for the W and Z decay. The performance of a χ^2 fit to the double ratio determined which observable will be used for further analysis. z_0 was chosen for the p_T calibration and fit because the calibration worked much better than for d_0. The weight were used to calibrate and give systematic uncertainties for an in z_0 binned p_T distribution. It is then fitted by a binned maximum likelihood method than can be parametrized by a three factor model. One of the factors is $R_{\tau\ell}$ and is proportional to the branching ratio fraction.

For the 1D fit no information of IP is included. This value is used as reference for the 2D fit. The statistical and the full uncertainty are 4.73 % and 5.75 %, respectively. In the 2D case the p_T distribution was fitted in 16 merged z_0 bins. This time the full uncertainty will include the IP systematics. Compared to the 1D fit the statistical uncertainty decreases from 4.73 % to 4.49 %. This was already shown in a bachelor thesis by Hannah Schmitz. If the IP systematics are not included the full uncertainty is 5.9946 % and if they are included it is 5.9954 %. In the case of the old calibration the inclusion of the IP systematics had little impact. Further, the distribution of the p_T fit showed kinks in the shape that mirrored the binning of the p_T cut.

For the new calibration two new cuts were chosen and the calibration was redone for d_0,z_0, $z_0/\sigma(z_0)$ and two cuts: *p-quant* and nBL. Due to time constraints the analysis could not be made in detail. For the new calibration the fit was performed in 14, 8 and 4 bins. Otherwise, the calibration and fit were done in the same way. Again, the result can be compared to the 1D fit. Independent of the binning or observable the statistical uncertainty decreases slightly which is in line with the old calibration. The trend

that was noticed is that the more merged bins there are the smaller the uncertainty gets. The statistical uncertainty for z_0 anf $z_0/\sigma(z_0)$ are close to each other at 4.51 % and 4.21 %, respectively. For d_0 the statistical uncertainty is 3.02 %. Similiar to the old calibration, the inclusion of the IP systematics had little impact and the full uncertainty is smaller for d_0 than for z_0, its significance and the 1D fit. The reason why the transversal impact parameter gives smaller uncertainties despite the high systematics is because the parameter of interest is a ratio thus the uncertainties cancel out. Furthermore, as mentioned before d_0 is more suitable in seperating the $W \to \mu\nu$ and $W \to \tau\nu$ decay that is why d_0 has the smallest uncertainties. An explanation for why the systematics of the IP have little to no impact is that the tails which are the sensitive regions show only little MC statistics. As of now the inclusion of the impact parameter is not helpful because the vertexing for Run 1 is not precise enough.

A way to further examine the IP would be to establish an uncertainty on the uncertainty because the way the calibration uncertainty was defined it does not consider how precise this method is. An improvement would be to take into account a statitistical uncertainty on the MC. Another idea is changing the parametrization of the vertex uncertainty but this is not possible for the Run 1.

Acknowledgements

I would like to thank Prof. Klaus Desch for giving me the oppurtunity to write my master thesis in his research group. I also like to thank PD Philip Bechtle and Philipp König for their supervision, especially during these challenging times.

Bibliography

[1] C. Burgard, *Example: Standard model of physics*, https://texample.net/tikz/examples/model-physics/ (cit. on p. 3).

[2] B. Povh et al., *Teilchen und Kerne. Eine Einfuehrung in die physikalischen Konzepte*, Sixth, Springer-Verlag GmbH, 2004, ISBN: 3540210652 (cit. on p. 3).

[3] G. Aad et al., *Observation of a new particle in the search for the Standard Model Higgs boson with the ATLAS detector at the LHC*, Physics Letters B **716** (2012) 1, ISSN: 0370-2693, URL: http://dx.doi.org/10.1016/j.physletb.2012.08.020 (cit. on p. 4).

[4] S. Glashow, *Partial Symmetries of Weak Interactions*, Nucl. Phys. **22** (1961) 579 (cit. on p. 4).

[5] A. Djouadi, *The anatomy of electroweak symmetry breaking: Tome I: The Higgs boson in the Standard Model*, Physics Reports **457** (2008) 1, ISSN: 0370-1573, URL: http://www.sciencedirect.com/science/article/pii/S0370157307004334 (cit. on p. 5).

[6] S. Dawson, "Introduction to electroweak symmetry breaking", *ICTP Summer School in High-Energy Physics and Cosmology*, 1998 1, arXiv: hep-ph/9901280 (cit. on p. 5).

[7] M. E. Peskin and D. V. Schroeder, *An introduction to quantum field theory*, Includes exercises, Westview, 1995, URL: https://cds.cern.ch/record/257493 (cit. on p. 5).

[8] M. L. Perl, *The Discovery of The Tau Lepton*, NATO Sci. Ser. B **352** (1996) 277, ed. by H. B. Newman and T. Ypsilantis (cit. on p. 6).

[9] S. Gentile and M. Pohl, *Physics of tau leptons*, Physics Reports **274** (1996) 287, ISSN: 0370-1573, URL: http://www.sciencedirect.com/science/article/pii/0370157396000026 (cit. on p. 6).

[10] P.A. Zyla et al. (Particle Data Group), Prog. Theor. Exp. Phys. 2020, 083C01 (2020) (cit. on pp. 7, 8).

[11] L. Di Lella and C. Rubbia, *The Discovery of the W and Z Particles*, Adv. Ser. Direct. High Energy Phys. **23** (2015) 137 (cit. on p. 7).

[12] A. Pich, *The Standard Model of Electroweak Interactions*, 2007, arXiv: 0705.4264 [hep-ph] (cit. on p. 8).

[13] P. Sauerland, *Kinematic reconstruction of tau leptons and test for lepton universality in charged weak interactions with the CMS experiment*, Zsfassung in dt. und engl. Sprache; Aachen, Techn. Hochsch., Diss., 2011, PhD thesis, 2011 XIII, 122 S. : graph. Darst. URL: https://publications.rwth-aachen.de/record/64350 (cit. on p. 9).

[14] M. Böhm, A. Denner and H. Joos, *Gauge theories of strong and electroweak interactions; 3rd ed.* Trans. of 3rd ed.: Eichtheorien der starken und elektroschwachen Wechselwirkung. Stuttgart, Teubner, 2001, B. G. Teubner, 2001, URL: https://cds.cern.ch/record/1333727 (cit. on p. 9).

[15] J.-h. Park, *Lepton non-universality at LEP and charged Higgs*, Journal of High Energy Physics **2006** (2006) 077, ISSN: 1029-8479, URL: http://dx.doi.org/10.1088/1126-6708/2006/10/077 (cit. on p. 9).

[16] R. Aaij et al., *Measurement of the Ratio of Branching FractionsB(B́0D*+ŕ)/B(B́0D*+ŕ)*, Physical Review Letters **115** (2015), ISSN: 1079-7114, URL: http://dx.doi.org/10.1103/PhysRevLett.115.111803 (cit. on p. 9).

[17] A. Collaboration, *Test of the universality of τ and μ lepton couplings in W-boson decays from $t\bar{t}$ events with the ATLAS detector*, 2020, arXiv: 2007.14040 [hep-ex] (cit. on p. 9).

[18] K. Freese, *Review of Observational Evidence for Dark Matter in the Universe and in upcoming searches for Dark Stars*, EAS Publications Series **36** (2009) 113, ISSN: 1638-1963, URL: http://dx.doi.org/10.1051/eas/0936016 (cit. on p. 10).

[19] J. Erler and M. Schott, *Electroweak precision tests of the Standard Model after the discovery of the Higgs boson*, Progress in Particle and Nuclear Physics **106** (2019) 68, ISSN: 0146-6410, URL: http://dx.doi.org/10.1016/j.ppnp.2019.02.007 (cit. on pp. 12, 29).

[20] G. Pásztor, *Recent ATLAS results and preparations for Run 2*, 2016, arXiv: 1602.01536 [hep-ex] (cit. on p. 14).

[21] L. R. F. Castillo, "The ATLAS and CMS detectors", *The Search and Discovery of the Higgs Boson*, 2053-2571, Morgan and Claypool Publishers, 2015 4, ISBN: 978-1-6817-4078-2, URL: http://dx.doi.org/10.1088/978-1-6817-4078-2ch4 (cit. on p. 14).

[22] G. Perez, *Unitarization Models For Vector Boson Scattering at the LHC*, PhD thesis, 2018 (cit. on p. 15).

[23] A. Airapetian et al., *ATLAS detector and physics performance: Technical Design Report, 1*, Technical Design Report ATLAS, CERN, 1999, URL: https://cds.cern.ch/record/391176 (cit. on p. 15).

[24] E.Daw, *Lecture 7 - Rapidity and Pseudorapidity*, 2012, URL: http://www.hep.shef.ac.uk/edaw/PHY206/Site/2012_course_files/phy206rlec7.pdf (cit. on p. 15).

[25] U. Zürich, *How to draw diagrams in LaTeX with TikZ*, 2020, URL: https://wiki.physik.uzh.ch/cms/latex:tikz (cit. on p. 16).

[26] V. A. MITSOU, *THE ATLAS TRANSITION RADIATION TRACKER*, Astroparticle, Particle and Space Physics, Detectors and Medical Physics Applications (2004), URL: http://dx.doi.org/10.1142/9789812702708_0073 (cit. on p. 16).

[27] A. L. Rosa, *ATLAS Pixel Detector: Operational Experience and Run-1 to Run-2 Transition*, 2015, arXiv: 1410.6347 [physics.ins-det] (cit. on p. 16).

[28] B. Di Girolamo, *The ATLAS Pixel Detector*, tech. rep. ATL-INDET-PROC-2011-016, CERN, 2011, URL: http://cds.cern.ch/record/1385028 (cit. on p. 16).

[29] T. A. collaboration, *Operation and performance of the ATLAS semiconductor tracker*, Journal of Instrumentation **9** (2014) P08009, ISSN: 1748-0221, URL: http://dx.doi.org/10.1088/1748-0221/9/08/P08009 (cit. on p. 16).

[30] N. Barlow, *Operation of the ATLAS Semiconductor Tracker*, tech. rep. ATL-INDET-PROC-2010-003, CERN, 2010, URL: https://cds.cern.ch/record/1237401 (cit. on p. 16).

[31] A. Vogel, *ATLAS Transition Radiation Tracker (TRT): Straw Tube Gaseous Detectors at High Rates*, tech. rep. ATL-INDET-PROC-2013-005, CERN, 2013, URL: https://cds.cern.ch/record/1537991 (cit. on p. 17).

[32] E. Abat, T. N. Addy and T. P. A. Akesson, *The ATLAS Transition Radiation Tracker (TRT) proportional drift tube: design and performance*, JINST **3** (2008) P02013, URL: http://cds.cern.ch/record/1094549 (cit. on p. 17).

[33] F. Teischinger, *Energy Measurement with the ATLAS Electromagnetic Calorimeter at the Per Mill Accuracy Level*, Presented 19 Mar 2014, 2014, URL: https://cds.cern.ch/record/1699838 (cit. on p. 17).

[34] M. Aleksa and M. Diemoz, *Discussion on the electromagnetic calorimeters of ATLAS and CMS*, tech. rep. ATL-LARG-PROC-2013-002, CERN, 2013, URL: https://cds.cern.ch/record/1547314 (cit. on p. 17).

[35] T. A. Collaboration and G. Aad, *The ATLAS Experiment at the CERN Large Hadron Collider*, Journal of Instrumentation **3** (2008) S08003, URL: https://doi.org/10.1088%2F1748-0221%2F3%2F08%2Fs08003 (cit. on pp. 17, 19).

[36] A. M. Henriques Correia, *The ATLAS Tile Calorimeter*, tech. rep. ATL-TILECAL-PROC-2015-002, CERN, 2015, URL: https://cds.cern.ch/record/2004868 (cit. on p. 18).

[37] K. Ishii, *The ATLAS muon spectrometer*, PoS **HEP2001** (2001) 253, ed. by D. Horváth, P. Lévai and A. Patkós (cit. on p. 18).

[38] J. S. and, *The ATLAS High Level Trigger Configuration and Steering: Experience with the First 7 TeV Collision Data*, Journal of Physics: Conference Series **331** (2011) 022026, URL: https://doi.org/10.1088%2F1742-6596%2F331%2F2%2F022026 (cit. on p. 19).

[39] A. collaboration, *ATLAS Experiment, Public Result Luminosity*, URL: https://twiki.cern.ch/twiki/bin/view/AtlasPublic/LuminosityPublicResults (cit. on p. 19).

[40] Mathias Uhlenbrock, *Studies into the mis-identification probability of tau leptons and a measurement of the cross section (pp W) Œ BR(W) at a center-of-mass energy of s = 7 TeV with the ATLAS detector*, PhD thesis: Rheinische Friedrich-Wilhelms-Universität Bonn, 2016, URL: http://hdl.handle.net/20.500.11811/6723 (cit. on p. 20).

[41] M. Cacciari, G. P. Salam and G. Soyez, *The anti-ktjet clustering algorithm*, Journal of High Energy Physics **2008** (2008) 063, ISSN: 1029-8479, URL: http://dx.doi.org/10.1088/1126-6708/2008/04/063 (cit. on p. 20).

[42] G. Aad et al., *Jet energy measurement and its systematic uncertainty in protonproton collisions at $\sqrt{s}$ = 7 TeV with the ATLAS detector*, The European Physical Journal C **75** (2015), ISSN: 1434-6052, URL: http://dx.doi.org/10.1140/epjc/s10052-014-3190-y (cit. on p. 21).

[43] *Identification of the Hadronic Decays of Tau Leptons in 2012 Data with the ATLAS Detector*, tech. rep. ATLAS-CONF-2013-064, CERN, 2013, URL: https://cds.cern.ch/record/1562839 (cit. on p. 22).

[44] G. Aad et al., *Muon reconstruction efficiency and momentum resolution of the ATLAS experiment in protonproton collisions at $\sqrt{s}$ = 7 TeV in 2010*, The European Physical Journal C **74** (2014), ISSN: 1434-6052, URL: http://dx.doi.org/10.1140/epjc/s10052-014-3034-9 (cit. on p. 22).

[45] L. March, *Performance of missing transverse momentum reconstruction in ATLAS studied in proton-proton collisions in 2012 at 8 TeV*, Journal of Physics: Conference Series **645** (2015) 012014, URL: https://doi.org/10.1088%2F1742-6596%2F645%2F1%2F012014 (cit. on p. 23).

[46] A. Buckley et al., *General-purpose event generators for LHC physics*, Physics Reports **504** (2011) 145, ISSN: 0370-1573, URL: http://dx.doi.org/10.1016/j.physrep.2011.03.005 (cit. on p. 23).

[47] S. Agostinelli et al., *GEANT4–a simulation toolkit*, Nucl. Instrum. Meth. A **506** (2003) 250 (cit. on p. 24).

[48] W. Panduro Vazquez, *The ATLAS Data Acquisition System: from Run 1 to Run 2*, Nucl. Part. Phys. Proc. **273-275** (2016) 939, ed. by M. Aguilar-Bentez et al. (cit. on p. 24).

[49] M. Aaboud et al., *Reconstruction of primary vertices at the ATLAS experiment in Run 1 protonproton collisions at the LHC*, The European Physical Journal C **77** (2017), ISSN: 1434-6052, URL: http://dx.doi.org/10.1140/epjc/s10052-017-4887-5 (cit. on p. 24).

[50] *Performance of primary vertex reconstruction in proton-proton collisions at $\sqrt{s}$ =7 TeV in the ATLAS experiment*, tech. rep. ATLAS-CONF-2010-069, CERN, 2010, URL: https://cds.cern.ch/record/1281344 (cit. on p. 24).

[51] A. collaboration, *ATLAS Experiment, Public Result Tracking Performance*, URL: https://twiki.cern.ch/twiki/bin/view/AtlasPublic/InDetTrackingPerformanceApprovedPlots (cit. on p. 25).

[52] C. Li, *B-tagging in ATLAS Experiment*, URL: https://indico.in2p3.fr/event/13330/contributions/13775/attachments/11586/14280/Changqiao%5C_TPJRJC.pdf (cit. on p. 26).

[53] S. Pires, *Impact of the Insertable B-layer on b-tagging Performance for ATLAS Run-II*, Acta Phys. Polon. B **45** (2014) 1567 (cit. on p. 27).

[54] N. Benekos et al., *ATLAS Inner Detector Performance*, (2003) (cit. on pp. 26, 28).

[55] M. Aaboud et al., *Measurement of the W-boson mass in pp collisions at $\sqrt{s}$ = 7 TeV with the ATLAS detector*, Eur. Phys. J. C **78** (2018) 110, [Erratum: Eur.Phys.J.C 78, 898 (2018)], arXiv: 1701.07240 [hep-ex] (cit. on pp. 29, 31).

[56] N. Andari et al., *Measurement of m_W with 7 TeV data: W boson mass measurement*, tech. rep. ATL-COM-PHYS-2014-1569, CERN, 2014, URL: https://cds.cern.ch/record/1976186 (cit. on pp. 29, 30).

[57] J. Smith, W. van Neerven and J. Vermaseren, *The Transverse Mass and Width of the W Boson*, Phys. Rev. Lett. **50** (1983) 1738 (cit. on p. 30).

[58] H. Schmitz, *Messung des Verhältnisses der Verzweigungsverhältnisse der Zerfälle W nach Tau + Myon nach Lepton + 3 Myons und W nach Lepton + Myon*, (2019), URL: https://web.physik.uni-bonn.de/group/view.php?%5C&group=1%5C&lang=de%5C&c=t%5C&id=103 (cit. on p. 35).

APPENDIX A

Appendix

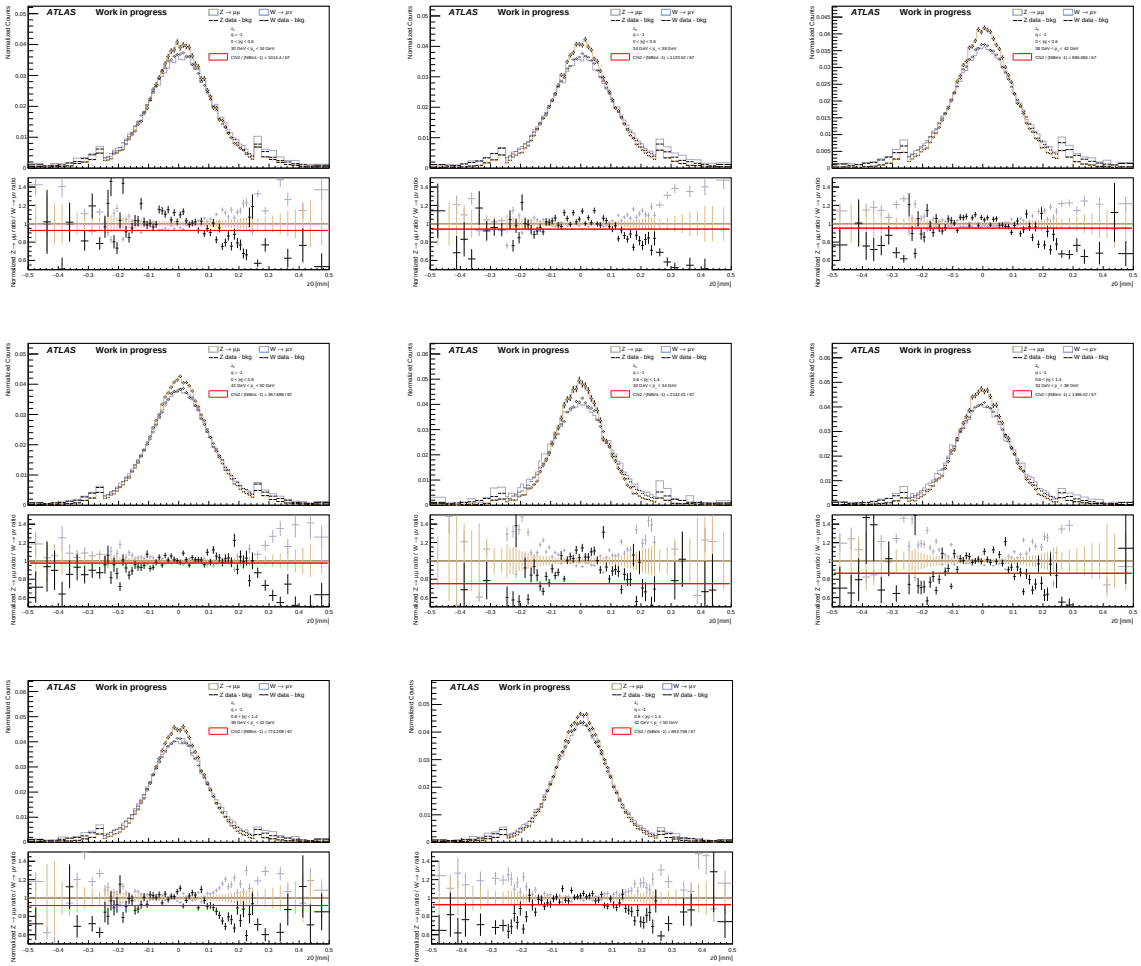

Figure A.1: Calibrated z_0 distributions for negative charge of the W and Z decay in grey and brown, respectively, on the upper panel. On the lower panel is the ratio of MC and data in the respective colors. The double ratio is plotted in black and a fit to it is shown in red. Further information can be found in the legend

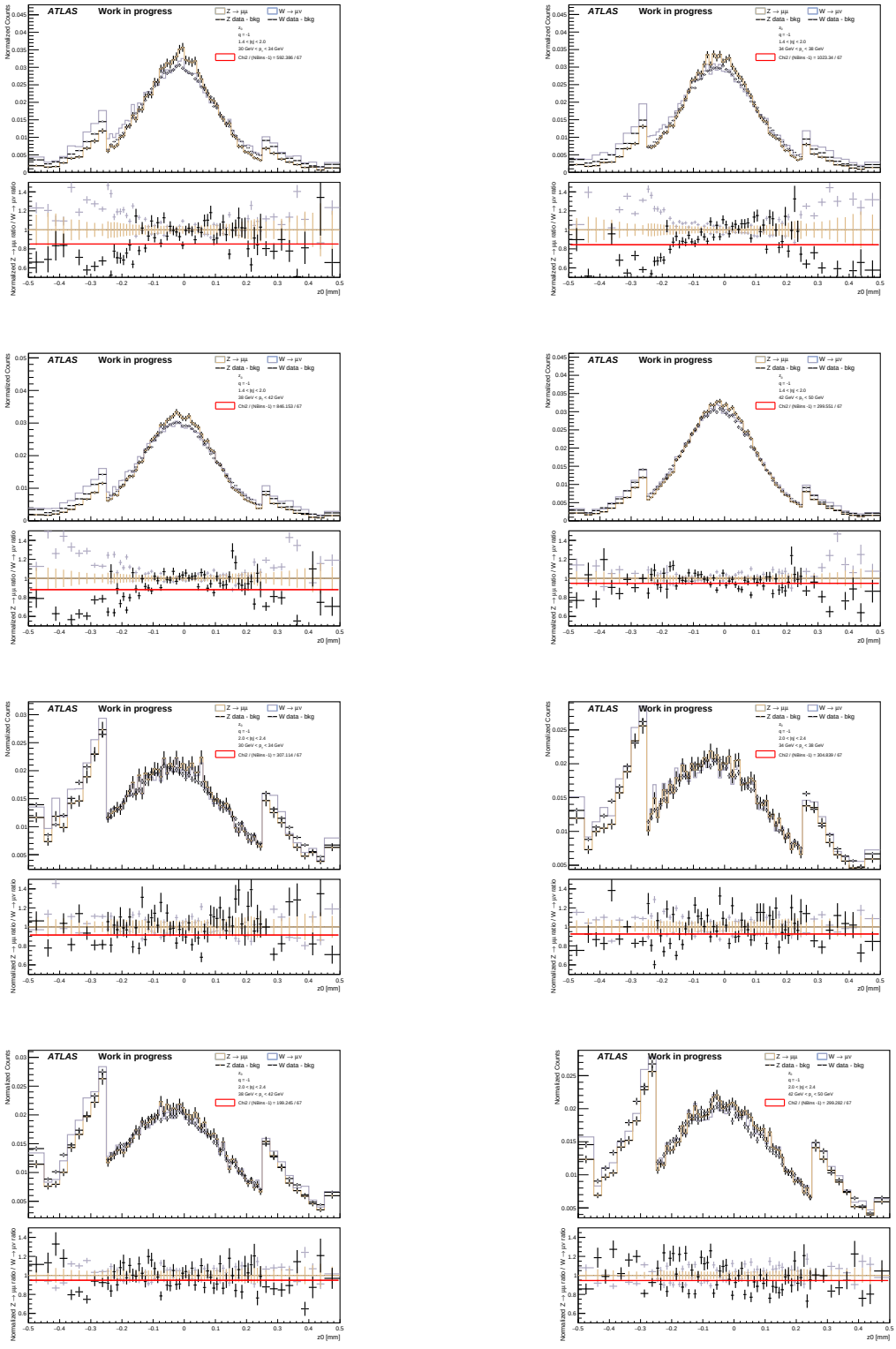

Figure A.2: Calibrated z_0 distributions for negative charge of the W and Z decay in grey and brown, respectively, on the upper panel. On the lower panel is the ratio of MC and data in the respective colors. The double ratio is plotted in black and a fit to it is shown in red. Further information can be found in the legend

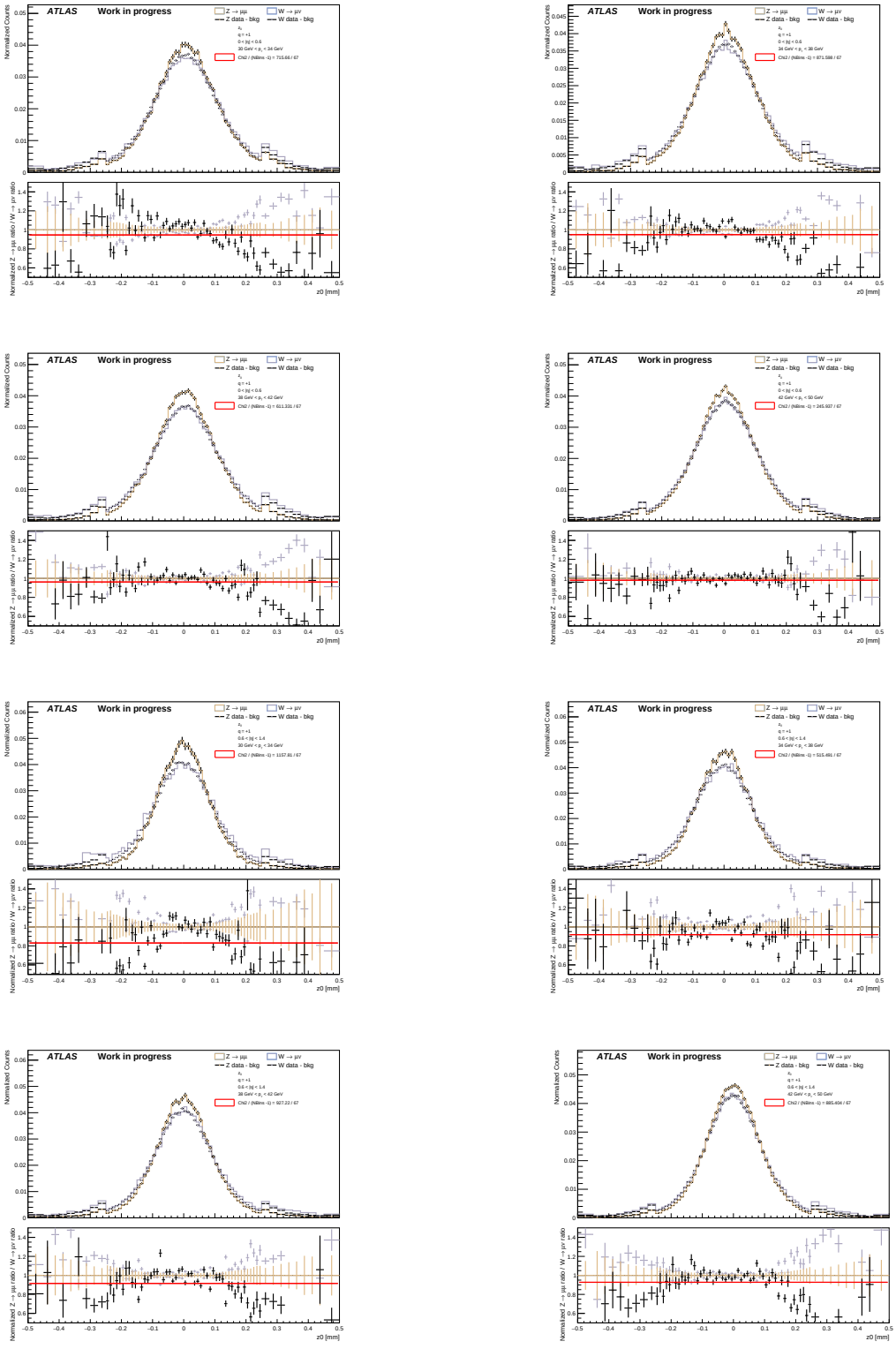

Figure A.3: Calibrated z_0 distributions for positive charge of the W and Z decay in grey and brown, respectively, on the upper panel. On the lower panel is the ratio of MC and data in the respective colors. The double ratio is plotted in black and a fit to it is shown in red. Further information can be found in the legend

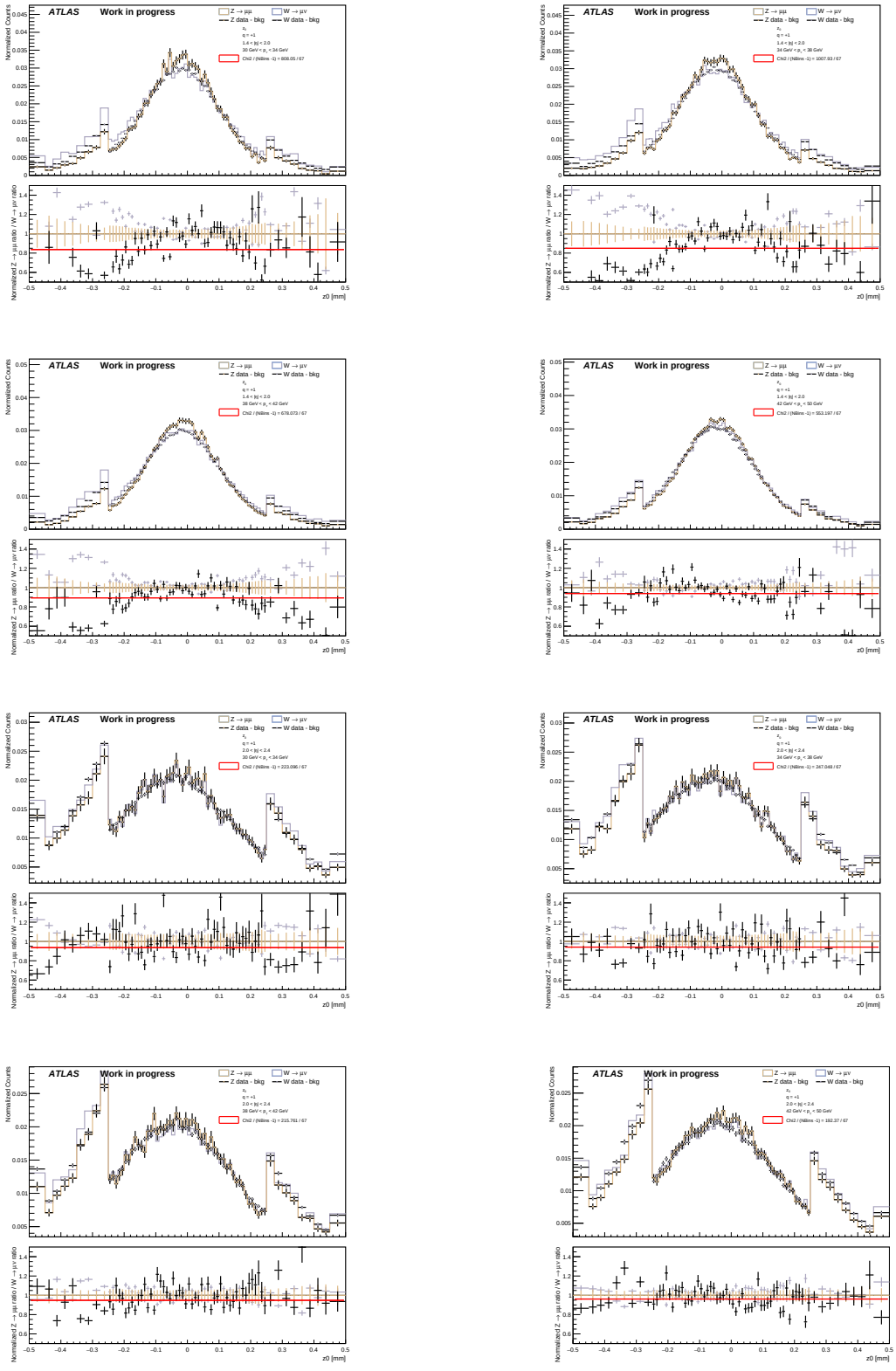

Figure A.4: Calibrated z_0 distributions for positive charge of the W and Z decay in grey and brown, respectively, on the upper panel. On the lower panel is the ratio of MC and data in the respective colors. The double ratio is plotted in black and a fit to it is shown in red. Further information can be found in the legend

APPENDIX B

Appendix

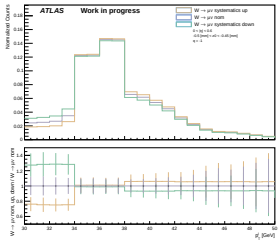

(a) $-0.5\,\text{mm} < z_0 < -0.45\,\text{mm}$

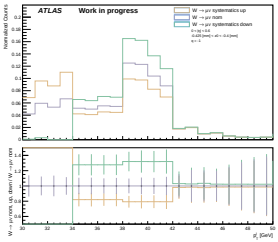

(b) $-0.425\,\text{mm} < z_0 < -0.4\,\text{mm}$

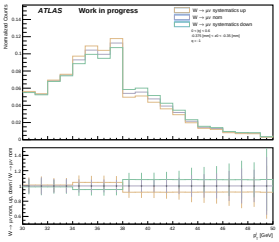

(c) $-0.375\,\text{mm} < z_0 < -0.35\,\text{mm}$

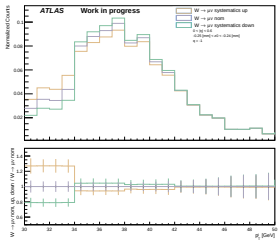

(d) $-0.25\,\text{mm} < z_0 < -0.24\,\text{mm}$

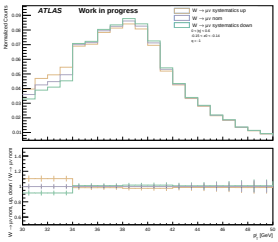

(e) $-0.15\,\text{mm} < z_0 < -0.14\,\text{mm}$

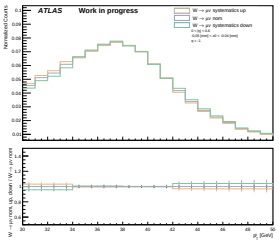

(f) $-0.05\,\text{mm} < z_0 < -0.04\,\text{mm}$

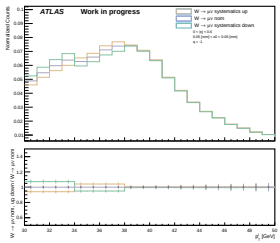

(g) $0.05\,\text{mm} < z_0 < 0.06\,\text{mm}$

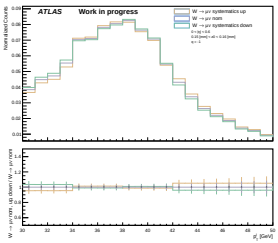

(h) $0.15\,\text{mm} < z_0 < 0.16\,\text{mm}$

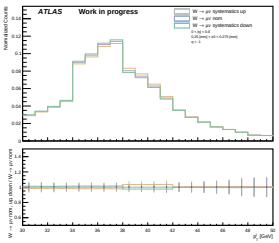

(i) $0.25\,\text{mm} < z_0 < 0.275\,\text{mm}$

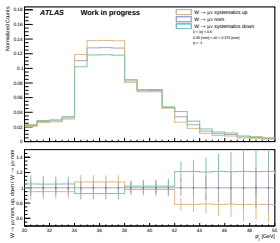

(j) $0.35\,\text{GeV} < z_0 < 0.375\,\text{mm}$

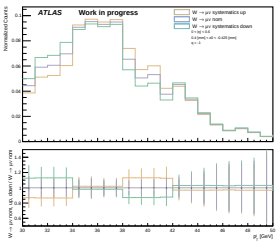

(k) $0.4\,\text{mm} < z_0 < 0.425\,\text{mm}$

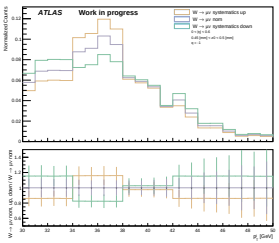

(l) $0.475\,\text{mm} < z_0 < 0.5\,\text{mm}$

Figure B.1: Calibrated p_T distribution of negative charged leptons for $0 < |\eta| < 0.6$ on the upper panel in grey. The systematic uncertainties are plotted as an envelope in brown and green. The lower panel displays the ratio of the different distribution and nominal one.

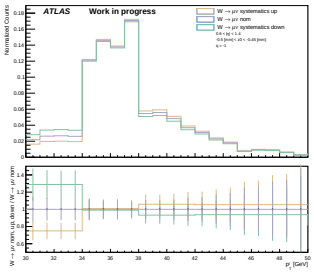

(a) $-0.5\,\text{mm} < z_0 < -0.45\,\text{mm}$

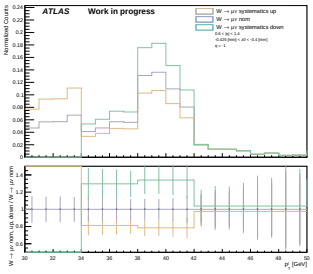

(b) $-0.425\,\text{mm} < z_0 < -0.4\,\text{mm}$

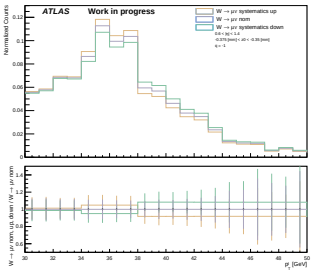

(c) $-0.375\,\text{mm} < z_0 < -0.35\,\text{mm}$

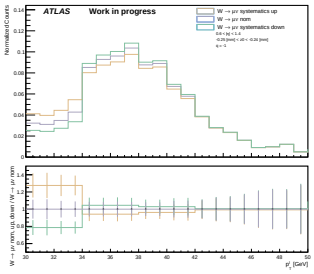

(d) $-0.375\,\text{mm} < z_0 < -0.35\,\text{mm}$

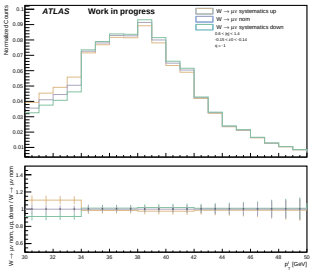

(e) $-0.15\,\text{mm} < z_0 < -0.14\,\text{mm}$

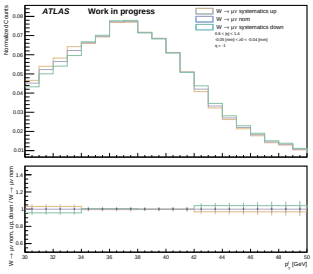

(f) $-0.05\,\text{mm} < z_0 < -0.04\,\text{mm}$

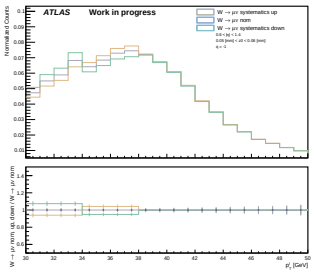

(g) $0.05\,\text{mm} < z_0 < 0.06\,\text{mm}$

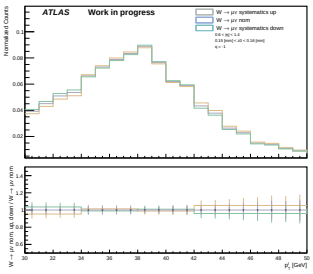

(h) $0.15\,\text{mm} < z_0 < 0.16\,\text{mm}$

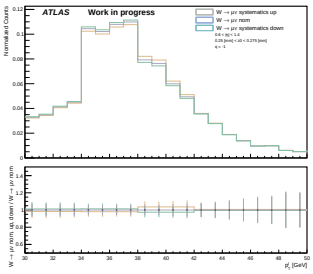

(i) $0.25\,\text{mm} < z_0 < 0.275\,\text{mm}$

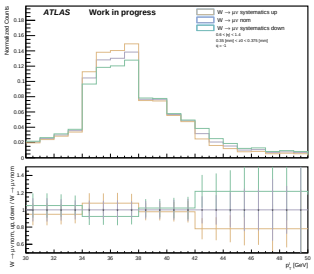

(j) $0.35\,\text{GeV} < z_0 < 0.375\,\text{mm}$

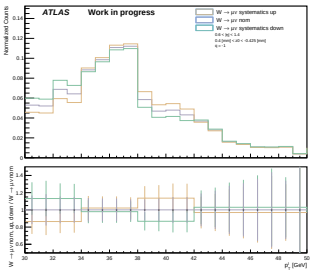

(k) $0.4\,\text{mm} < z_0 < 0.425\,\text{mm}$

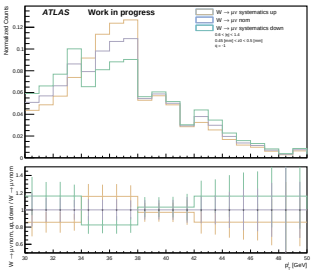

(l) $0.475\,\text{mm} < z_0 < 0.5\,\text{mm}$

Figure B.2: Calibrated p_T distribution of negative charged leptons for $0.6 < |\eta| < 1.4$ on the upper panel in grey. The systematic uncertainties are plotted as an envelope in brown and green. The lower panel displays the ratio of the different distribution and nominal one.

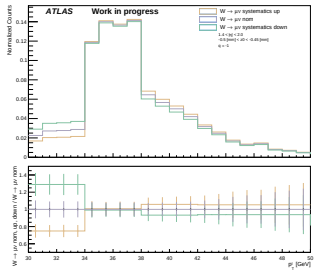

(a) $-0.5\,\text{mm} < z_0 < -0.45\,\text{mm}$

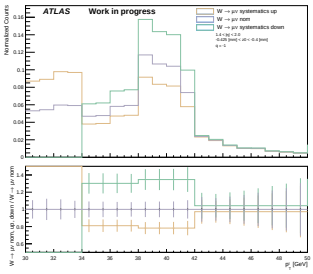

(b) $-0.425\,\text{mm} < z_0 < -0.4\,\text{mm}$

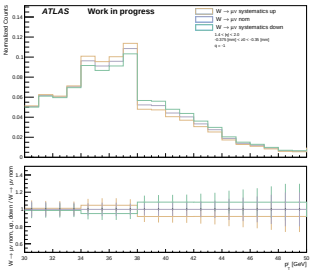

(c) $-0.375\,\text{mm} < z_0 < -0.35\,\text{mm}$

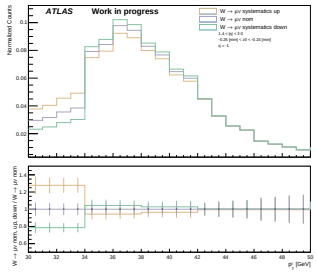

(d) $-0.375\,\text{mm} < z_0 < -0.35\,\text{mm}$

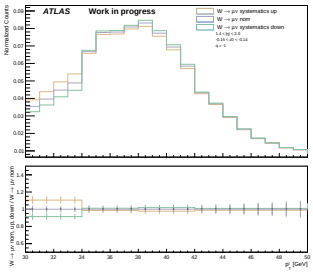

(e) $-0.15\,\text{mm} < z_0 < -0.14\,\text{mm}$

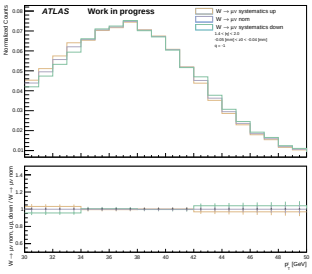

(f) $-0.05\,\text{mm} < z_0 < -0.04\,\text{mm}$

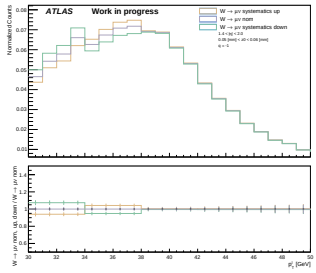

(g) $0.05\,\text{mm} < z_0 < 0.06\,\text{mm}$

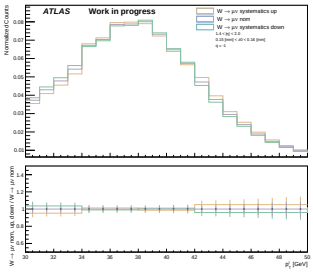

(h) $0.15\,\text{mm} < z_0 < 0.16\,\text{mm}$

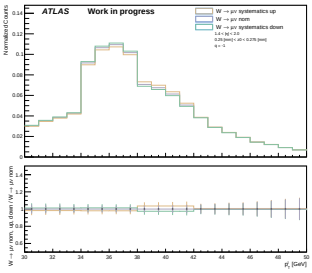

(i) $0.25\,\text{mm} < z_0 < 0.275\,\text{mm}$

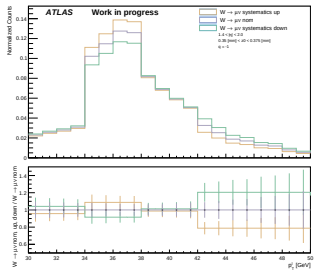

(j) $0.35\,\text{mm} < z_0 < 0.375\,\text{mm}$, $q = -1$

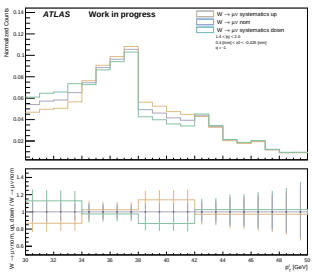

(k) $0.4\,\text{mm} < z_0 < 0.425\,\text{mm}$

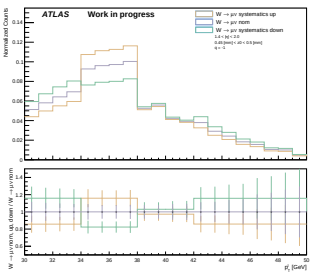

(l) $0.475\,\text{mm} < z_0 < 0.5\,\text{mm}$

Figure B.3: Calibrated p_T distribution of negative charged leptons for $1.4 < |\eta| < 2.0$ on the upper panel in grey. The systematic uncertainties are plotted as an envelope in brown and green. The lower panel displays the ratio of the different distribution and nominal one.

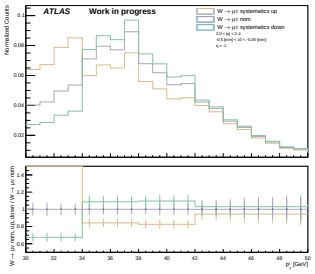

(a) $-0.5\,\text{mm} < z_0 < -0.45\,\text{mm}$

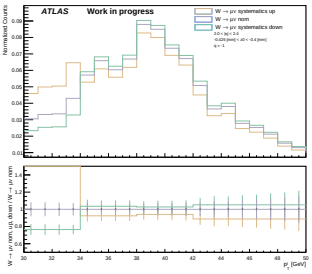

(b) $-0.425\,\text{mm} < z_0 < -0.4\,\text{mm}$

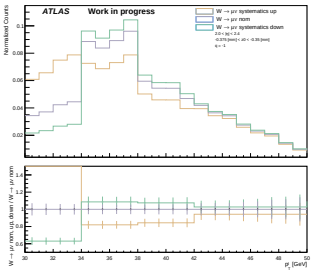

(c) $-0.375\,\text{mm} < z_0 < -0.35\,\text{mm}$

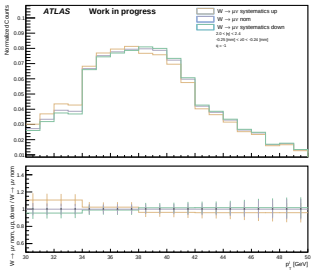

(d) $-0.375\,\text{mm} < z_0 < -0.35\,\text{mm}$

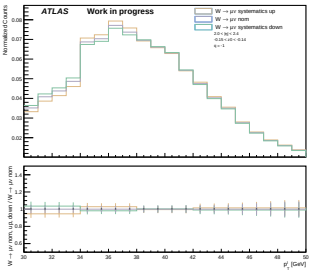

(e) $-0.15\,\text{mm} < z_0 < -0.14\,\text{mm}$

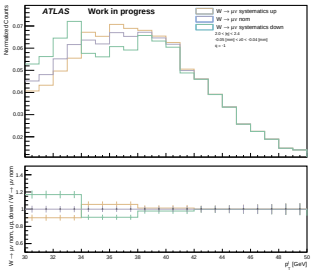

(f) $-0.05\,\text{mm} < z_0 < -0.04\,\text{mm}$

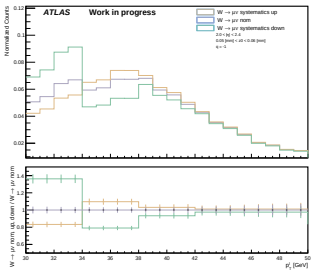

(g) $0.05\,\text{mm} < z_0 < 0.06\,\text{mm}$

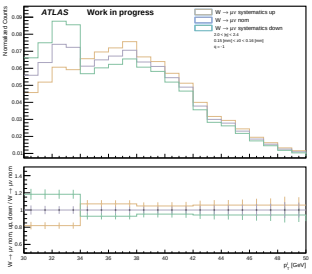

(h) $0.15\,\text{mm} < z_0 < 0.16\,\text{mm}$

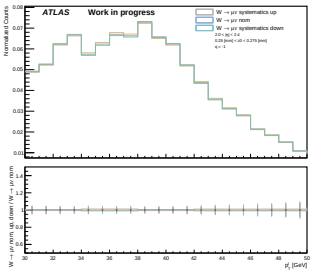

(i) $0.25\,\text{mm} < z_0 < 0.275\,\text{mm}$

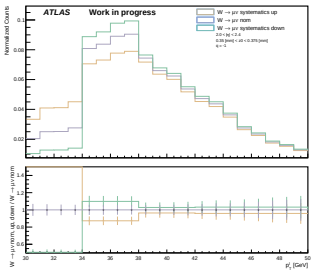

(j) $0.35\,\text{mm} < z_0 < 0.375\,\text{mm}$

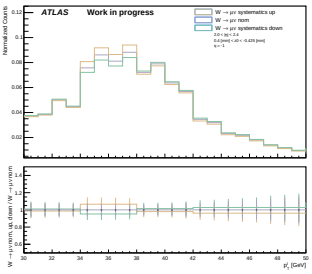

(k) $0.4\,\text{mm} < z_0 < 0.425\,\text{mm}$

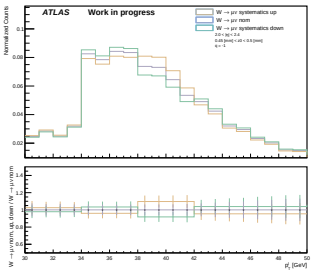

(l) $0.475\,\text{mm} < z_0 < 0.5\,\text{mm}$

Figure B.4: Calibrated p_T distribution of negative charged leptons for $2.0 < |\eta| < 2.4$ on the upper panel in grey. The systematic uncertainties are plotted as an envelope in brown and green. The lower panel displays the ratio of the different distribution and nominal one.

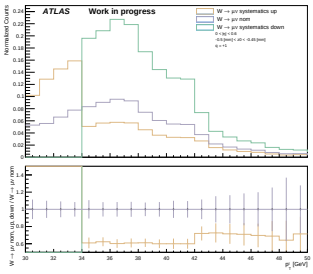

(a) $-0.5\,\text{mm} < z_0 < -0.45\,\text{mm}$

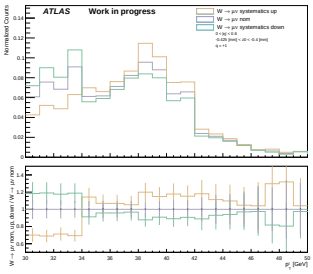

(b) $-0.425\,\text{mm} < z_0 < -0.4\,\text{mm}$

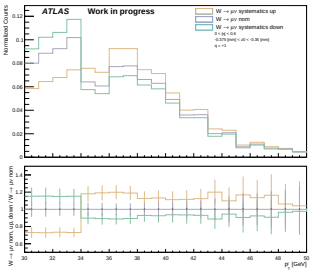

(c) $-0.375\,\text{mm} < z_0 < -0.35\,\text{mm}$

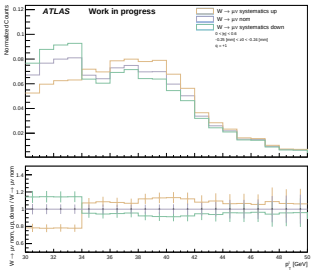

(d) $-0.25\,\text{mm} < z_0 < -0.24\,\text{mm}$

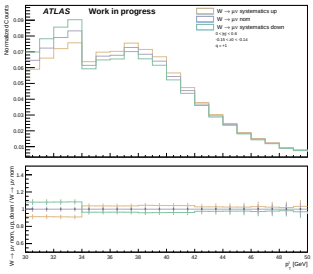

(e) $-0.15\,\text{mm} < z_0 < -0.14\,\text{mm}$

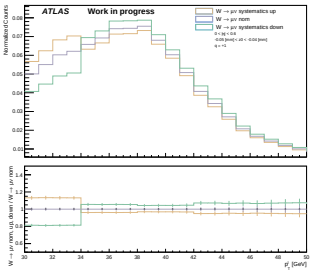

(f) $-0.05\,\text{mm} < z_0 < -0.04\,\text{mm}$

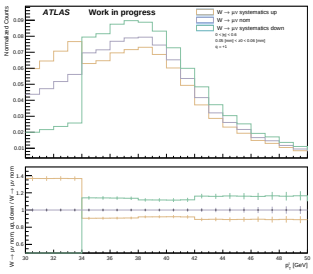

(g) $0.05\,\text{mm} < z_0 < 0.06\,\text{mm}$

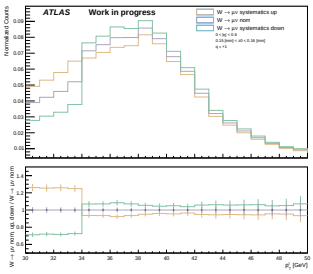

(h) $0.15\,\text{mm} < z_0 < 0.16\,\text{mm}$

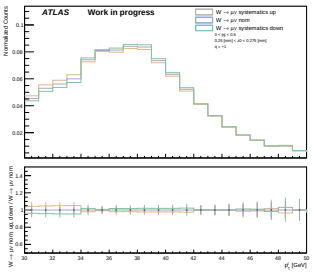

(i) $0.25\,\text{mm} < z_0 < 0.275\,\text{mm}$

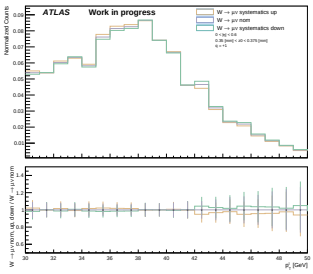

(j) $0.35\,\text{GeV} < z_0 < 0.375\,\text{mm}$

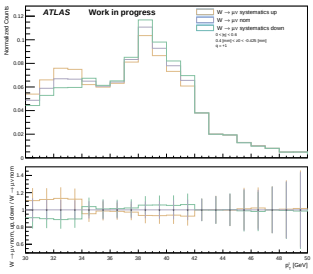

(k) $0.4\,\text{mm} < z_0 < 0.425\,\text{mm}$

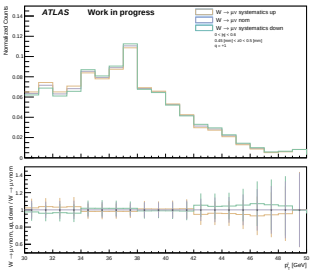

(l) $0.475\,\text{mm} < z_0 < 0.5\,\text{mm}$

Figure B.5: Calibrated p_T distribution of positive charged leptons for $0 < |\eta| < 0.6$ on the upper panel in grey. The systematic uncertainties are plotted as an envelope in brown and green. The lower panel displays the ratio of the different distribution and nominal one.

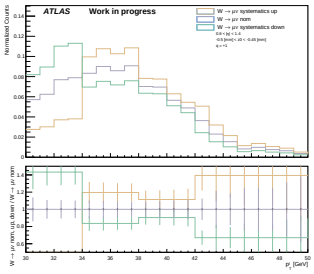

(a) $-0.5\,\text{mm} < z_0 < -0.45\,\text{mm}$

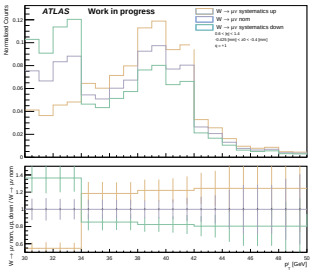

(b) $-0.425\,\text{mm} < z_0 < -0.4\,\text{mm}$

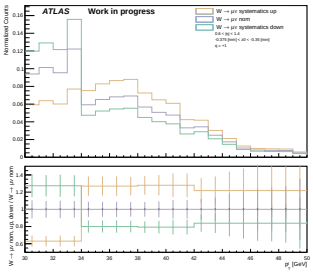

(c) $-0.375\,\text{mm} < z_0 < -0.35\,\text{mm}$

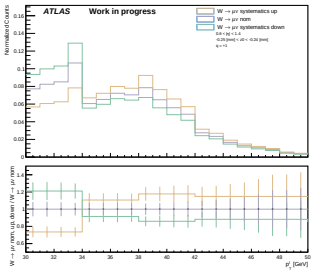

(d) $-0.375\,\text{mm} < z_0 < -0.35\,\text{mm}$

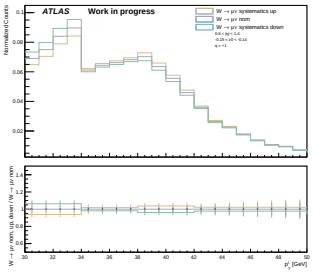

(e) $-0.15\,\text{mm} < z_0 < -0.14\,\text{mm}$

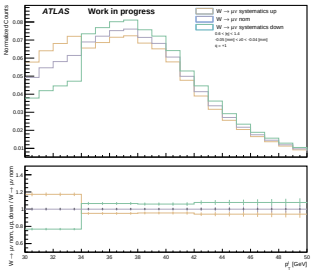

(f) $-0.05\,\text{mm} < z_0 < -0.04\,\text{mm}$

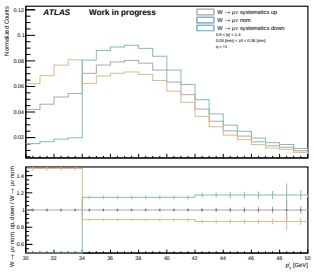

(g) $0.05\,\text{mm} < z_0 < 0.06\,\text{mm}$

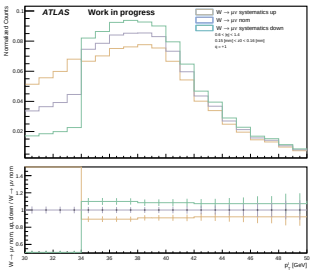

(h) $0.15\,\text{mm} < z_0 < 0.16\,\text{mm}$

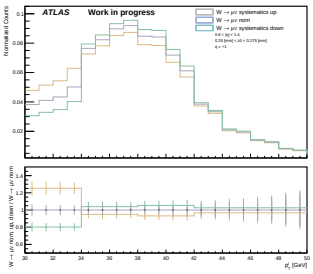

(i) $0.25\,\text{mm} < z_0 < 0.275\,\text{mm}$

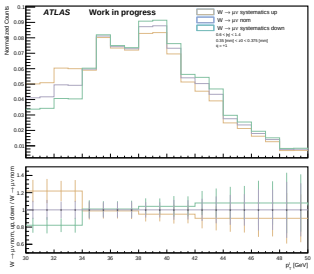

(j) $0.35\,\text{GeV} < z_0 < 0.375\,\text{mm}$

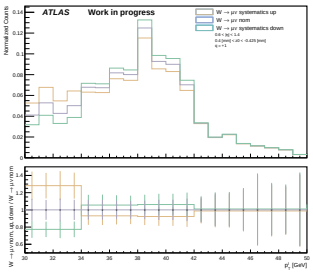

(k) $0.4\,\text{mm} < z_0 < 0.425\,\text{mm}$

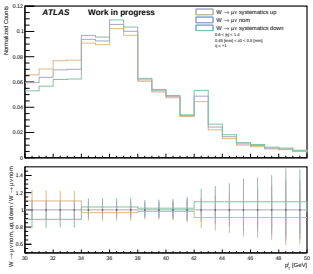

(l) $0.475\,\text{mm} < z_0 < 0.5\,\text{mm}$

Figure B.6: Calibrated p_T distribution of positive charged leptons for $0.6 < |\eta| < 1.4$ on the upper panel in grey. The systematic uncertainties are plotted as an envelope in brown and green. The lower panel displays the ratio of the different distribution and nominal one.

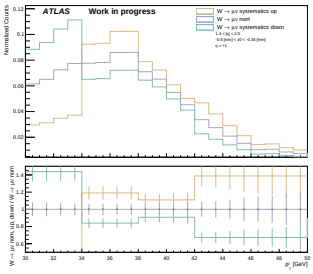

(a) $-0.5\,\text{mm} < z_0 < -0.45\,\text{mm}$

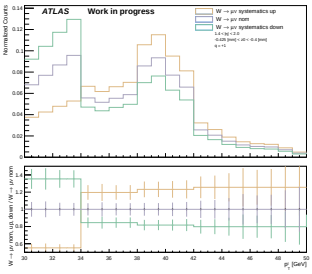

(b) $-0.425\,\text{mm} < z_0 < -0.4\,\text{mm}$

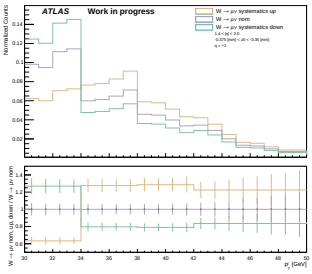

(c) $-0.375\,\text{mm} < z_0 < -0.35\,\text{mm}$

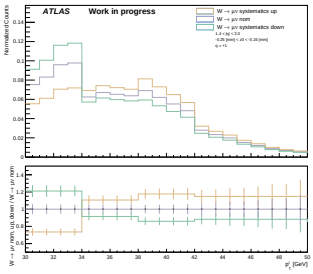

(d) $-0.375\,\text{mm} < z_0 < -0.35\,\text{mm}$

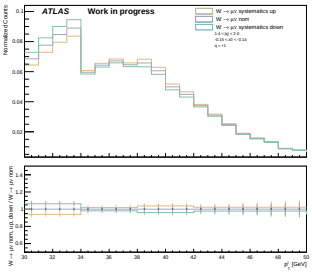

(e) $-0.15\,\text{mm} < z_0 < -0.14\,\text{mm}$

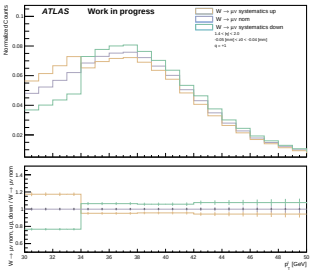

(f) $-0.05\,\text{mm} < z_0 < -0.04\,\text{mm}$

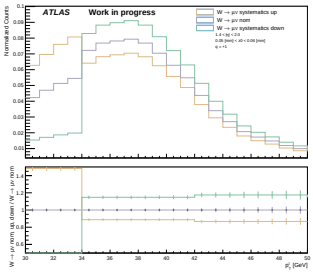

(g) $0.05\,\text{mm} < z_0 < 0.06\,\text{mm}$

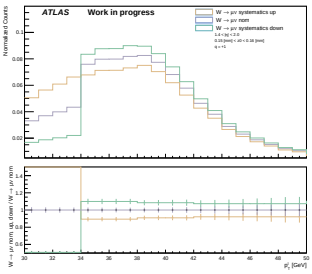

(h) $0.15\,\text{mm} < z_0 < 0.16\,\text{mm}$

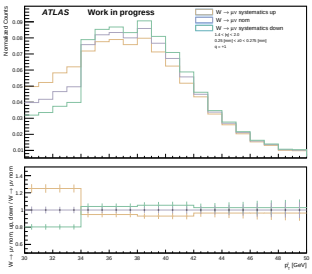

(i) $0.25\,\text{mm} < z_0 < 0.275\,\text{mm}$

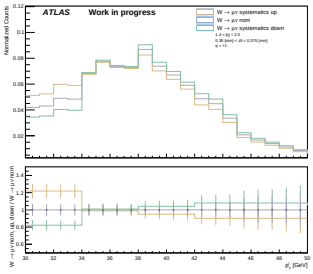

(j) $0.35\,\text{mm} < z_0 < 0.375\,\text{mm}$

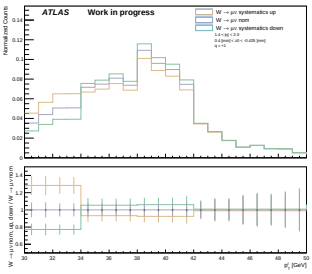

(k) $0.4\,\text{mm} < z_0 < 0.425\,\text{mm}$

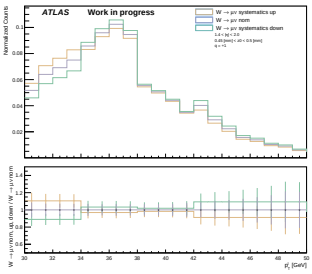

(l) $0.475\,\text{mm} < z_0 < 0.5\,\text{mm}$

Figure B.7: Calibrated p_T distribution of positve charged leptons for $1.4 < |\eta| < 2.0$ on the upper panel in grey. The systematic uncertainties are plotted as an envelope in brown and green. The lower panel displays the ratio of the different distribution and nominal one.

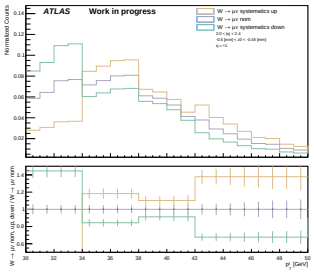

(a) $-0.5\,\text{mm} < z_0 < -0.45\,\text{mm}$

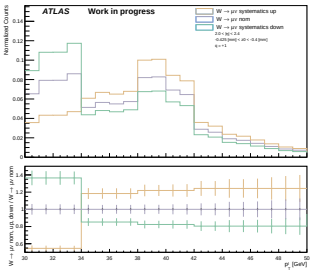

(b) $-0.425\,\text{mm} < z_0 < -0.4\,\text{mm}$

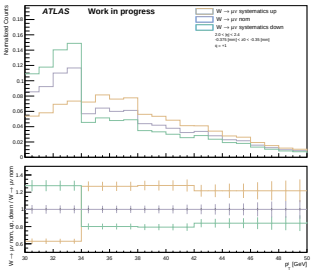

(c) $2.0 < |\eta| < 2.4$, $-0.375\,\text{mm} < z_0 < -0.35\,\text{mm}$

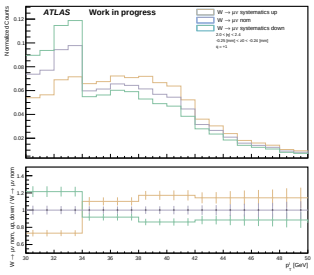

(d) $-0.375\,\text{mm} < z_0 < -0.35\,\text{mm}$

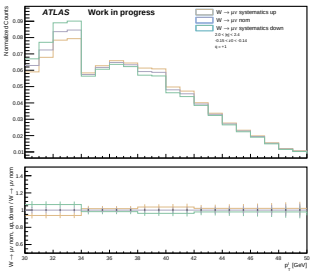

(e) $-0.15\,\text{mm} < z_0 < -0.14\,\text{mm}$

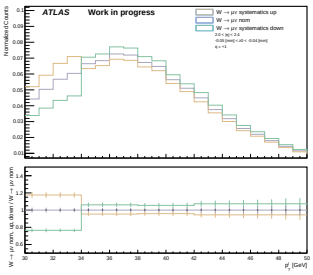

(f) $-0.05\,\text{mm} < z_0 < -0.04\,\text{mm}$

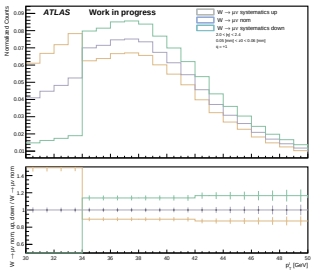

(g) $0.05\,\text{mm} < z_0 < 0.06\,\text{mm}$

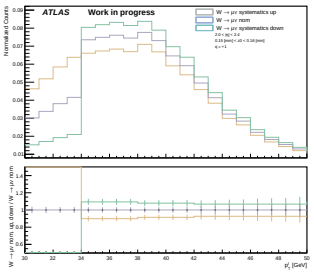

(h) $0.15\,\text{mm} < z_0 < 0.16\,\text{mm}$

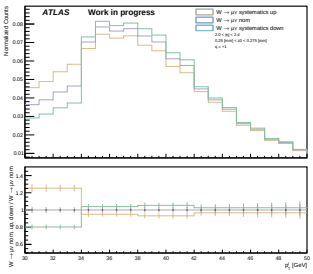

(i) $0.25\,\text{mm} < z_0 < 0.275\,\text{mm}$

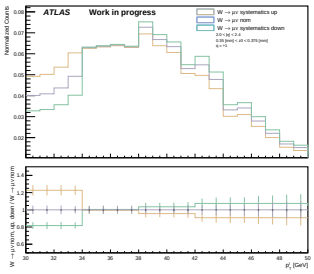

(j) $0.35\,\text{mm} < z_0 < 0.375\,\text{mm}$

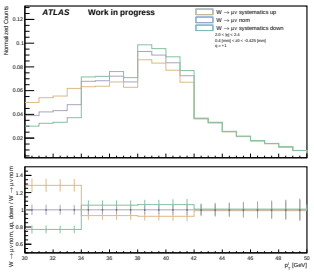

(k) $0.4\,\text{mm} < z_0 < 0.425\,\text{mm}$

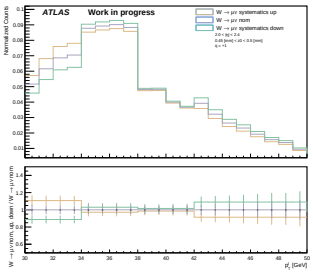

(l) $0.475\,\text{mm} < z_0 < 0.5\,\text{mm}$

Figure B.8: Calibrated p_T distribution of positive charged leptons for $2.0 < |\eta| < 2.4$ on the upper panel in grey. The systematic uncertainties are plotted as an envelope in brown and green. The lower panel displays the ratio of the different distribution and nominal one.

APPENDIX C

Appendix

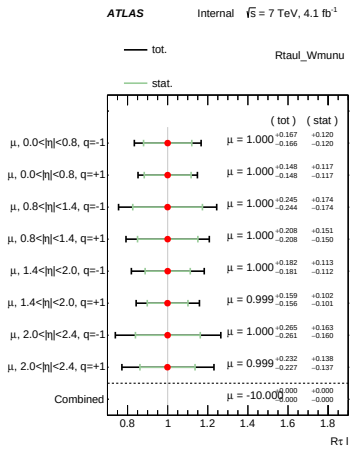

(a) $z_0/\sigma(z_0)$, 14 Bins, with Systematics

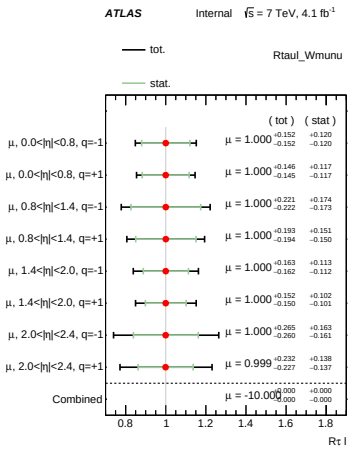

(b) $z_0/\sigma(z_0)$, 14 Bins, without Systematics

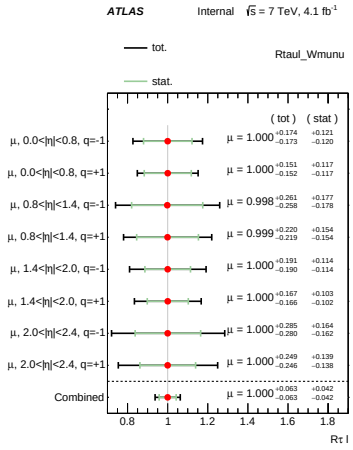

(c) $z_0/\sigma(z_0)$, 8 Bins, with Systematics

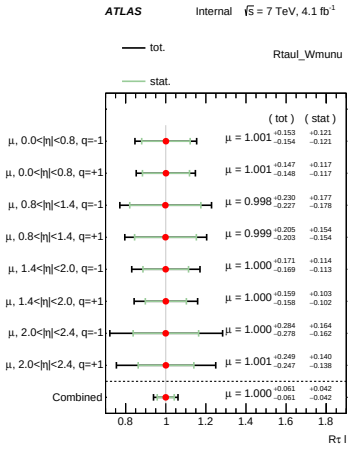

(d) $z_0/\sigma(z_0)$, 8 Bins, without Systematics

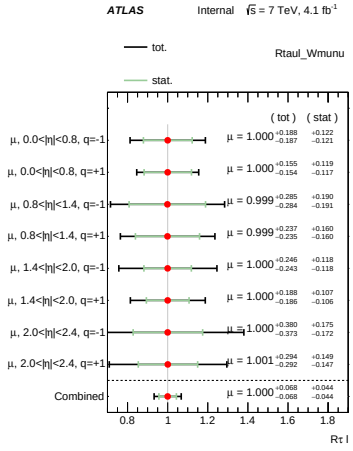

(e) $z_0/\sigma(z_0)$, 4 Bins, with Systematics

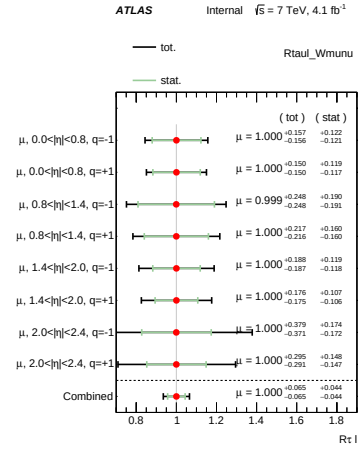

(f) $z_0/\sigma(z_0)$, 4 Bins, without Systematics

Figure C.1: Fit result of $R_{\tau\ell}$ for $z_0/\sigma(z_0)$, different charges, pseudorapidties and bins

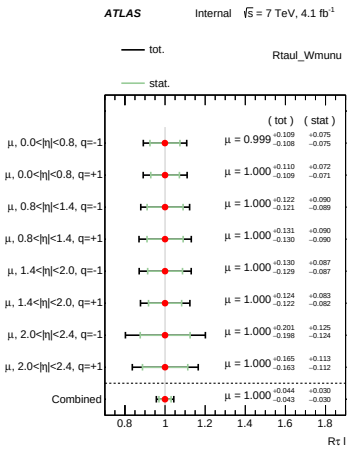

(a) d_0, 14 Bins, with Systematics

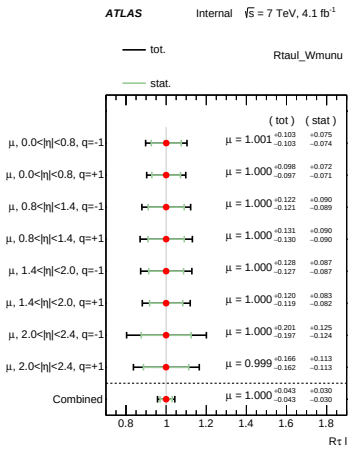

(b) d_0, 14 Bins, without Systematics

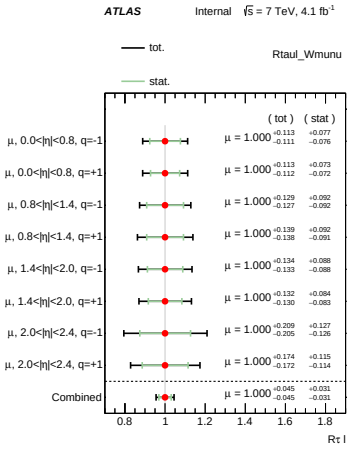

(c) d_0, 8 Bins, with Systematics

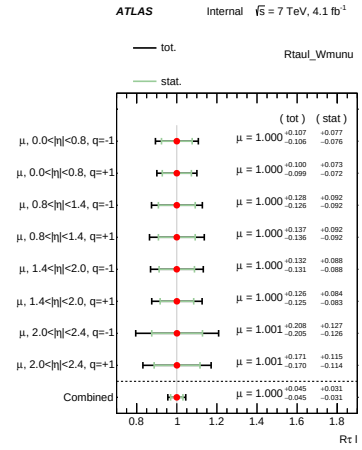

(d) d_0, 8 Bins, without Systematics

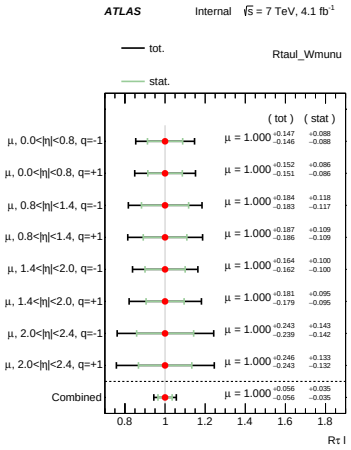

(e) d_0, 4 Bins, with Systematics

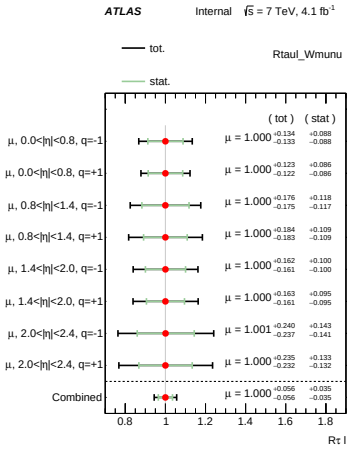

(f) d_0, 4 Bins, without Systematics

Figure C.2: Fit result of $R_{\tau\ell}$ for d_0, different charges, pseudorapidties and bins

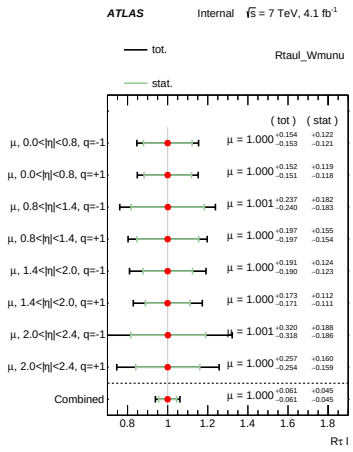

(a) z_0, 14 Bins, with Systematics

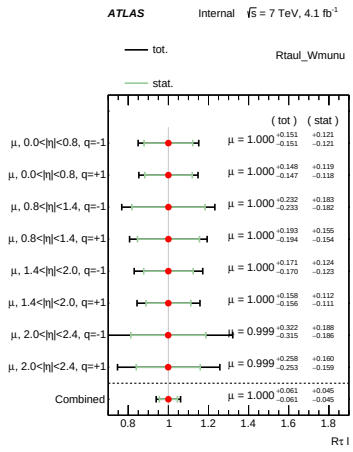

(b) z_0, 14 Bins, without Systematics

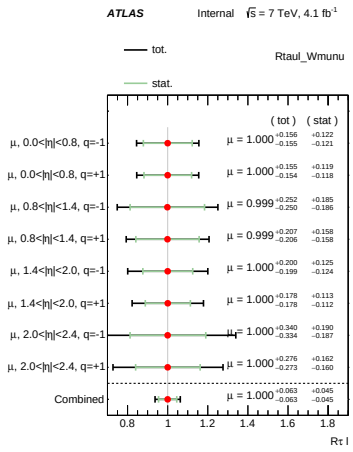

(c) d_0, 8 Bins, with Systematics

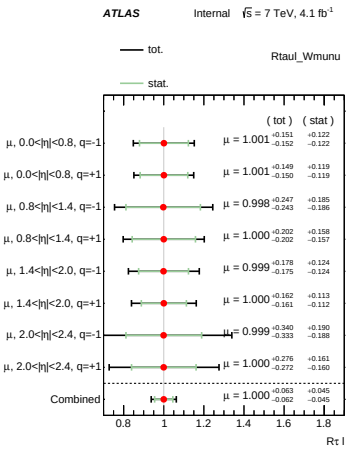

(d) d_0, 8 Bins, without Systematics

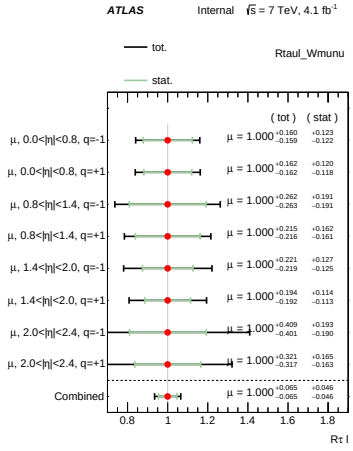

(e) d_0, 4 Bins, with Systematics

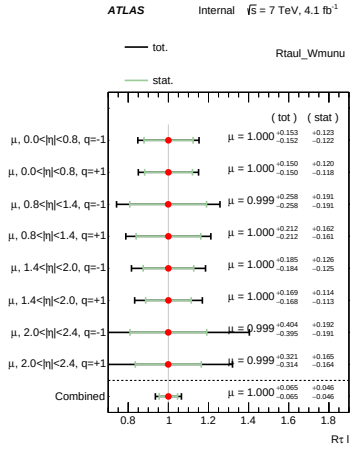

(f) d_0, 4 Bins, without Systematics

Figure C.3: Fit result of $R_{\tau\ell}$ for z_0, different charges, pseudorapidties and bins

APPENDIX D

Appendix

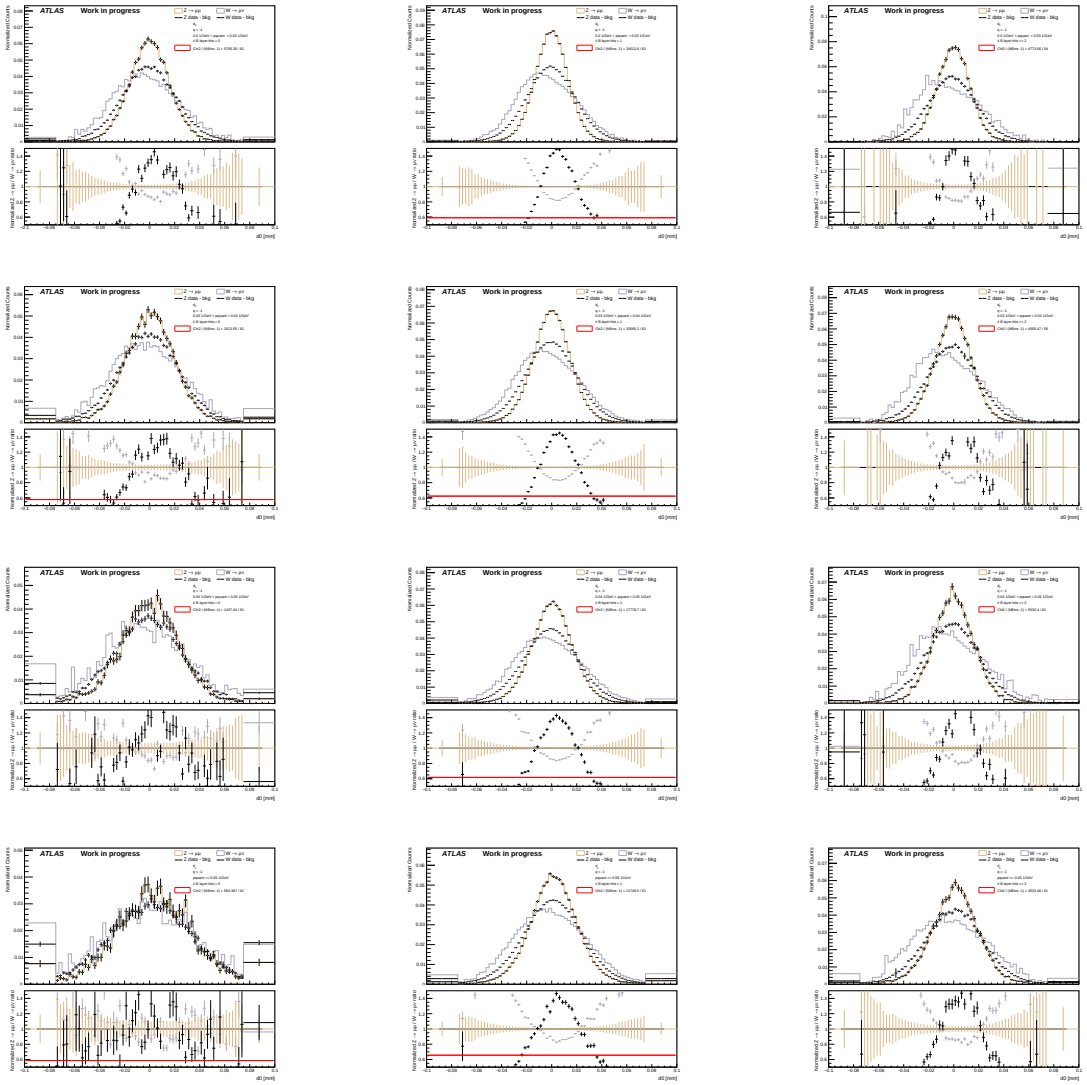

Figure D.1: Calibrated double ratio of the new calibration. The shown plots represent the distribution for negative charge. The different columns show the three different nBL bins, the different rows show the four pquant bins. Detailed information can be found in the legend of each plot

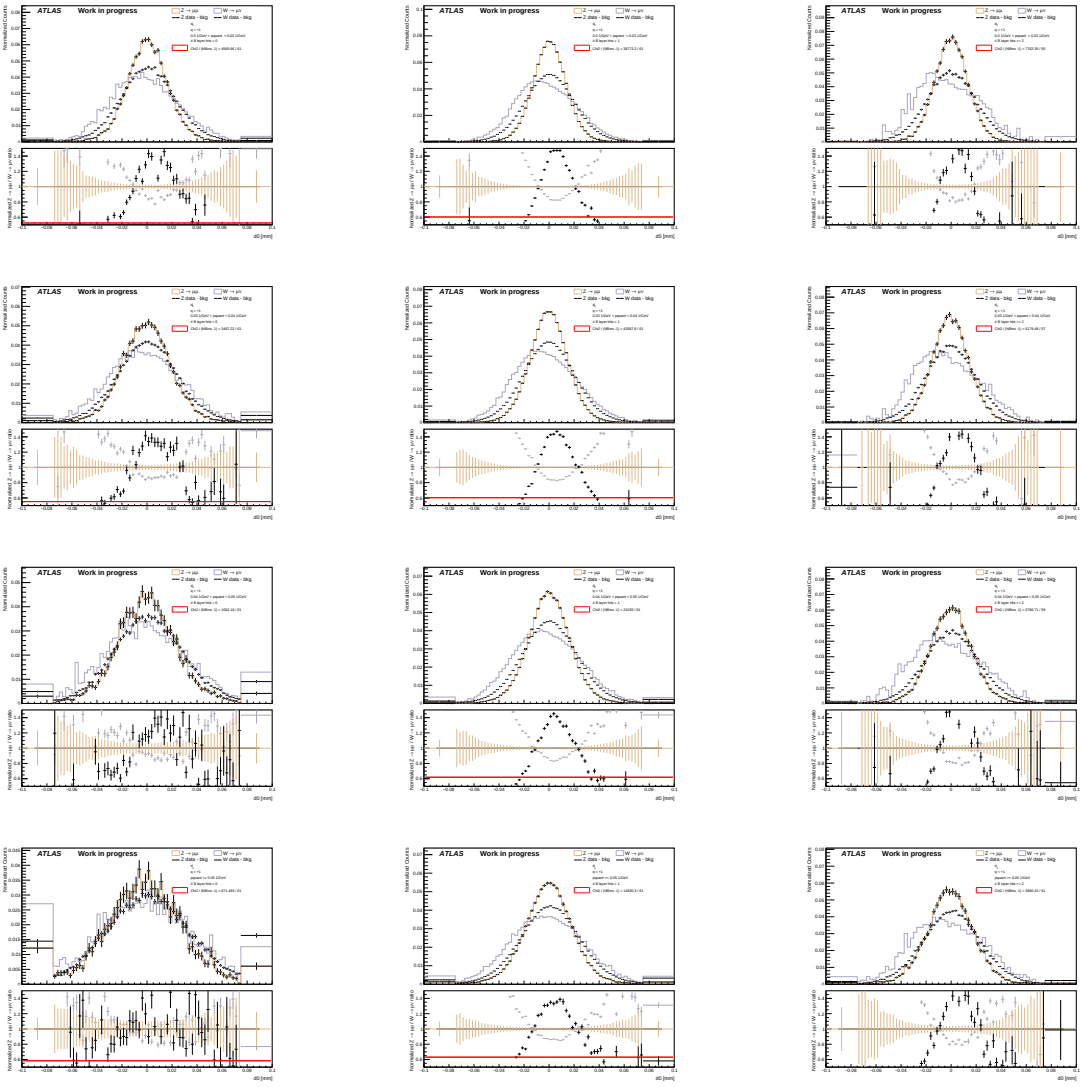

Figure D.2: Calibrated double ratio of the new calibration. The shown plots represent the distribution for positive charge. The different columns show the three different nBL bins, the different rows show the four pquant bins. Detailed information can be found in the legend of each plot

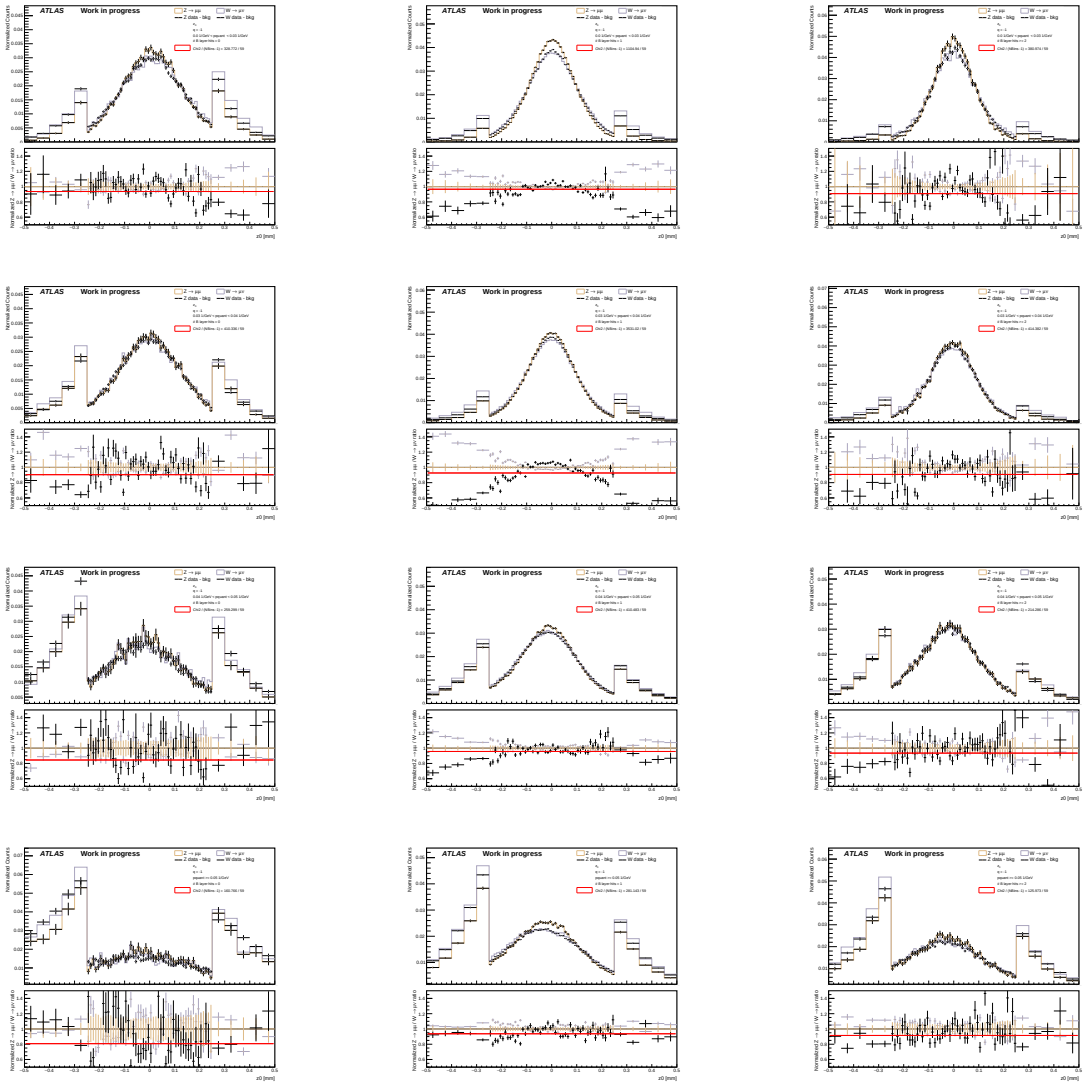

Figure D.3: Calibrated double ratio of the new calibration. The shown plots represent the distribution for negative charge. The different columns show the three different nBL bins, the different rows show the four pquant bins. Detailed information can be found in the legend of each plot

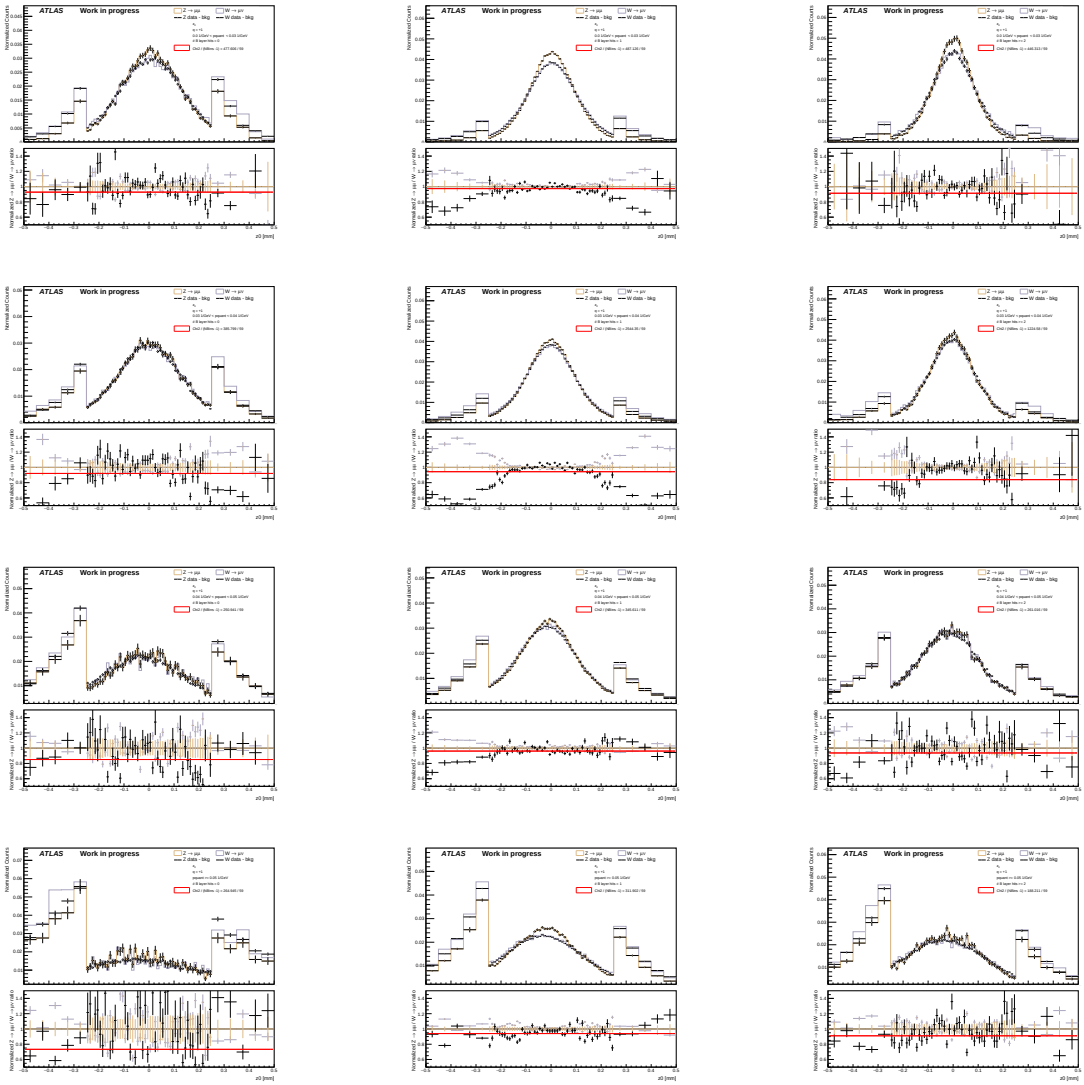

Figure D.4: Calibrated double ratio of the new calibration. The shown plots represent the distribution for positive charge. The different columns show the three different nBL bins, the different rows show the four pquant bins. Detailed information can be found in the legend of each plot

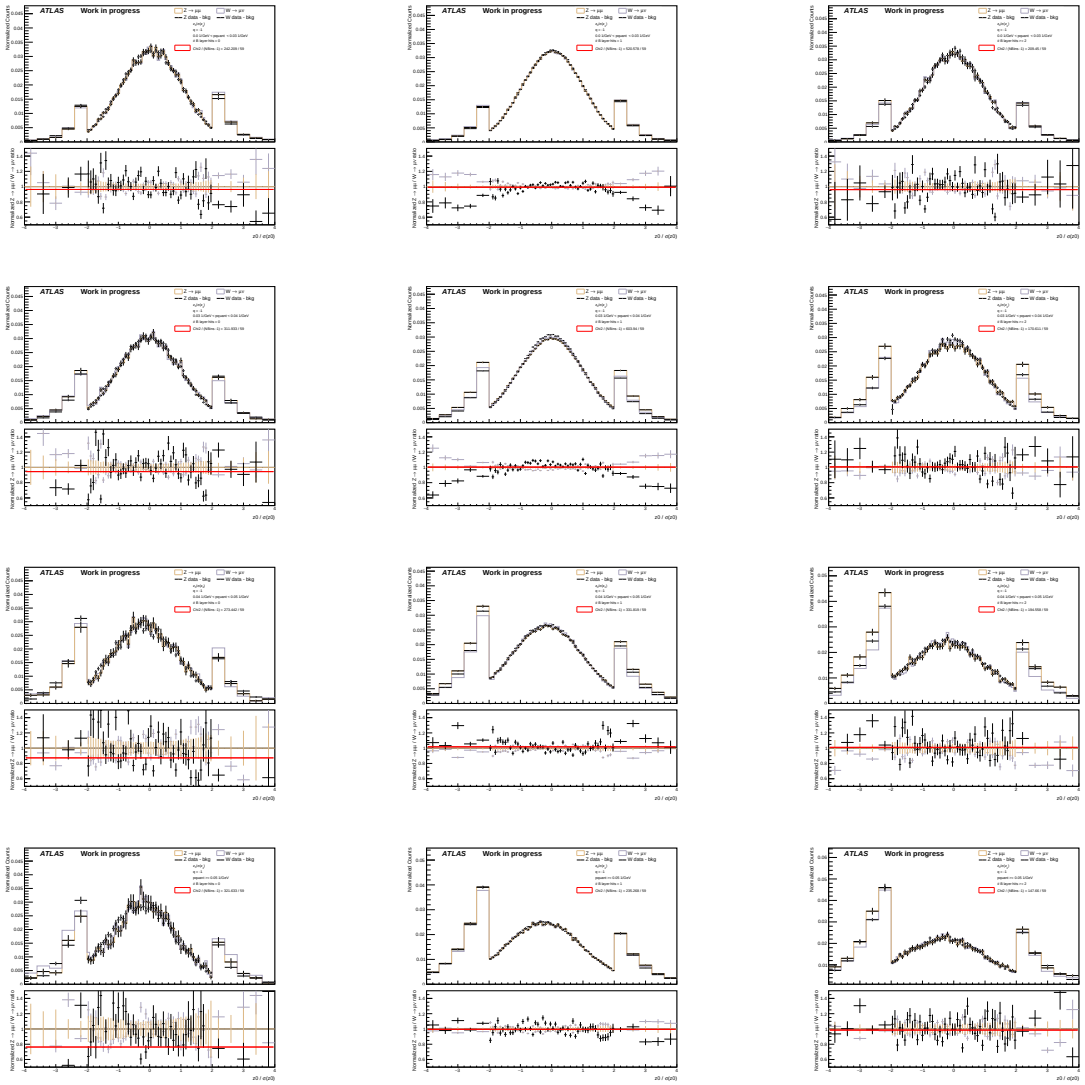

Figure D.5: Calibrated double ratio of the new calibration. The shown plots represent the distribution for negative charge. The different columns show the three different nBL bins, the different rows show the four pquant bins. Detailed information can be found in the legend of each plot

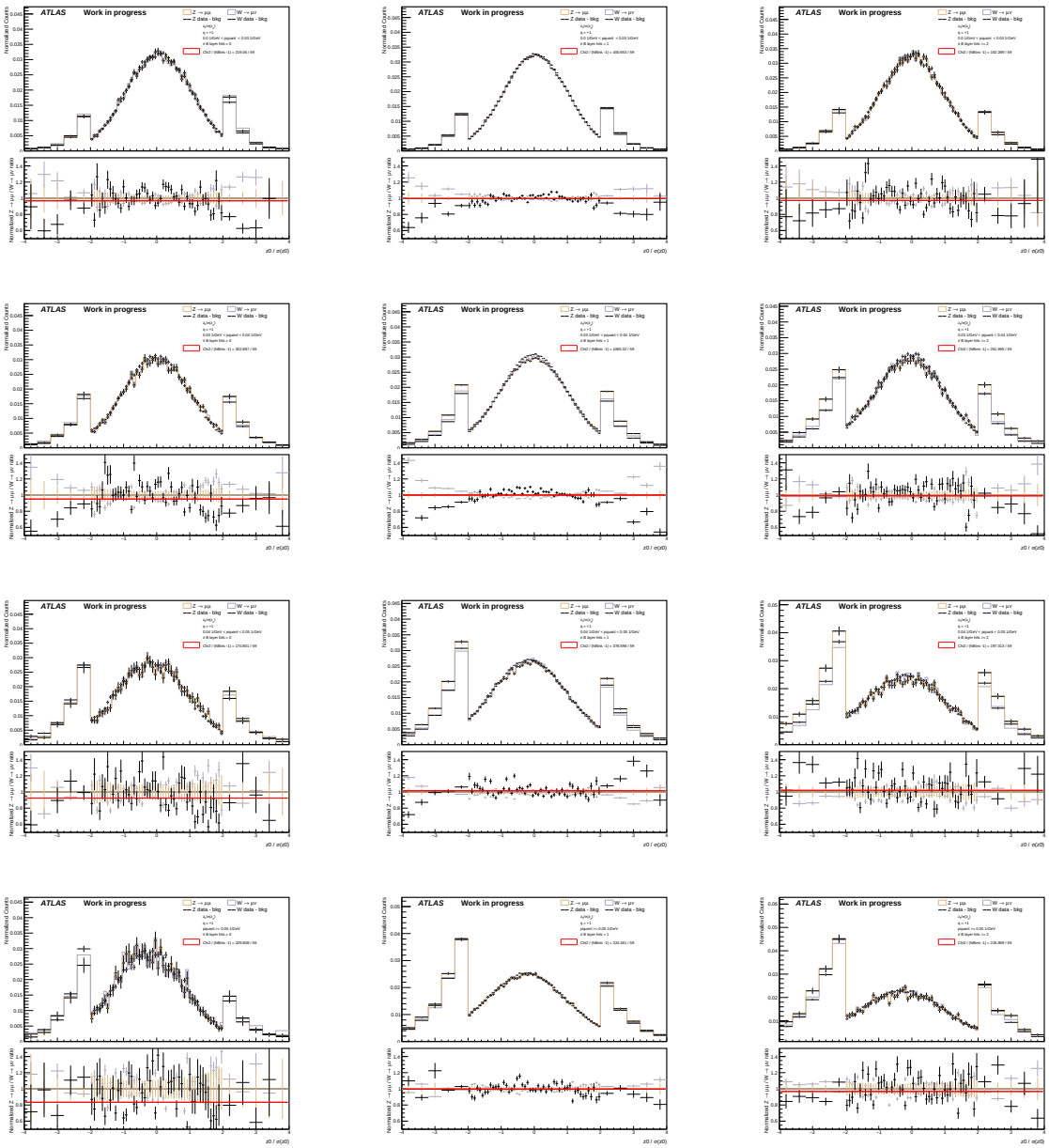

Figure D.6: Calibrated double ratio of the new calibration. The shown plots represent the distribution for positive charge. The different columns show the three different nBL bins, the different rows show the four pquant bins. Detailed information can be found in the legend of each plot

APPENDIX E

Appendix

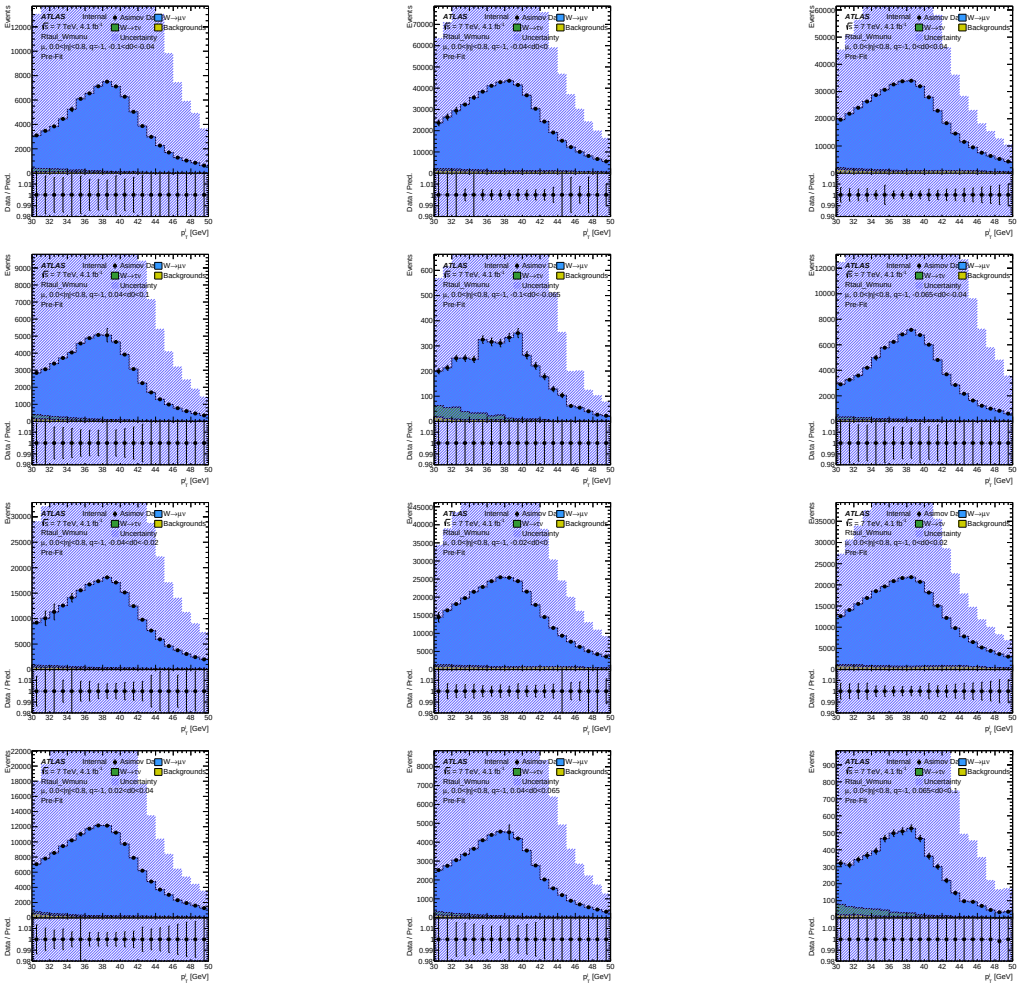

Figure E.1: p_T fit for d_0 in 4 and 8 bins. Not all slices could be shown thus as an example only $0 < |\eta| < 0.8$ and $q = -1$ is shown. Lower panel shows ratio of data and MC. Further information can be found in the legend

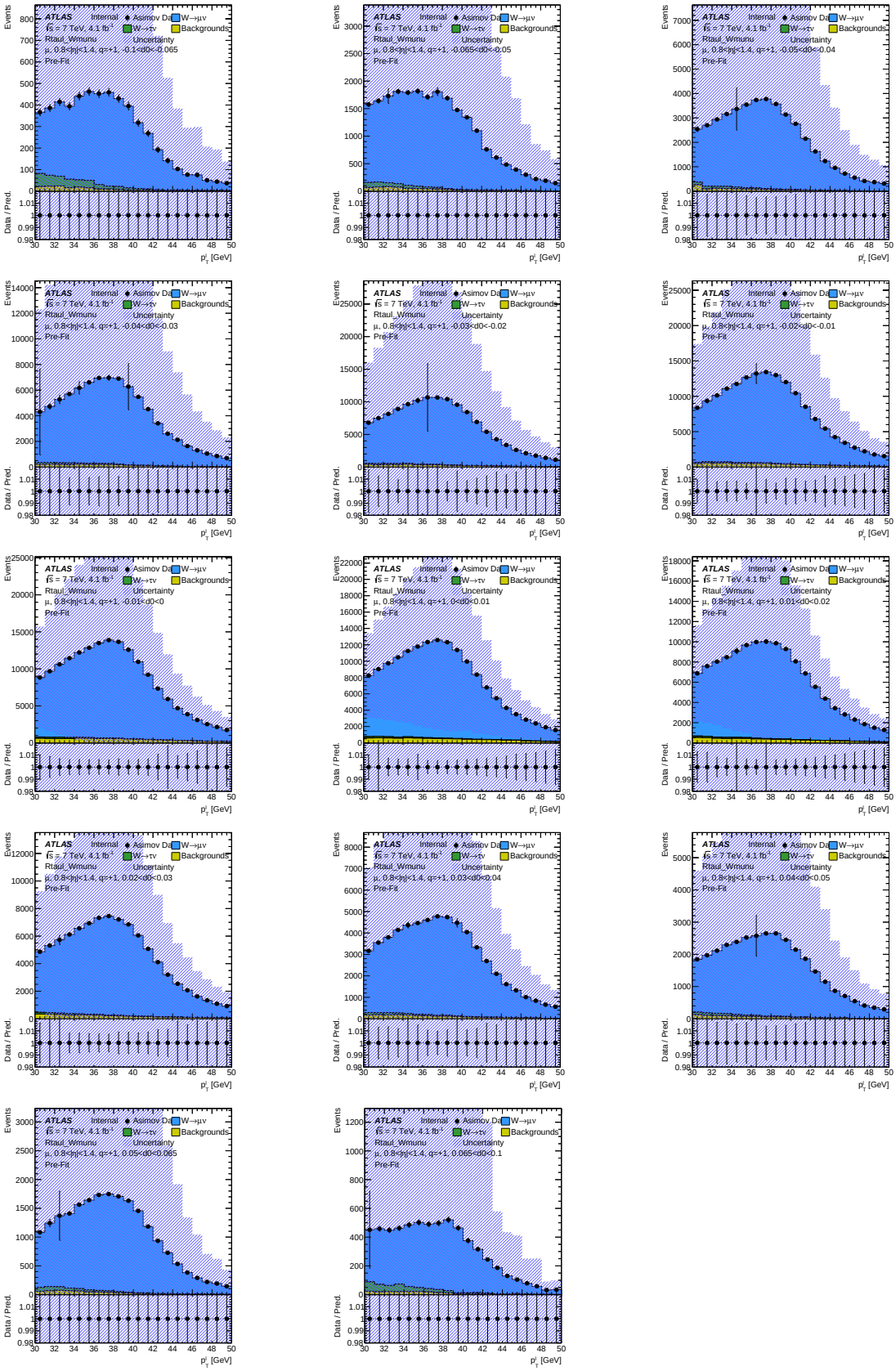

(a) p_T fit for d_0 in 14 bins. Not all slices could be shown thus as an example only $0.8 < |\eta| < 1.4$ and $q = +1$ is shown. Lower panel shows the ratio of data and MC. Further information can be found in the legend

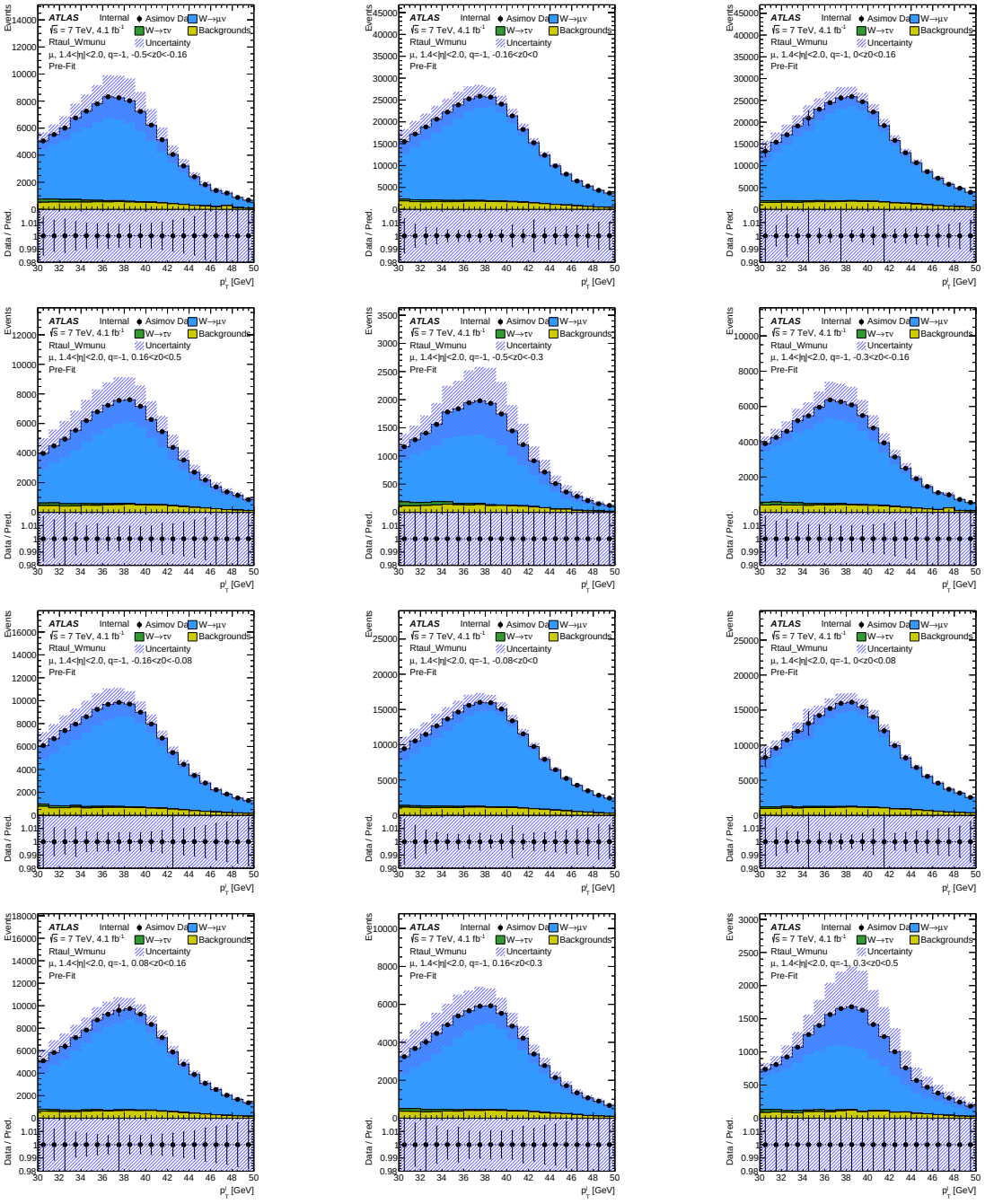

Figure E.3: p_T fit for z_0 in 4 and 8 bins. Not all slices could be shown thus as an example only $1.4 < |\eta| < 2.0$ and $q = -1$ is shown. The lower panel shows the ratio of data and MC. Further information can be found in the legend

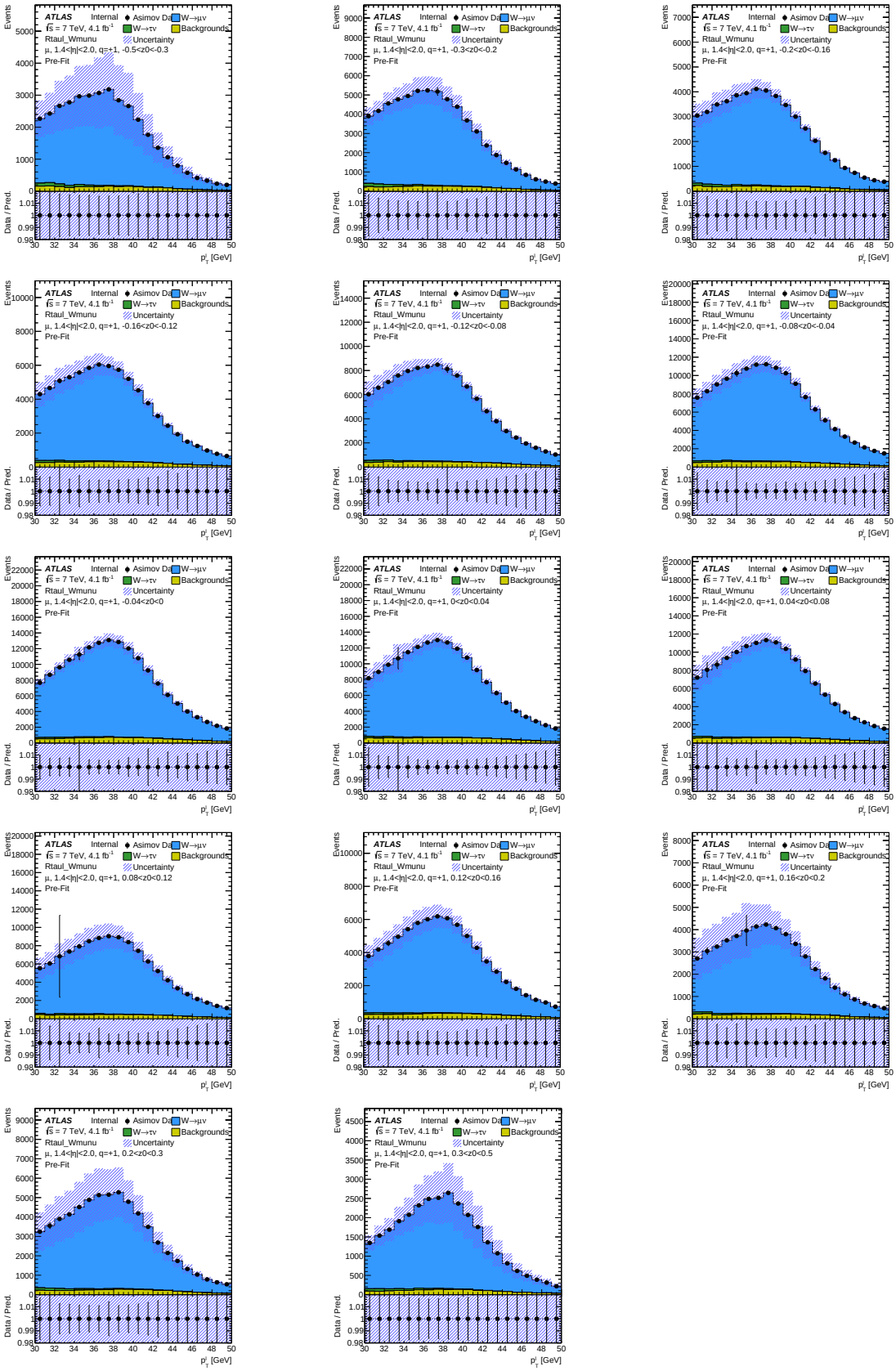

(a) p_T fit for z_0 in 14 bins. Not all slices could be shown thus as an example only $1.4 < |\eta| < 2.0$ and $q = +1$ is shown. The lower panel shows the ratio of data and MC. Further information can be found in the legend

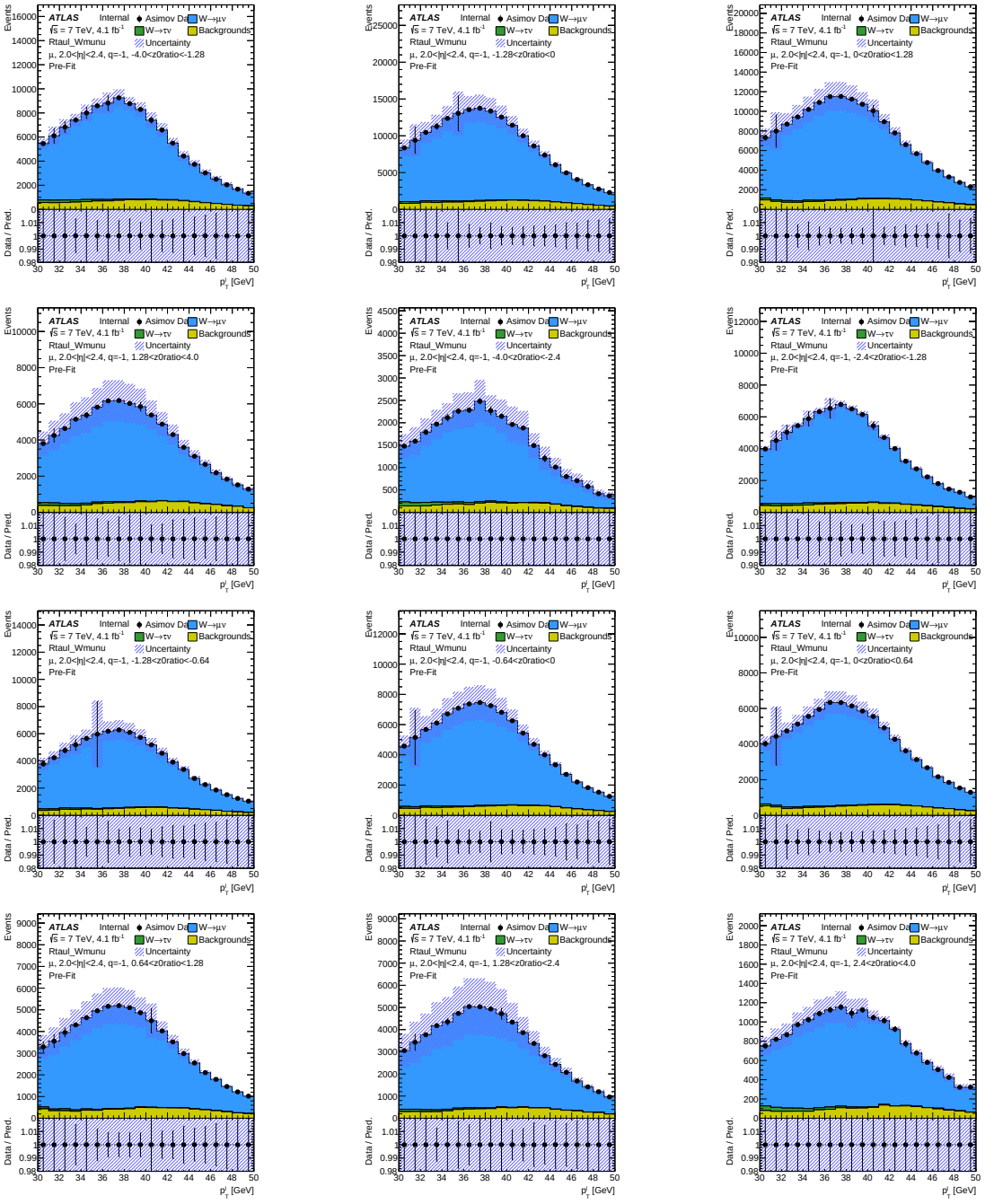

Figure E.5: p_T fit for $z_0/\sigma(z_0)$ in 4 and 8 bins. Not all slices could be shown thus as an example only $2.0 < |\eta| < 2.4$ and $q = -1$ is shown. he lower panel shows the ratio of data and MC. Further information can be found in the legend

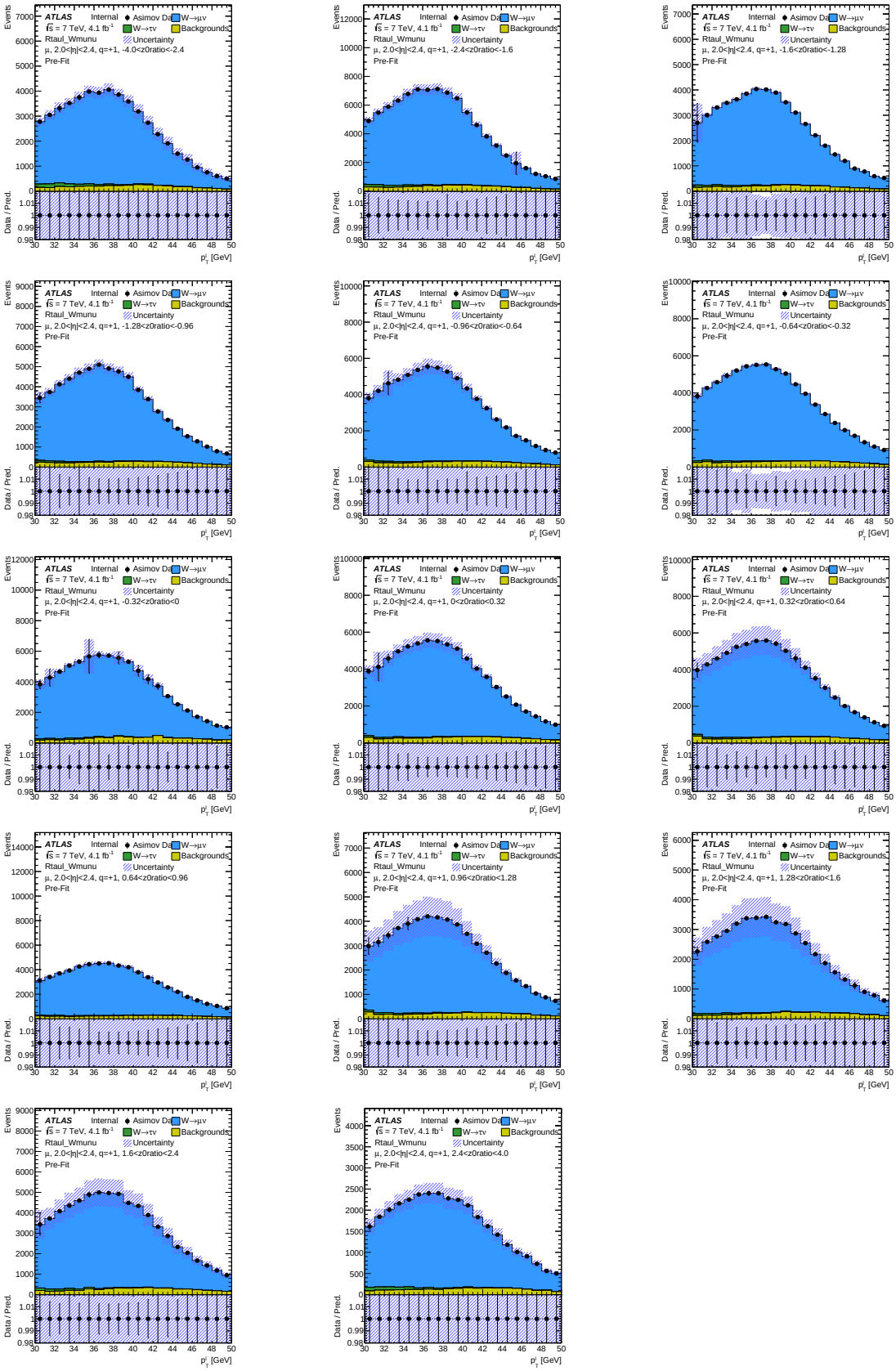

Figure E.6: p_T fit for $z_0/\sigma(z_0)$ in 14 bins. Not all slices could be shown thus as an example only $2.0 < |\eta| < 2.4$ and $q = +1$ is shown. The lower panel shows the ratio of data and MC. Further information can be found in the legend

List of Figures

List of Tables